University of Alberta

Air-core microcavities and metal-dielectric filters - building blocks for optofluidic microsystems

by

Trevor Warren Allen

A thesis submitted to the Faculty of Graduate Studies and Research
in partial fulfillment of the requirements for the degree of

Doctor of Philosophy

in

Photonics and Plasmas

Department of Electrical and Computer Engineering

Fall 2012
Edmonton, Alberta

Abstract

This thesis describes a study on two optical devices intended to be building blocks for the creation of integrated optical/microfluidic lab-on-a-chip systems. First, arrays of curved-mirror dome-shaped microcavities were fabricated by buckling self-assembly of a-Si/SiO_2 multilayers. This novel technique employs controlled, stress-induced film delamination to form highly symmetric cavities with minimal roughness defects or geometrical imperfections. Measured cavity heights were in good agreement with predictions from elastic buckling theory. Also, the measured finesse ($> 10^3$) and quality factor ($> 10^4$ in the 1550-nm range) were close to reflectance-limited predictions, indicating low defects and roughness. Hermite- and Laguerre-Gaussian modes were observable, indicating a high degree of cylindrical symmetry.

In the second part of the research, transmittance in periodic metal-dielectric multilayer structures was studied. Metal-dielectric stacks have many potential applications in optofluidic microsystems, including as transmission filters, superlenses, and substrates for surface plasmon sensors. In this work, we showed that potential transmittance theory provides a good method for describing the tunneling of photons through metal-dielectric stacks, for both Fabry-Perot and surface plasmon resonances. This approach explains the well-known fact that for a given thickness of metal, subdividing the metal into several thin films can increase the maximum transmittance. Conditions for admittance matching of dielectric-metal-dielectric unit cells to an external air medium were explored for Fabry-Perot based tunneling, revealing that thicker metal films require higher-index dielectrics for optimal admittance matching. It was also shown for the first time that potential transmittance theory can be used to predict the maximum possible transmittance in surface-plasmon-mediated tunneling.

In a subsequent study, potential transmittance was used to derive an expression

for reflection-less tunneling through a dielectric-metal-dielectric unit cell. For normal-incidence light in air, only a specific and impractically large dielectric index can enable a perfect admittance match. For off-normal incidence of TE-polarized light, an admittance match is obtained for a specific angle determined by the index of the ambient and dielectric media and the thickness and index of the metal. For TM-polarized light, admittance matching is possible for surface-plasmon-mediated tunneling. These results provide important insight for the design and optimization of optical filters and superlenses.

Acknowledgements

This thesis took longer than most, so there's a great deal of people that need to be thanked for their help. If I've missed you in this list, please know that your help was greatly appreciated and you have my eternal thanks.

Thanks especially go to my supervisor Dr. Ray DeCorby, for his hard work, guidance, advice, financial support and infinite patience. He went above and beyond to get me though this Ph.D., and for that I will be eternally grateful.

Thanks to David Clegg, for all his advice and help. Our weekly lunches were a great way to learn new lab techniques and hammer out ideas.

Thanks to all the members of the photonics lab group, past and present. They made working at the university a pleasure, and their work and advice were instrumental in the completion of my thesis. So thank you to Dr. Nakeeran Ponnampalam, Florian Lenz, Tom Clement, Eric Epp, Josh Silverstone, Trevor Olsen, Brian Drobot, Ward Newman, Aaron Melnyk, Carson Zhang, Clinton Potts, Seyed Azmayesh, and Zahuril Islam.

Thanks to Dr. Chris Haugen and Dr. Jim McMullin for all their help in co-supervising me early on in my Ph.D..

Thanks to TRLabs, Alberta Ingenuity and NSERC for funding assistance over the course of my degree. At TRLabs in particular, thanks to Vinod Ratti and Linda Richens for their help, support and for lending vital equipment.

Thanks to Dr. P.K. Dwivedi and Dr. Ying Tsui for their help in the early parts of my thesis. The work we did on pulsed laser deposition didn't work out in the end, but it was a great learning experience nonetheless.

Thanks to Aden Grue, Kar Mun Cheng and Brian Forst. Our "hackerspace" sessions kept me sane in the long, cold dark of thesis writing.

Thanks to my parents and my brother, Chris, for their support and encouragement.

Thanks to Dr. Al Meldrum and his research group all their support and collaborations with our group over the years.

Thanks to Pinder Bains for her help with the administrative side of my grad studies.

And finally, thanks to all my friends who supported and encouraged me through my time in grad studies. Your help was greatly appreciated.

Table of Contents

List of Tables

List of Figures

List of Symbols and Abbreviations

Symbols

A	Absorptance
A_1, A_2	Amplitude coefficients for transmitted light waves
A_i	Amplitude coefficient for incident light wave
b	Half-width of delamination buckle [m]
B	Input electric field normalized to exit electric field
$B_{1,}B_2$	Amplitude coefficients for reflected light waves
c	Speed of light in vacuum (3×10^8 m s^{-1})
C	Input magnetic field normalized to exit electric field [S]
C_{even}	Normalization constant for even Ince-Gaussian modes
C_p^m	Ince polynomials for even Ince-Gaussian modes
d	Separation of reflective surfaces in optical resonator [m]
D	Diameter of plate/buckle [m]
d_{total}	Total thickness of all metal layers in metal-dielectric multilayer [m]
E	Young's modulus [Pa] (Chapter 2.1)
E	Electric field [V m^{-1}] (Chapter 2.2)
E_{in}	Electric field entering film [V m^{-1}]
E_{out}	Electric field exiting film [V m^{-1}]

F	Finesse
F_d	Overall defect finesse
F_{dg}	Surface irregularity defect finesse
F_{dp}	Parallelism defect finesse
F_{ds}	Spherical defect finesse
F_{eff}	Effective finesse
F_R	Reflective finesse
g	Degeneracy condition parameter
G_o	Elastic energy per unit area stored in unbuckled film [J m^{-2}]
$\overline{G}$	Energy release rate averaged over curved end of buckle [J m^{-2}]
h	thickness [m]
H	High-index dielectric layer
H_ℓ, H_m	Hermite polynomials
H_{in}	Magnetic field entering film [A m^{-1}]
H_{out}	Magnetic field exiting film [A m^{-1}]
I_{in}	Intensity of light entering layer after reflections [W m^{-2}]
I_{exit}	Intensity of light exiting layer after reflections [W m^{-2}]
I_i	Intensity of light incident on resonator [W m^{-2}]
I_r	Intensity of light reflected by resonator [W m^{-2}]
I_t	Intensity of light transmitted through resonator [W m^{-2}]

k	Wavenumber [m^{-1}]
k_o	Free space wavenumber [m^{-1}]
k_q	Wavenumber of qth mode [m^{-1}]
K	Spring constant [N m^{-1}]
L	Low-index dielectric layer
$L_{p,l}$	Laguerre polynomial
m	Integer
$[M]$	Characteristic matrix
n	Refractive index
N	Integer
N	Complex refractive index (Chapter 2.3)
n_{eff}	Effective refractive index
N_M	Complex refractive index (Chapter 3)
PT	Potential transmittance
PT_{MAX}	Maximum potential transmittance
q	Integer
Q	Quality factor
R	Reflectance
$R_{1,}R_2$	Radius of curvature of cavity mirrors 1 and 2 [m]
R_{CD}	Expected radius of curvature of dome [m]

R_C	Measured radius of curvature of dome [m]
$R(z)$	Radius of curvature of wavefront of beam [m]
S_{odd}	Normalization constant for odd Ince-Gaussian modes
S_p^m	Ince polynomials for odd Ince-Gaussian modes
T	Transmittance
U_f	Energy released in plastic deformation of film [J m^{-2}]
U_{fric}	Energy released due to friction [J m^{-2}]
U_o	Energy per unit are in unbuckled portion of plate [J m^{-2}]
U_s	Energy released in plastic deformation of substrate [J m^{-2}]
$\overline{U}$	Average energy per unit area in fully buckled portion of plate [J m^{-2}]
v	Poisson's ratio
v_m	Resonance frequency of cavity [Hz]
V_m	Mode volume [m^3]
v_q	Resonance frequency of qth mode [Hz]
$v_{q,\ell,m}$	Resonance frequency of q,ℓ,m Hermite Gaussian mode [Hz]
v_o	Frequency of mode [s^{-1}]
w	Normal displacement of Euler buckle (Chapter 3.2)
W_A	True work of adhesion [J m^{-2}]
X	Real component of admittance Y_{out} [S]
X_{op}	Real component of optimal admittance Y_{op} [S]

y	Admittance in free space units
Y_{out}	Admittance of output structure [S]
Y_{op}	Optimal exit admittance [S]
Z	Imaginary component of admittance Y_{out}
Z_0	Impedance of free space [Ω]
Z_{op}	Imaginary component of optimal admittance Y_{op} [S]
z_1, z_2	Position of mirrors 1 and 2 on z-axis [m]
z_o	Rayleigh range [m]
α	Real component of complex metal phase thickness δ_M
α_{bulk}	Bulk absorption coefficient [m^{-1}]
α_{eff}	Effective absorption coefficient [m^{-1}]
β	Imaginary component of metal phase thickness δ_M
δ	Normal displacement of Euler buckle [m] (Chapter 2.1)
δ	Peak height of spherical buckle [m] (Chapter 3.2)
δ	Phase thickness of layer (general)
δ_M	Complex phase thickness of metal film
δ_{eff}	Effective phase thickness
δ_{max}	Maximum normal displacement of Euler buckle [m]
η	Gouy phase shift

ΔL	Path difference travelled by light wave during single round trip in resonator [m]
$\Delta\lambda_T$	Wavelength spacing between non-degenerate transverse spatial modes [m]
Δv	Free spectral range of cavity [Hz]
$\Delta v_{1/2}$	Full width half maximum [Hz]
Δv_{HG}	Frequency separation between adjacent Hermite-Gaussian modes [Hz]
ε	Ellipticity parameter
γ_f	Surface energy of film [J m^{-2}]
γ_s	Surface energy of substrate [J m^{-2}]
γ_{fs}	Energy of film-substrate interface [J m^{-2}]
Γ	Interface toughness [J m^{-2}]
κ_M	Extinction coefficient
λ	Wavelength [m]
μ	Effective phase thickness of metal layer
ω	Angular frequency of mode [rad s^{-1}]
$\omega(z)$	Spot size of laser beam [m]
ω_o	Minimum spot size of laser beam [m]
ϕ	Phase shift experienced by light wave during single round trip in resonator (Chapter 2.2)

ψ	Complex factor determining difference between wave in resonator and uniform plane wave
σ_c	Critical compressive biaxial stress needed to induce buckling [Pa]
σ_o	Biaxial compressive stress in film [Pa]
θ_i	Angle of incidence of light
$\theta_{\ell,m}(z)$	Phase change of $\mathrm{TEM}_{\ell,m}$ wave in direction of propagation
θ_M	Complex angle of propagation in absorptive layer
(x,y,z)	Cartesian coordinates
(r,ϕ,z)	Cylindrical coordinates
(ξ,φ,z)	Elliptical coordinates
(ℓ,m)	Hermite polynomial mode indices for coordinate directions
(p,l)	Laguerre polynomial mode indices for radial and azimuthal coordinate directions
(p,m)	Ince polynomial mode indices

Abbreviations

a-Si	Amorphous silicon
AR	Anti-reflection
CQED	Cavity quantum electrodynamics
DMD	Dielectric-metal-dielectric
FFL	Far-field superlens

FSR	Free spectral range
FWHM	Full width half maximum
HG	Hermite-Gaussian
IG2	Chalcogenide glass composed of GeAsSe
IT	Induced transmission
ITO	Indium tin oxide
LED	Light emitting diode
LG	Laguerre-Gaussian
MD	Metal-dielectric
MDM	Metal-dielectric multilayer
MEMS	Micro electro mechanical systems
PAI	Polyamide-imide
TE	Transverse electric
TEM	Transverse electromagnetic
TM	Transverse magnetic
VASE	Variable angle spectroscopic ellipsometry

1 Introduction

This thesis describes an experimental and theoretical study into optical filters and resonators, with the intended goal of developing devices for optical lab-on-a-chip applications. This work grew out of previous developments in our research group, which facilitated the creation of novel curved-mirror microstructures. The present chapter provides some background and context for the rest of the thesis.

1.1 Optofluidic microsystems

In lab-on-a-chip [1] and optofluidic [2] microsystems, there is a need to be able to integrate many different devices into a single platform, to facilitate a diverse set of sensing and analysis requirements. Waveguides and microchannels are needed to transport light and fluid between on-chip components. In biophotonic analysis methods such as fluorescence and Raman spectroscopy, spectral filtering is necessary to separate the excitation source from emitted signal wavelengths. This filtering is sometimes accomplished using absorption filtering, where a material has high absorptance at the excitation wavelength but low absorptance at the signal wavelength. The alternative is to use interference filters (an example of which is shown in Figure 1.1), where a multilayer dielectric stack is designed to filter out the excitation source [1]. Devices combining the two methods in a hybrid filter, to mitigate the drawbacks of both, have also been demonstrated [4], as shown in Figure 1.2. Microresonators have been studied for many applications, including optical sources such as LEDs and microlasers, optical filters and switches for WDM systems, cavity quantum electrodynamics, and fluorescence enhancers for biochemical sensors [5]. One example of an array of microcavities is shown in Figure 1.3. As a final example, metal-dielectric superlenses, described in Section 1.3.2, are being investigated as a means of optically imaging nanometer scale

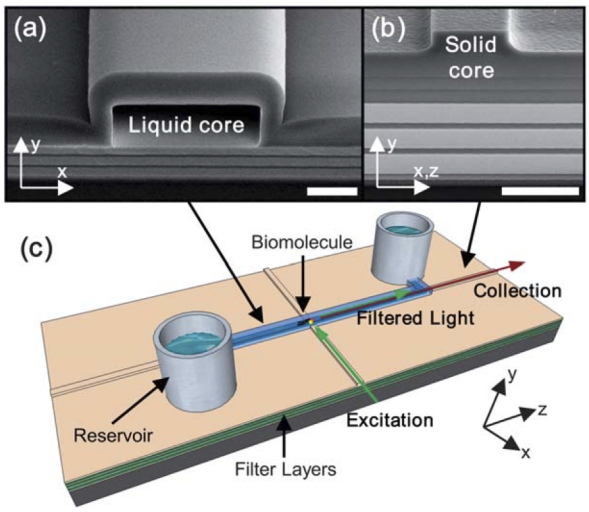

Figure 1.1: Example of an optofluidic filter designed for detecting biomolecules [6]. (a) and (b) show SEM images of the hollow and solid core portions of the waveguide, respectively, and (c) shows a schematic of the integrated optical filter.

objects and individual molecules [3].

In previous research, our group developed a method of fabrication, called buckling self-assembly, that potentially allows for straightforward creation and integration of many of the components required for these lab-on-a-chip devices, including microfluidic channels, optical waveguides, microcavities and curved metal-dielectric superlenses and filters. In this thesis, we studied two specific building blocks necessary for the development of these systems - resonant microcavities and metal-dielectric multilayer stacks - and were able to successfully demonstrate their potential utility for applications in lab-on-a-chip systems.

1.2 Buckling self-assembly

For several years our research group has been studying buckling self-assembly, a procedure for fabricating hollow microstructures by controlled delamination of thin film dielectric stacks. In this process, an area of low adhesion is patterned within a thin film stack on a substrate, allowing the films to separate in that area when

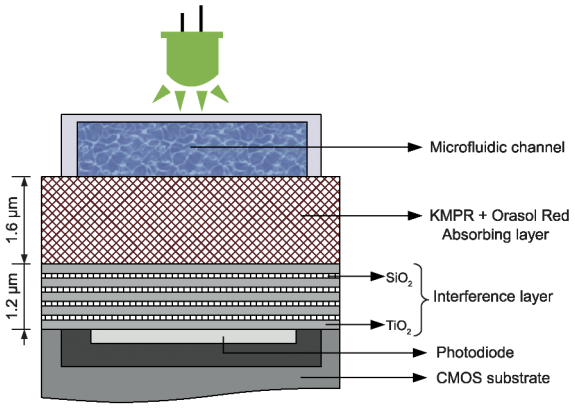

Figure 1.2: Schematic of hybrid optofluidic filter designed by Richard *et al*. [4], integrated with an analytical device.

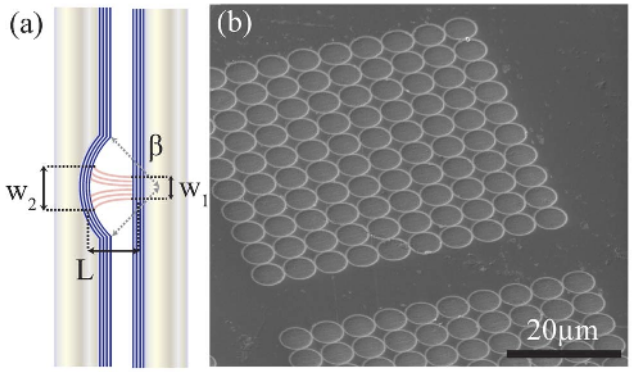

Figure 1.3: (a) Schematic of half-symmetric microcavities. (b) Array of concave features milled in silicon, which comprises one-half of the cavities shown in (a). Another flat mirror layer is added to complete the cavities [7]. Our microcavities, formed through buckling self-assembly, have the benefit of being fully formable on a single substrate.

the sample is subjected to a critical amount of stress. Many different structures can be formed, including crossing, ring-shaped and tapered channels, and previous work was primarily focused on air-core waveguides (with Bragg reflector claddings) fabricated by this technique.

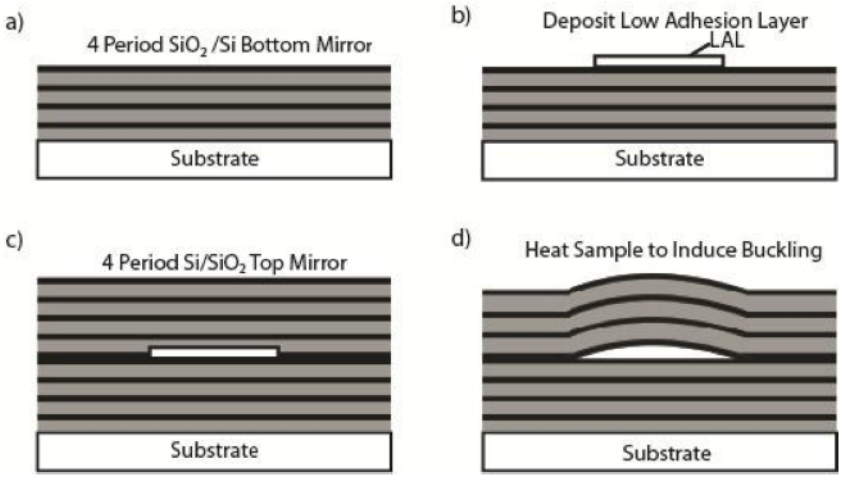

Figure 1.4: Schematic of process for producing buckling in Si/SiO_2 thin film system. (a) a 4-period Si/SiO_2 Bragg mirror is deposited on a Si substrate. (b) A low-adhesion fluorocarbon layer is deposited on the mirror according to a desired pattern. (c) Another 4-period mirror is deposited with deposition parameters that produce a net compressive stress in the layer. (d) Heat is applied to the sample to induce adhesion loss and the stress in the top layer causes it to buckle and form the patterned structure. [10]

We have successfully formed these waveguides using two material systems. In the first case, multilayers containing alternating layers of chalcogenide glass (IG2) and commercial polymer (PAI) were used, with silver doping of the chalcogenide glass used to define regions of low adhesion [8, 9]. In the second case, multilayers containing alternating layers of SiO_2 and Si with a patterned low adhesion layer of fluorocarbon were used [10]. The general procedure for the Si/SiO_2 system is shown in Figure 1.4.

As mentioned, this process allows complex structures including bends and tapers to be manufactured in parallel, with smooth sidewalls that allow for low loss light propagation and fluid flow [10]. Air-core waveguides have many potential

applications including chip-scale optical interconnects [11], optical analysis of small amounts of gases or liquids [12], device tuning through actuation of the top mirror [13], and creation of microfluidic channel networks [14].

Motivating the work in the first part of this thesis, it was found that a circular region of the low adhesion layer will, under appropriate conditions, produce a microscopic dome-shaped optical resonator, examples of which are shown in Figure 1.5. The research discussed in Chapter 3 of this thesis is a detailed study of the morphology and optical properties of these microcavities.

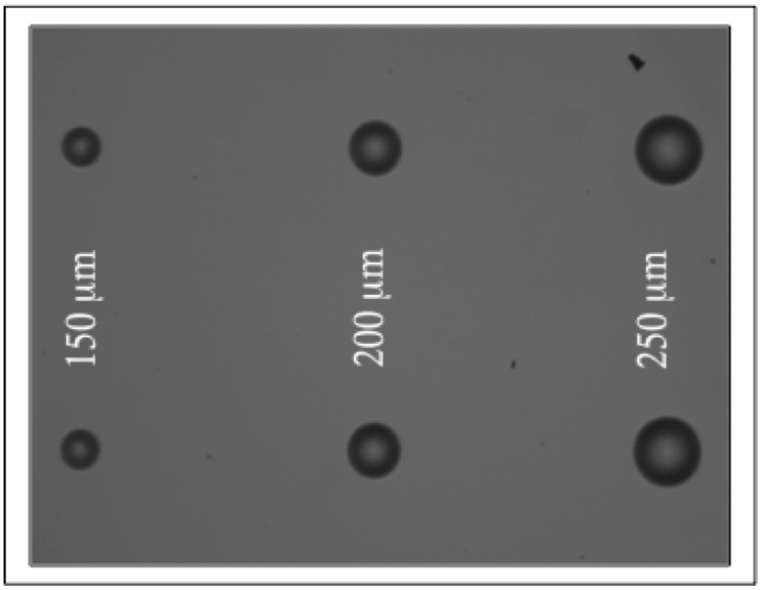

Figure 1.5: Domes of various sizes fabricated through buckling self-assembly.

1.3 Applications of curved spherical surfaces in microsystems

1.3.1 Curved mirror microcavities

Fabry-Perot microcavities in general have several useful properties for optical systems, including sharp resonances and high resolving power in spectroscopic applications [15]. Cavities with curved mirrors, such as the half-symmetric dome-shaped cavities described in Chapter 3, have several advantages over cavities

with planar mirrors. These advantages include the potential for improved quality factor and finesse, which are limited by factors such as non-parallel mirrors in planar cavities [16]. Furthermore, curved mirror Fabry-Perot cavities enable three-dimensional confinement of light, and in well-designed and high-quality microcavities, light can be confined to very small modal volumes [15].

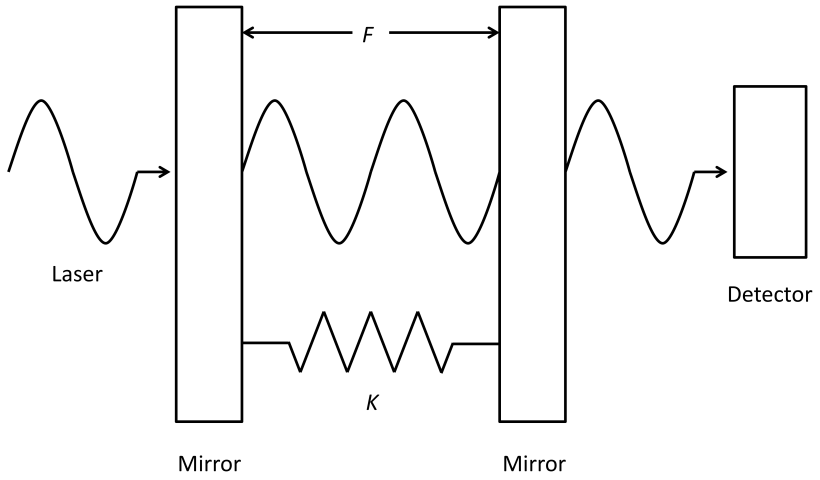

Figure 1.6: Basic schematic of a microcavity used as an optomechanical system. The radiation pressure from the light resonant in the cavity applies a force F on the mirrors, which expand and contract (as a spring with some spring constant K) as the resonant frequency of the cavity changes.

One potential application for these cavities is in the field of optomechanics, where the interaction between electromagnetic radiation and mechanical forces is examined [17]. When resonant light is present in an optical cavity, the photons can exert significant radiation pressure on the cavity walls. If the cavity is deformable, this pressure will cause the cavity to change shape, thereby shifting the resonant frequency and changing the amount of energy stored in the cavity. The amount of pressure will correspondingly decrease, and the cavity will attempt to regain its original shape, creating an optical/mechanical feedback system. This behaviour can be induced through a change in light wavelength or intensity, or in external force applied to the mirrors, and can be used for high-precision measurement applications

such as atomic force microscopy and gravity-wave detectors [18].

Cavities with low modal volume and high finesse have also attracted interest in the field of cavity quantum electrodynamics [19], as well as in studying emissions from single molecules [20]. In general, air-core microcavities with open access to the cavity have great potential for use in microfluidic and lab-on-a-chip systems. If liquids or gases can be controllably introduced into the cavity, novel and high performance lasers [2] and sensing devices [21] might be realized.

1.3.2 Superlenses

Another potential application for the microdome structures described above is in the creation of superlenses, based on artificially engineered metamaterials. When light is incident on an object, the light scattered from its surface is made up of two components: propagating waves which contain the large features of the object, and evanescent waves which contain the small, sub-wavelength features. A typical lens has no problem magnifying the features contained by the propagating waves, but the evanescent waves decay exponentially and are lost in the near-field before they can reach the image plane of the lens. This property is commonly referred to as the diffraction limit of the lens [22]. In the 1990s, Pendry theoretically demonstrated that a negative index metamaterial could overcome this limitation and enable a lens that could enhance the evanescent field through resonant coupling to surface waves [23]. It has been found that very thin metal films are capable of acting as negative index materials for TM-polarized light, and working superlenses have been fabricated using silver films [24].

Superlenses are limited in that they can only produce images that continue in the near-field and therefore again decay exponentially over a short distance. One solution developed to project the evanescent wave into the far-field, and subsequently produce a more useful image of the object's sub-wavelength features,

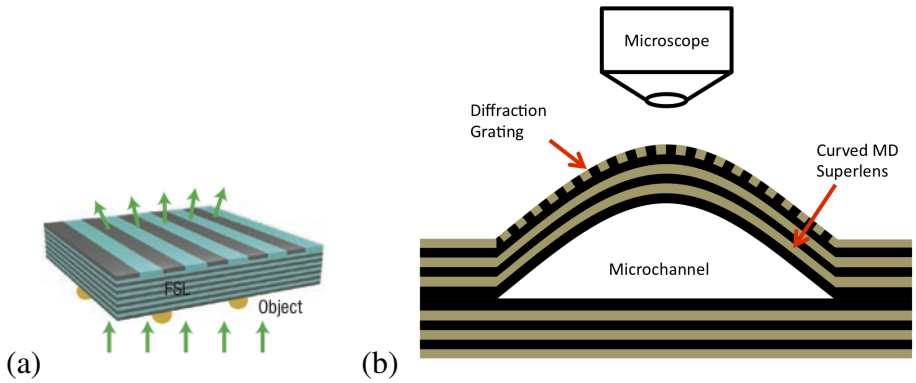

Figure 1.7: (a) Example of multilayer far-field superlens (FFL) [22]. (b) Potential concept of a curved MD far-field superlens integrated into a buckled microchannel.

is the far-field superlens. The far-field superlens consists of a metal layer or a metal-dielectric (MD) multilayer with a sub-wavelength-period, metal-dielectric grating that converts the evanescent field into a propagating wave (the MD multilayer allows for more flexibility in design of the evanescent band) [25]. Implementing superlenses in curved surfaces, like the microdomes fabricated for this thesis, might allow the focal length of the lenses to be pushed out to more practical distances [26]. Furthermore, the implementation of a superlens adjacent to a microfluidic channel might enable high resolution imaging of cells and other organic structures. As shown in Figure 1.7(b), we envision that buckling self-assembly could eventually enable straightforward fabrication of such structures.

MD multilayer devices present additional design challenges in terms of maximizing transmission of light and selection of bandwidth. It was these problems that inspired further study into the second part of this thesis, namely the study of transmission of light through MD multilayer stacks.

1.4 Metal-dielectric multilayer filters

Metal-dielectric transmission filters have been studied for several decades [14], motivated mainly by their ability to exhibit a single transparency band while providing excellent rejection of out-of-band wavelengths [32]. Transmission filters are of great importance in lab-on-a-chip systems [1], for example, in the separation of excitation light from the light fluoresced or scattered by an analyte. In spite of their interesting properties, MD filters have not been widely studied for lab-on-a-chip applications. This fact partly motivated the work described in the second part of the thesis (Chapters 4 and 5), which is a theoretical study of the optimization of transparency bands in periodic dieletric-metal-dielectric multilayers. In the following sub-sections, a brief overview of some of the traditional applications for transparent MD stacks is provided.

1.4.1 Solar/Heat-reflecting windows

MD multilayer stacks have traditionally found use as transparent heat mirrors and heat-reflecting windows [29, 30, 31]. In this application, MD multilayers are designed to have optimal transmittance in the visible range, while being highly reflective in the infrared region (Figure 1.8). Heat-reflecting windows can be used for many applications, such as solar cells, where they prevent external heat from interfering with the efficiency of the solar cell, or as windows in buildings that prevent heat transfer while letting sunlight through [31].

1.4.2 Transparent conductors

A great deal of recent study has been focused on transparency bands exhibited by metal-dielectric photonic bandgap structures [32]. It has been shown that for both propagating [28] and evanescent [33] waves, splitting a metal layer into multiple thinner layers separated by dielectrics can yield a higher transmission than that

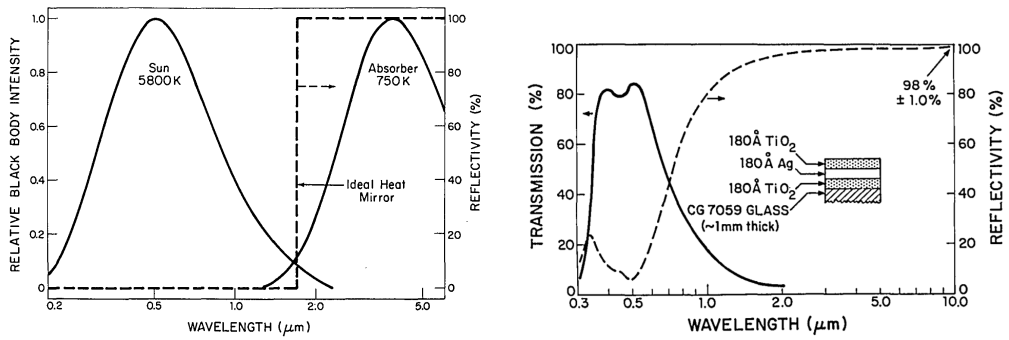

(a) (b)

Figure 1.8: (a) Plot showing the small amount of overlap between the light spectrum emitted by the sun and the heat emitted by an object that has absorbed the solar energy. An ideal heat mirror (indicated by the dotted line) would be able to filter out the majority of heat, while still letting light through [30]. (b) Measured transmission and reflectivity of a TiO_2/Ag/TiO_2 thin film designed as a heat mirror [30].

obtainable with the original metal layer, due to resonant tunneling. However, it has often been overlooked that this property can be explained using the theory of potential transmittance, developed by Berning and Turner in 1957 [12]. This theory is discussed further in Chapters 2, 4 and 5. The ability to increase transmission of light through metals at specific wavelengths is highly useful, considering that metals can be both highly reflective, allowing for the design of filters with high rejection of out-of-band wavelengths/frequencies, and highly conductive, facilitating their use in optoelectronic applications such as solar cells and in transparent conductive display technology [32]. Traditionally, films of indium oxide doped with tin (commonly referred to as indium tin oxide (ITO)), have found common use as transparent conductors [28, 35]. However, these films are hindered by high resistivities (three orders of magnitude higher than those for metals) [28] and a higher tendency to fail under mechanical strain compared to other layers [36]. Transparent conductors made of MD multilayer stacks can be designed to have transmission similar to ITO conductors, and benefit from much lower electrical resistance and increased flexibility, making them ideal for applications such as solar cells, windshields, electromagnetic interference

shielding, and electrodes for displays [36].

1.5 Summary of thesis

This thesis describes work on dome microcavity structures fabricated through buckling self-assembly of thin film stacks, and work on the design and optimization of MD multilayer stacks using the concept of potential transmittance. The chapters are summarized as follows:

Chapter 2 summarizes some background theory applicable to this work, including theoretical treatments of buckling self-assembly, Fabry-Perot optical cavities and potential transmittance.

Chapter 3 describes the work done on the microcavity domes fabricated by buckling self-assembly, with examinations of their structure, their viability as resonant cavities and the structure of modes they support.

Chapters 4 and 5 describe our studies on the application of the theory of potential transmittance to periodic metal dielectric multilayers. The studies involve finding the conditions that match the admittance of the MD multilayer to an ambient medium and thus optimize the transmittance of light through the stack. The work encompasses cases of both normal and oblique incidence, and tunneling of both propagating and evanescent waves.

Chapter 6 outlines some preliminary experimental work intended to demonstrate admittance matching in real-life dielectric-metal-dielectric multilayers. Measured and theoretical results are compared for three different multilayer designs.

Chapter 7 provides some concluding remarks on the topics presented in the thesis, as well as some speculation on possible future work.

References

[1] M. Dandin, P. Abshire, E. Smela, "Optical filtering technologies for integrated fluorescence sensors", *Lab Chip*, vol. 7, pp. 955-977, 2007.

[2] C. Monat, P. Domachuk, B.J. Eggleton, "Integrated optofluidics: A new river of light", *Nature Photonics*, vol. 1, pp. 106-114, 2007.

[3] C. Jeppesen, R.B. Nielsen, A. Boltasseva, S. Xiao, N.A. Mortensen, A. Kristensen, "Thin film Ag superlens towards lab-on-a-chip integration", *Opt. Express*, vol. 17, pp. 22543-22552, 2009.

[4] C. Richard, A. Renaudin, V. Aimez, P.G. Charette, "An integrated hybrid interference and absorption filter for fluorescence detection in lab-on-a-chip devices", *Lab Chip*, vol. 9, pp. 1371-1376, 2009.

[5] T.M. Benson, S.V. Boriskina, P. Sewell, A. Vukovic, S.C. Greedy and A.I. Nosich, "Micro-optical resonators for microlasers and integrated optoelectronics: Recent advances and future challenges", in *Frontiers in Planar Lightwave Circuit Technology*, S. Janz et al. (eds.), pp. 39–70, Springer, 2006.

[6] P. Measor, B.S. Phillips, A. Chen, A.R. Hawkins, H. Schmidt, "Tailorable integrated optofluidic filters for biomelecular detection", *Lab Chip*, vol. 11, pp. 899-904, 2011.

[7] P.R. Dolan, G.M. Hughes, F. Grazioso, B.R. Patton, J.M. Smith, "Femtoliter tunable optical cavity arrays", *Opt. Lett.*, vol. 35, pp. 3556-3558, 2010.

[8] R.G. DeCorby, N. Ponnampalam, H.T. Nguyen, M.M. Pai, T.J. Clement, "Guided self-assembly of integrated hollow Bragg waveguides", *Opt. Express*, vol. 15, pp. 3902-3915, 2007.

[9] E. Epp, N. Ponnampalam, J.N. McMullin, R.G. DeCorby, "Thermal tuning of hollow waveguides fabricated by controlled thin-film buckling", *Opt. Express*, vol. 17, pp. 17369-17375, 2009.

[10] E. Epp, N. Ponnampalam, W. Newman, B. Drobot, J.N. McMullin, A.F. Meldrum, R.G. DeCorby, "Hollow Bragg waveguides fabricated by controlled buckling of Si/SiO_2 multilayers", *Opt. Express*, vol. 18, pp. 24917-24925, 2010.

[11] Y. Zhou, V. Karagodsky, B. Pesala, F.G. Sedgwick, C.J. Chang-Hasnain, "A novel ultra-low loss hollow-core waveguide using subwavelength high-contrast gratings," *Opt. Express*, vol. 17, pp. 1508-1517, 2009.

[12] S. Campopiano, R. Bernini, L. Zeni, P.M. Sarro, "Microfluidic sensor based on integrated optical hollow waveguides," *Opt. Lett.*, vol. 29, pp. 1894-1896, 2004.

[13] F. Koyama, T. Miura, Y. Sakurai, "Tunable hollow waveguides and their applications for photonic integrated circuits," *Electronics and Communications in Japan*, vol. 29, pp. 9-19, 2006.

[14] M.W. Moon, S. Chung, K.R. Lee, K.H. Oh, H.A. Stone, J.W. Hutchinson, "Directed assembly of fluidic networks by buckle delamination of films on patterned substrates", *Int. J. Mat. Res.*, vol. 98, pp. 1203-1208, 2007.

[15] R.C. Pennington, G. D'Alessandro, J.J. Baumbert, M. Kaczmarek, "Tracking spatial modes in nearly hemispherical microcavities", *Opt. Lett.*, vol. 32, pp. 3131-3133, 2007.

[16] E.J. Eklund, A.M. Shkel, "Factors affecting the performance of micromachined sensors based on Fabry-Perot interferometry", *J. Micromech. Microeng*, vol. 15, pp. 1770-1776, 2005.

[17] F. Marquardt, S.M. Girvin, "Optomechanics", arXiv:0905.0566v1 [cond-mat.mes-hall], 2009.

[18] I. Favero, K. Karrai, "Optomechanics of deformable optical cavities", *Nature Photonics*, vol. 3, pp. 201-205, 2009.

[19] Y. Colombe, T. Steinmetz, G. Dubois, F. Linke, D. Hunger, J. Reichel, "Strong atom-field coupling for Bose-Einstein condensates in an optical cavity on a chip", *Nature*, vol. 450, pp. 272-276, 2007.

[20] C. Toninelli, Y. Delley, T. Stoferle, A. Renn, S. Gotzinger, V. Sandoghdar, "A scanning microcavity for in situ control of single-molecule emission", *App. Phys. Lett.*, vol. 97, pp. 021107, 2010.

[21] M. Trupke, E.A. Hinds, S. Eriksson, E.A. Curtis, "Microfabricated high-finesse optical cavity with open access and small volume", *App. Phys. Lett.*, vol. 87, 211106, 2005

[22] X. Zhang, Z Liu, "Superlenses to overcome the diffraction limit", *Nat. Mat.*, vol. 7, pp. 435-441, 2008.

[23] J.B. Pendry, "Negative refraction makes a perfect lens", *Phys. Rev. Lett.*, vol. 85, pp. 3966-3969, 2000.

[24] N. Fang, H. Lee, C. Sun, X. Zhang, "Sub-diffraction-limited optical imaging with a silver superlens," *Science*, vol. 308, pp. 534-537, 2005.

[25] Y. Xiong, Z. Liu, C. Sun, X. Zhang, "Two-dimensional imaging by far-field superlens at visible wavelengths", *Nano Lett.*, vol. 7, pp. 3360-3365, 2007.

[26] A.D. Falco, M. Ploschner, T.F. Krauss, "Flexible metamaterials at visible wavelengths," *New J. Phys.*, vol. 12, 113006, 2010.

[27] P.W. Baumeister, “Radiant power flow and absorptance in thin films”, *Appl. Opt.*, vol. 8, pp. 423-436, 1969.

[28] M.J. Bloemer, M. Scalora, “Transmissive properties of Ag/MgF_2 photonic band gaps”, *Appl, Phys. Lett.*, vol. 72, pp. 1676-1678, 1998.

[29] J.C.C Fan, F.J. Bachner, G.H. Foley, P.M. Zavracky, “Transparent heat-mirror films of TiO_2/Ag/TiO_2 for solar energy collection and radiation insulation”, Appl. Phys. Lett., vol. 25, pp. 693-695, 1974.

[30] J.C.C. Fan, F.J. Bachner, “Transparent heat mirrors for solar-energy applications”, *Appl. Opt.*, vol. 15, pp. 1012-1017, 1976.

[31] C.G. Granqvist, “Transparent conductors as solar energy materials: A panoramic review”, *Sol. Energy Mater. Sol. Cells*, vol. 91, pp. 1529-1598, 2007.

[32] M. Scalora, M. J. Bloemer, and C. M. Bowden, "Laminated photonic band structures with high conductivity and high transparency: Metals under a new light," *Opt. Photon. News,* vol. 10, 1999.

[33] S.A. Ramakrishna, J.B. Pendry, M.C.K. Wiltshire, W.J. Stewart, “Imaging the near field”, *J. Mod. Opt.*, vol. 50, pp. 1419-1430, 2003.

[34] P.H. Berning, A.F. Turner, “Induced transmission in absorbing films applied to band pass filter design”, *J. Opt. Soc. Am.*, vol. 47, pp. 230-239, 1957.

[35] K.L. Chopra, S. Major, D.K. Pandya, “Transparent conductors - a status review”, *Thin Solid Films*, vol. 102, pp. 1-46, 1983.

[36] J. Lewis, S. Grego, B. Chalamala, E. Vick, D. Temple, “Highly flexible transparent electrodes for organic light-emitting diode-based displays”, *Appl. Phys. Lett.*, vol. 85, pp., 3450-3452, 2004.

2 Theory

This chapter describes some of the important background theory pertaining to resonant microcavities and metal-dielectric multilayer films, and serves as an introduction to the topics discussed in Chapters 3, 4 and 5.

2.1 Delamination buckles

In order to understand the formation of the dome microcavities studied in Chapter 3, it is useful to examine the theory behind thin film delamination. Buckling delamination is one of the major causes of failure in compressively stressed thin films [1]. In this phenomenon, a film deposited under conditions inducing biaxial compressive stress can delaminate from its substrate, depending on factors such as film stress, film thickness and adhesion. Although delamination can be a problem in thin film fabrication, it can also be used to fabricate interesting structures if the film is fabricated in a way that allows for controlled, patterned delamination in localized areas.

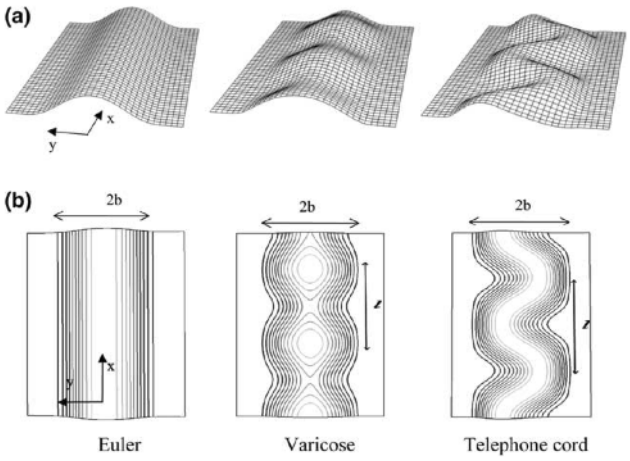

Figure 2.1: Views of the various types of buckles [1].

There are two main types of buckles that form as a delamination propagates through a film, the straight-sided (Euler) buckle and the undulating buckle, which

can take the form of either a telephone cord or in rare cases a varicose structure (Figure 2.1). In an unpatterned film, the particular morphology that appears depends on a number of factors, including film stress, film thickness and adhesion, but mostly on the toughness of the interface between the substrate and the film, which increases as the delamination crack propagates through the film and the mix of stress modes at the interface shifts from normal stress (normal to the plane of the film) to shear stress (in the plane of the film) [1].

When the buckled area is confined to a strip by a patterned area of low adhesion with width greater than a critical width determined by the stress present in the film, the buckle will propagate freely along that area. Smaller widths will produce the Euler buckles, and larger ones will favour the telephone cords, as the stress in the film is relieved in the direction parallel to the strip.

When determining its buckling properties, a patterned thin film area of width $2b$ undergoing buckling can be modeled as an infinitely long plate of the same width clamped fully on all edges. This model will hold true as long as the Young's modulus of the substrate is at greater than or equal to one fifth of that of the film to be buckled, else deformations of the substrate will need to be taken into account [1]. The start of buckling is dominated by the Euler mode, or straight buckle, whose shape is independent of the direction parallel to the strip (as seen in Figure 2.1). The critical compressive biaxial stress σ_c needed to induce buckling in a strip of width $2b$ is given by:

$$\sigma_c = \frac{\pi^2}{12} \frac{E}{1-\nu^2} \left(\frac{h}{b}\right)^2, \tag{2.1}$$

where E is Young's modulus, ν is Poisson's ratio, h is the thickness and b is the half-width of the plate. The cross-section of the buckle can be described by a raised cosine function, and the normal displacement δ of the Euler buckle with half-width b is given by:

$$\delta = \frac{\delta_{max}}{2}\left(1+\cos\left(\frac{\pi y}{b}\right)\right), \tag{2.2}$$

where y is measured from the centre of the buckle and δ_{max} is given by:

$$\delta_{max} = h\sqrt{\frac{4}{3}\left(\frac{\sigma}{\sigma_c}-1\right)}, \tag{2.3}$$

where σ is the biaxial compressive stress in the film. For the Euler mode to continue to propagate a buckle through a film, the energy release rate averaged over the curved end of the buckle must exceed the toughness of the interface, i.e., $\overline{G} > \Gamma$. This energy is the difference between the energy per unit area in the unbuckled portion of the plate (U_o), and the average energy per unit area in the fully buckled portion of the plate ($\overline{U}$).

$$\overline{G} = U_o - \overline{U} \tag{2.4}$$

U_o and $\overline{U}$ can be calculated with the following equations[1, 2]:

$$U_o = \frac{(1-v)\,\sigma^2 h}{E}, \tag{2.5}$$

$$\overline{U} = U_o\left(1-\left(\frac{1+v}{2}\right)\left(1-\frac{\sigma_c}{\sigma}\right)^2\right). \tag{2.6}$$

Substituting these into Equation 2.4 results in

$$\overline{G} = G_o\left(1-\frac{\sigma_c}{\sigma}\right)^2, \tag{2.7}$$

where

$$G_o = \left(\frac{1+v}{2}\right)U_o = \frac{\left(1-v^2\right)\sigma^2 h}{2E} \tag{2.8}$$

is the elastic energy per unit area stored in the unbuckled film, associated with the compressive stress of the pre-buckled film.

The interface toughness Γ, also known as the practical work of adhesion, is made up of several factors. Of mainly theoretical importance is the true work of adhesion, W_A, which is defined as the amount of energy needed to separate two bonded materials from each other:

$$W_A = \gamma_f + \gamma_s - \gamma_{fs}, \tag{2.9}$$

where γ_f and γ_s are the surface energies of the film and substrate, respectively, and γ_{fs} is the energy of the film-substrate interface. When the film debonds from the substrate, other factors in addition to the work of adhesion dissipate energy in the interface and must be overcome by the energy release rate in order for delamination to occur. Accounting for these factors produces a practical work of adhesion, or the actual interface toughness:

$$\Gamma = W_A + U_f + U_s + U_{fric}, \tag{2.10}$$

where U_f and U_s are the energy released in plastic deformation of the film and substrate and U_{fric} is the energy released due to friction. It should be noted that the majority of adhesion testing methods actually measure the interface toughness instead of the true work of adhesion, as they typically involve buckling or peeling of the film, making the true work of adhesion very difficult to extract from measurements [3].

2.2 Fabry-Perot optical microcavities

The microcavities studied in this thesis are made up of an air gap surrounded by two reflectors, one curved and one flat, which is the basic form of a half-symmetric

optical resonator. Fabry-Perot optical resonators are devices used to store light at certain resonance frequencies by continuously reflecting light between two low-loss, flat or curved reflective surfaces separated by a gap or optical medium of length d. In order for light of a given wavelength to be resonant in the cavity, its partial reflections must interfere constructively, i.e. the phase shift or delay between two partially reflected waves must be a multiple of 2π.

2.2.1 Planar Fabry-Perot resonator

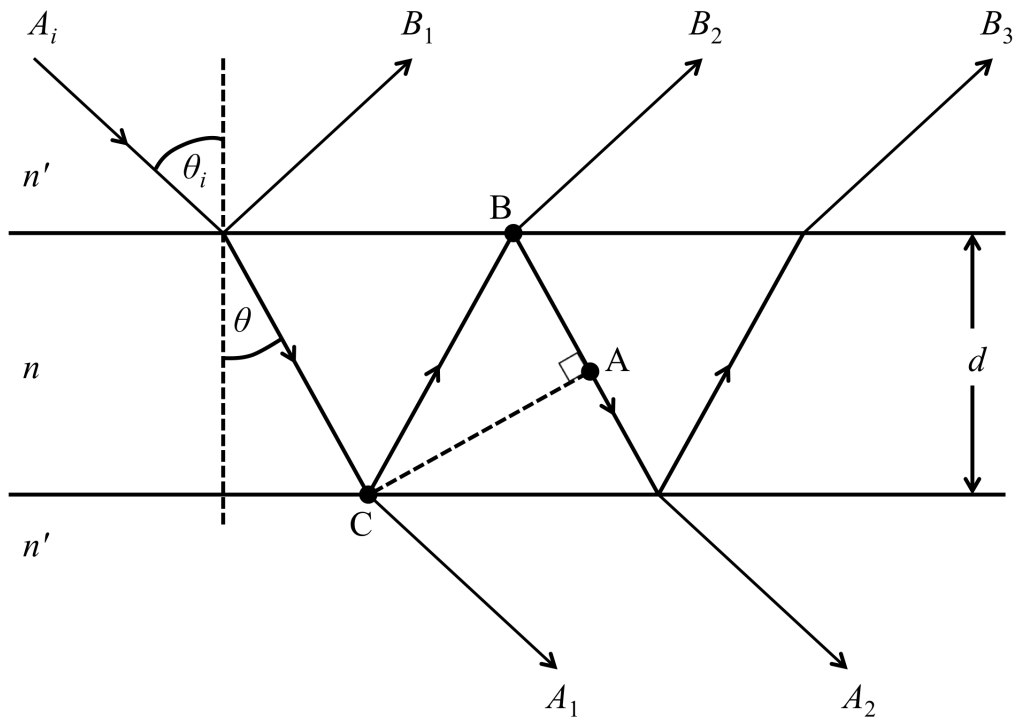

Figure 2.2: Diagram of a basic Fabry-Perot cavity with multiple reflections caused by a wave incident on the cavity at an angle θ_i. A_i, A_n, and B_n are amplitude coefficients denoting the incident, transmitted and reflected light, respectively.

The most basic form of an optical resonator is the Fabry-Perot etalon or interferometer, which consists of a set of plane-parallel mirrors surrounding a medium of index n and immersed in another medium of index n' as shown in

Figure 2.2. For a wave inside the resonator, the path difference travelled during a single round trip is given by:

$$\Delta L = AB + BC = 2d\cos\theta, \tag{2.11}$$

which gives a total phase shift of

$$\phi = \frac{-2\pi(\Delta L)n}{\lambda} = \frac{-4\pi nd\cos\theta}{\lambda}. \tag{2.12}$$

$|\phi/2|$ is generally known as the phase thickness of the layer (denoted by δ). In addition, the fraction of incident light reflected and transmitted by the resonator (derived by summing up the complex amplitudes of the partial reflections of the wave) can be expressed [4]:

$$\frac{I_r}{I_i} = \frac{4R\sin^2\delta}{(1-R)^2 + 4R\sin^2\delta}, \tag{2.13}$$

and

$$\frac{I_t}{I_i} = \frac{(1-R)^2}{(1-R)^2 + 4R\sin^2\delta}, \tag{2.14}$$

where I_i, I_r, and I_t are the total incident, reflected and transmitted intensities of light, and R is the reflectance of the mirrors. From these equations, it is apparent that the transmission through the cavity will be maximum when $\delta = m\pi$, where m is any integer. Combining this fact with Equation 2.12, an equation for the resonance frequencies of the cavity is obtained:

$$v_m = m\frac{c}{2nd\cos\theta}, \tag{2.15}$$

where c is the speed of light in vacuum and v_m is the optical frequency for a given integer m. The difference between the frequencies of two consecutive values of m

$(v_{m+1} - v_m)$ is called the free spectral range of the cavity:

$$\Delta v = \frac{c}{2nd\cos\theta}. \tag{2.16}$$

There are two main figures of merit used to describe optical resonators. These are the quality factor (Q), used to describe the resonator's ability to trap light energy, and the finesse (F), used to measure the resolution of the resonator. There are two definitions for Q that are most commonly used. The first defines Q by the energy stored in the cavity:

$$Q = \omega\left(\frac{\text{field energy stored in resonator}}{\text{power dissipated by resonator}}\right), \tag{2.17}$$

where $\omega = 2\pi v_o$ is the resonance frequency of the mode in question. The second defines Q in terms of the resonance bandwidth of the cavity:

$$Q = \frac{v_o}{\Delta v_{1/2}}. \tag{2.18}$$

where $\Delta v_{1/2}$ is the full width of the transmission peaks of the cavity at half their maximum (FWHM).

The FWHM of a Fabry-perot resonators transmission peaks also determines its ability to resolve individual wavelengths. From Equation 2.14, it can be seen that $I_t/I_i = 0.5$ when:

$$\sin^2\delta = \frac{(1-R)^2}{4R}. \tag{2.19}$$

Since R is close to 1 for most high-resolution cavities, an approximate solution for δ can be obtained, and following some basic arithmetic, the FWHM in terms of frequency ($\Delta v_{1/2}$) can be obtained [4]:

$$\Delta\nu_{1/2} = \frac{c\,(1-R)}{2d\pi\sqrt{R}} = \frac{c}{2dF_R}, \tag{2.20}$$

where $F_R \equiv \pi\sqrt{R}/\,(1-R)$ is the reflective finesse. Ignoring losses other than the loss due to mirrors with sub-unity reflectance, F_R is equal to the effective finesse F_{eff}, which can be found from the transmission spectrum using the free spectral range and the FWHM of a resonant transmission peak:

$$F_{eff} = \frac{\Delta\nu}{\Delta\nu_{1/2}}. \tag{2.21}$$

However, in non-ideal devices, absorption and scattering from imperfect reflectors will cause the effective finesse to diverge from the ideal reflective value. There are three primary types of defects that affect the finesse of the resonator. These are spherical defects (F_{ds}), surface irregularities (F_{dg}) and parallelism defects (F_{dp}) (see Figure 2.3). These contribute to an overall defect finesse as follows:

$$\frac{1}{F_d^2} = \frac{1}{F_{ds}^2} + \frac{1}{F_{dg}^2} + \frac{1}{F_{dp}^2}. \tag{2.22}$$

The final expression for effective finesse is then:

$$\frac{1}{F_{eff}} = \sqrt{\frac{1}{F_R^2} + \frac{1}{F_d^2}}. \tag{2.23}$$

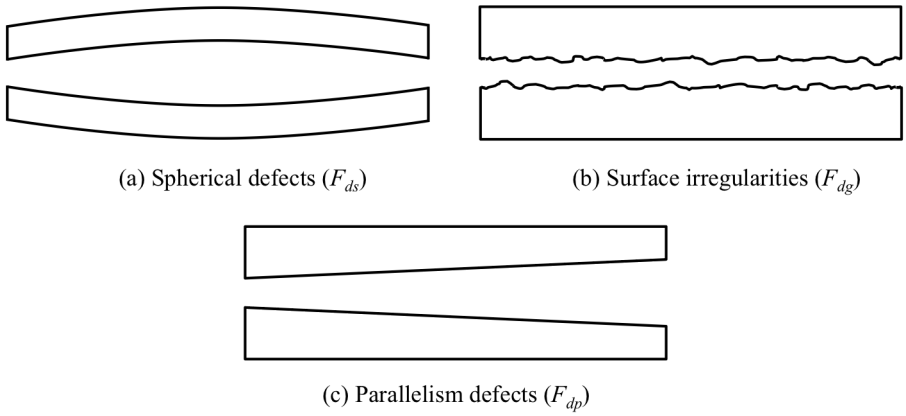

Figure 2.3: Examples of mirror defects that affect the finesse of a Fabry-Perot resonator.

2.2.2 Fabry-Perot cavities with spherical mirrors

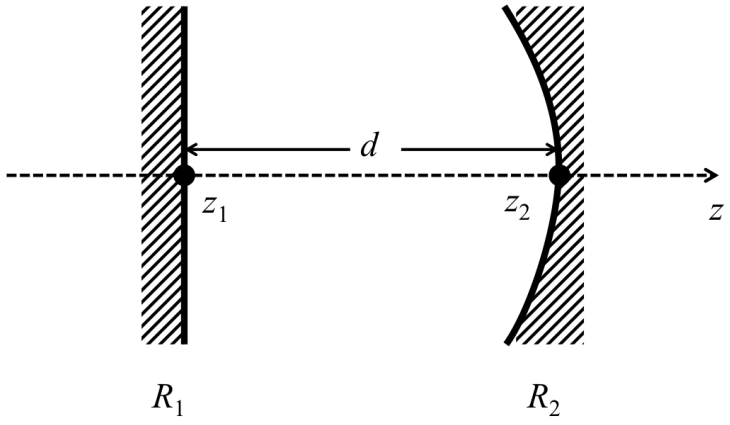

Figure 2.4: Optical cavity with spherical mirror surface of radius R_2. The flat mirror can be considered to have a radius R_1 of infinity. This cavity is the basic form of the resonators studied in Chapter 3 of this thesis.

The previous equations for resonator spectral properties were derived for the Fabry-Perot cavity, i.e., a set of two plane-parallel mirrors, and also assume that the fields are uniform plane waves. However, if a cavity has some amount of lateral confinement of light, as in the case of a cavity with curved mirrors (Figure 2.4), higher-order modes adjacent to the fundamental mode will be supported. In a cavity with rectangular symmetry (with discernible differences in the *x*- and *y*-directions)

adjacent modes will be separable in Cartesian coordinates (see Figure 2.5). These modes are called Hermite-Gaussian modes, and the field distribution of a transverse mode with given (ℓ, m) is given by [5]:

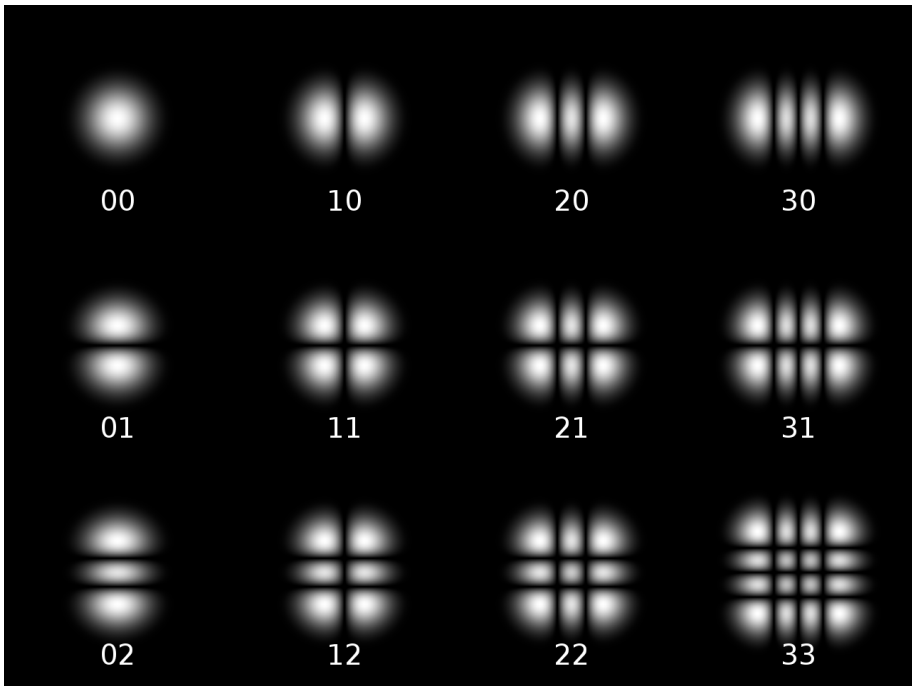

Figure 2.5: Examples of Hermite-Gaussian modes [7].

$$E_{\ell,m} = E_o \frac{\omega_o}{\omega(z)} H_\ell\left(\sqrt{2}\frac{x}{\omega(z)}\right) H_m\left(\sqrt{2}\frac{y}{\omega(z)}\right) \times \exp\left[-\frac{x^2+y^2}{\omega^2(z)} - ik\frac{x^2+y^2}{2R(z)} - ikz + i(\ell+m+1)\eta\right], \tag{2.24}$$

where H_ℓ and H_m are the Hermite polynomials of order ℓ and m, respectively, and $\omega(z)$ is the spot size and is given as:

$$\omega(z) = \omega_o\left[1+\left(\frac{z}{z_o}\right)^2\right]^{1/2}. \tag{2.25}$$

ω_o is the minimum spot size and z_o is the Rayleigh range, also know as the confocal

beam parameter, which is the position where the input beam spot size increases by a factor of $\sqrt{2}$ from the minimum, and is given by:

$$z_o = \frac{\pi \omega_o^2 n}{\lambda}. \tag{2.26}$$

The radius of curvature $R(z)$ of the wavefront is given by:

$$R(z) = z\left[1 + \left(\frac{\pi \omega_o^2 n}{\lambda z}\right)^2\right]. \tag{2.27}$$

Finally, η is the Gouy phase shift, defined as the difference between the phase shift seen by a Gaussian beam relative to the phase shift seen by a plane wave at the same frequency:

$$\eta = \tan^{-1}\left(\frac{z}{z_o}\right) = \tan^{-1}\left(\frac{\lambda z}{\pi \omega_o^2 n}\right). \tag{2.28}$$

As with the Fabry-Perot cavity, the resonator length must be an integer number of half-wavelengths in order for a stable standing wave pattern to be established. For a cavity with mirrors at positions z_1 and z_2, the phase shift experienced by the $\mathrm{TEM}_{\ell,m}$ mode in one complete pass through the resonator needs to be a multiple of 2π (or a half-pass needs to be a multiple of π) which can be expressed as:

$$\theta_{\ell,m}(z_2) - \theta_{\ell,m}(z_1) = q\pi, \tag{2.29}$$

where q is an integer and $\theta_{\ell,m}(z)$ is the phase change of the wave in the direction of propagation, given by:

$$\theta_{\ell,m}(z) = kz - (\ell + m + 1)\tan^{-1}\left(\frac{z}{z_o}\right), \tag{2.30}$$

where k is the wavenumber. The phase shift experienced by the mode during reflection at the mirrors is omitted, as it will cancel out in subsequent derivations.

Using this equation, the resonance condition becomes:

$$k_q d - (\ell + m + 1)\left[\tan^{-1}\left(\frac{z_2}{z_o}\right) - \tan^{-1}\left(\frac{z_1}{z_o}\right)\right] = q\pi, \tag{2.31}$$

where $d = z_2 - z_1$ is the resonator length. For the fundamental $\mathrm{TEM}_{0,0}$ modes, the free spectral range can be found:

$$k_{q+1} - k_q = \frac{\pi}{d}, \tag{2.32}$$

or, after substituting $k = 2\pi\nu n/c$,

$$\nu_{q+1} - \nu_q = \frac{c}{2nd}, \tag{2.33}$$

which is the same as the result obtained for the planar Fabry-Perot cavity. In the case of transverse Hermite-Gaussian modes, the resonance frequency depends on the sum of ℓ and m, rather than on ℓ and m separately. Therefore, modes with the same $\ell + m$ value will be degenerate, meaning at the same resonance frequency. Given this property, the frequency separation between two adjacent transverse modes ($\Delta\nu_{HG}$) can be found:

$$(k_1 - k_2)\, d = \left[(\ell + m + 1)_1 - (\ell + m + 1)_2\right]\left[\tan^{-1}\left(\frac{z_2}{z_o}\right) - \tan^{-1}\left(\frac{z_1}{z_o}\right)\right], \tag{2.34}$$

and:

$$\Delta\nu_{HG} = \frac{c}{2\pi nd}\Delta(\ell + m)\left[\tan^{-1}\left(\frac{z_2}{z_o}\right) - \tan^{-1}\left(\frac{z_1}{z_o}\right)\right]. \tag{2.35}$$

where $\Delta(\ell + m)$ is the difference in the sums of the mode indices for two adjacent transverse modes. In the case of a near-planar resonator such as the microcavities studied in this thesis (see Chapter 3), where $d \ll R_1$ and R_2 and therefore z_1 and

$z_2 \ll z_o$ [4], Equation 2.35 becomes:

$$\Delta v_{HG} \cong \frac{c}{2\pi n z_o} \Delta (\ell + m). \tag{2.36}$$

The resonant frequencies of the transverse modes can also be calculated by manipulating Equation 2.31:

$$v_{q,\ell,m} = \frac{c}{2nd} \left\{ q + \frac{(\ell + m + 1)}{\pi} \cos^{-1} \left[\sqrt{\left(1 - \frac{d}{R_1}\right)\left(1 - \frac{d}{R_2}\right)} \right] \right\}. \tag{2.37}$$

For the half-symmetric microcavities in this thesis, for which $R_2 = \infty$, Equation 2.37 simplifies to:

$$v_{q,\ell,m} = \frac{c}{2nd} \left\{ q + \frac{(\ell + m + 1)}{\pi} \cos^{-1} \left[\sqrt{\left(1 - \frac{d}{R_1}\right)} \right] \right\}. \tag{2.38}$$

2.2.3 Other high-order Gaussian modes

The high-order Hermite-Gaussian modes defined by Equation 2.24 are part of a set of orthogonal solutions to the paraxial wave equation, a simplification of the general wave equation that assumes the wavefront of the lightwave travels either parallel or near-parallel to the optical axis. It is given by:

$$\frac{\partial^2 \psi}{\partial x^2} + \frac{\partial^2 \psi}{\partial y^2} - i2k \frac{\partial \psi}{\partial z} = 0, \tag{2.39}$$

where ψ is a complex factor determining how the wave in the resonator differs from a uniform plane wave, i.e.:

$$E = E_o \psi e^{-ikz}. \tag{2.40}$$

Another valid set of modes is obtained when the solution is written in terms or

cylindrical coordinates (r, ϕ, z) instead of rectangular coordinates. These modes are called the Laguerre-Gaussian modes, and are generally of the form [6]:

$$\begin{aligned} E_{p,l} =& E_o \left[\frac{\sqrt{2}r}{\omega(z)}\right] L_{p,l}\left(\frac{2r^2}{\omega^2(z)}\right) \\ & \times \exp\left[-\frac{r^2}{\omega^2(z)} \pm il\phi - ik\frac{r^2}{2R(z)} - ikz + i(2l+p+1)\eta\right], \end{aligned} \tag{2.41}$$

where $L_{p,l}$ is the associated Laguerre polynomial for the (p,l) mode, and p and l are the mode indices for the radial and azimuthal coordinate directions, respectively. These modes will be favoured in structures with high cylindrical symmetry, such as optical fibres and the domes studied in this thesis, although defects in the shape of the structure will allow the existence of Hermite-Gaussian modes, and in many cases favour them. For example, real lasers tend to heavily favour the Hermite-Gaussian modes with even small rectangular symmetry added by tilted surfaces or defects [8]. Examples of the Laguerre-Gaussian modes are shown in Figure 2.6.

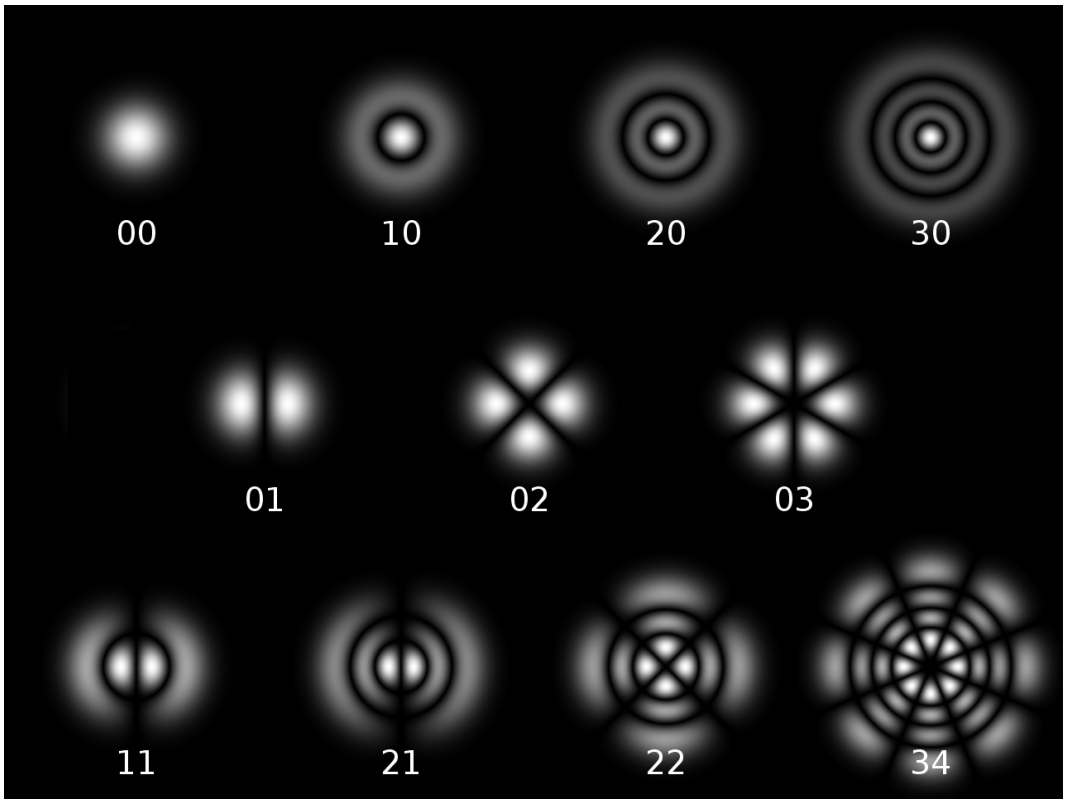

Figure 2.6: Examples of Laguerre-Gaussian modes [7].

In addition, there is a third family of modes that are also exact solutions of the paraxial wave equations, and make up the transition between the Hermite and Laguerre modes. These modes, called the Ince-Gaussian modes [9], have elliptical symmetry and can be observed in structures whose cylindrical or rectangular symmetry is slightly broken [10]. There are two expressions in elliptical coordinates for the Ince-Gaussian modes based on the even and odd Ince polynomials [11]:

$$\begin{aligned} E_{even} =& C_{even}\frac{\omega_o}{\omega(z)}C_p^m(i\xi,\varepsilon)\,C_p^m(\varphi,\varepsilon) \\ & \times\exp\left[-\frac{r^2}{\omega^2(z)}+ik\frac{r^2}{2R(z)}+ikz-i(p+1)\,\eta\right], \end{aligned} \tag{2.42}$$

$$E_{odd} = S_{odd} \frac{\omega_o}{\omega(z)} S_p^m(i\xi, \varepsilon) S_p^m(\varphi, \varepsilon) \times \exp\left[-\frac{r^2}{\omega^2(z)} + ik\frac{r^2}{2R(z)} + ikz - i(p+1)\eta \right], \tag{2.43}$$

where C_p^m and S_p^m are the even and odd Ince polynomials of order p and degree m, respectively, C_{even} and S_{odd} are normalization constants, (ξ, φ) are transverse coordinates of the traveling wave, and ε is an ellipticity parameter. Hermite and Laguerre-Gaussian modes are actually special case Ince modes with $\varepsilon = \infty$ and $\varepsilon = 0$, respectively. Some examples of Ince modes are shown in Figure 2.7, along with a few similar field patterns that were observed in the domes studied in Chapter 3.

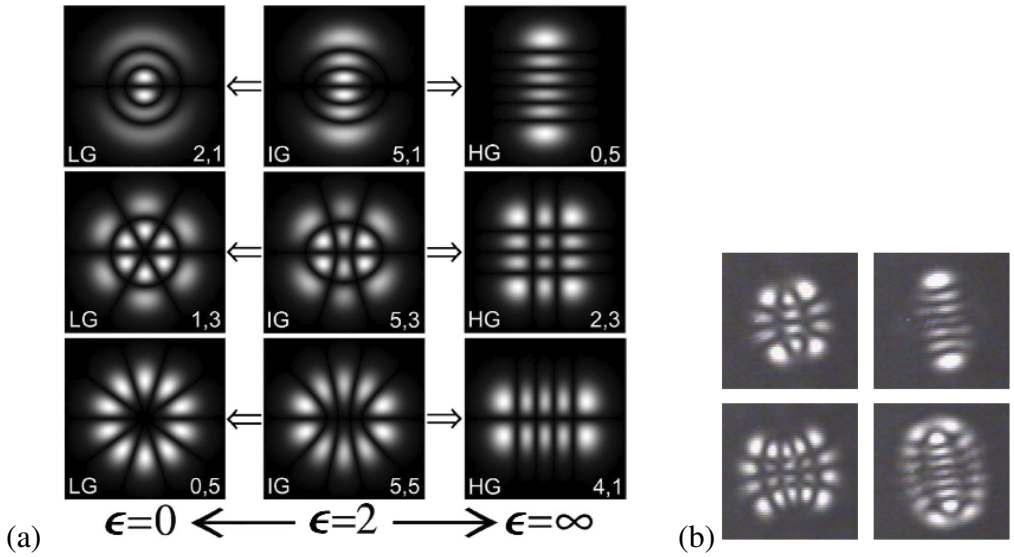

Figure 2.7: (a) Transverse shapes of Laguerre, Ince and Hermite-Gaussian modes for modes with the same degeneracy [11]. (b) Ince-Gaussian-like modes observed in some of the microdomes discussed in Chapter 3.

2.3 Induced transmission/potential transmittance

The concept of potential transmittance was developed by Berning and Turner in 1957 [12] as a tool to optimize the transmittance of light through absorbing metal films, particularly in the case of bandpass filters. At the time, it was well known that

surrounding a metal film with appropriate interference film structures could greatly enhance the transmission of light through that film at a certain wavelength. In their 1957 paper [12], Berning and Turner put forth a theory that allowed for strict design of metal-dielectric-metal filters using this property.

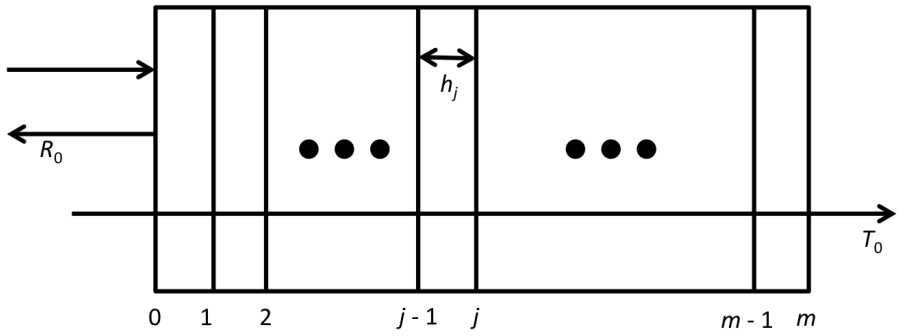

Figure 2.8: General multilayer film structure.

Figure 2.8 shows an arbitrary film structure consisting of m isotropic, homogeneous plane-parallel layers, with one or more absorbing layers with complex refractive index given by $N_j = n_j - ik_j$. T_0 and R_0 are the overall transmission and reflectance of the structure when it is exposed to normal-incidence light of wavelength λ from the external surrounding medium with refractive index n_0. From the definitions of the time-averaged numerical magnitudes of the Poynting vectors at the incident and exit surfaces of the structure (I_0 and I_m, respectively):

$$\frac{T_0}{1-R_0} = \frac{I_m}{I_0}, \tag{2.44}$$

where I at any point in the structure is given by $I = \frac{1}{2}\mathrm{Re}\{EH^*\}$, and E and H are the electric and magnetic field intensities at that point. The overall ratio I_m/I_0 can also be expressed as a product of the ratios of the power entering and exiting each individual absorbing layer of the structure, i.e.:

$$\frac{T_0}{1-R_0} = \prod_j \left(\frac{I_j}{I_{j-1}} \right), \tag{2.45}$$

where j refers to the absorbing film between the jth and $(j-1)$th boundaries, with n_j and $k_j > 0$. It is not necessary to include non-absorbing films, as the power entering them is equal to the power exiting (i.e.: $I_{k-1} = I_k$, where k denotes a non-absorbing film). The ratio $I_j / \left(I_{j-1}\right)$, dubbed the "potential transmittance" of the jth layer by Berning and Turner, is the ratio of net radiant flux transmitted past the jth boundary to that transmitted past the $(j-1)$th boundary. They also gave an equation that can be used to calculate the potential transmittance of the film directly:

$$\mathrm{PT}_j = \frac{1 - |r_j|^2 - 2\left(k_j/n_j\right)|r_j| \sin\rho_j}{\exp\left(\frac{4\pi k_j h_j}{\lambda}\right) - |r_j|^2 \exp\left(-\frac{4\pi k_j h_j}{\lambda}\right) - 2\frac{k_j}{n_j}|r_j| \sin\left(\rho_j - \frac{4\pi n_j h_j}{\lambda}\right)}, \tag{2.46}$$

where $r_j = |r_j| \exp(i\rho_j)$ is the reflectance coefficient at the interface between the jth layer and the $(j-1)$th layer. r_j is related to the normalized admittance ($Y_j = \left(H_j/E_j\right)/Y_o$, where Y_o is the impedance of free space) at the jth boundary by:

$$r_j = \frac{N_j - Y_j}{N_j + Y_j}. \tag{2.47}$$

From Equation 2.46, Berning and Turner noted that the potential transmittance of a layer only depends on its index (N_j), its thickness (h_j), and on the admittance Y_j, and therefore does not depend on the structure to the left of the film or the *specific* structure to the right. In addition, they noted that the product of the individual potential transmittances of the layers (Equation 2.45) can be viewed as the overall potential transmittance of the entire multilayer structure. The potential transmittance will also have a maximum value for any given fixed refractive index and thickness, and this value can be used to find the exit admittance needed to

maximize transmittance through the film structure. These calculations will be discussed in more detail later in the thesis. As well, the following paragraphs will introduce the terminology and theory used for those calculations, as described by Macleod [13].

Put in different terms, the potential transmittance of a layer is the ratio of intensity exiting the layer's rear interface to the intensity entering the layer after reflections at the front surface.

$$\mathrm{PT} = \frac{I_{exit}}{I_{enter}} \tag{2.48}$$

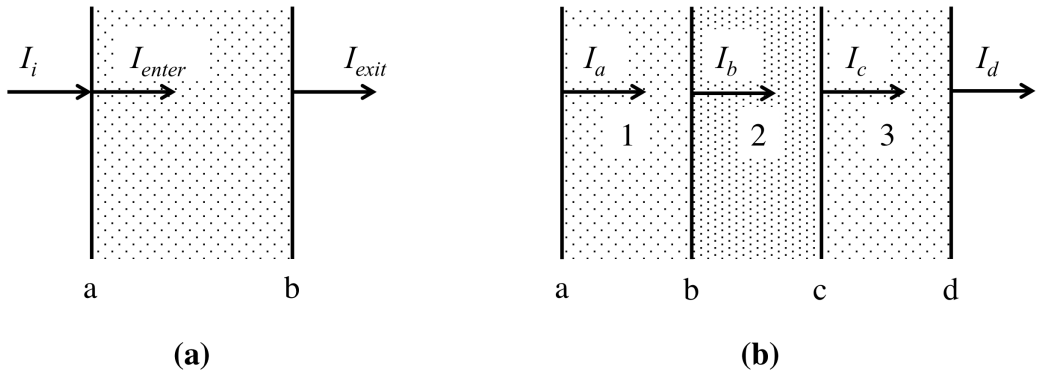

Figure 2.9: Naming conventions for (a) a single layer and (b) a multilayer. In the overall multilayer structure, $I_a = I_{enter}$ and $I_d = I_{exit}$.

When I_{exit} and I_{enter} are expressed in terms of the incident intensity (I_i), transmittance (T) and reflectance (R) of the layer:

$$\mathrm{PT} = \frac{T}{1-R} = \frac{T}{A+T} = \frac{1}{1+A/T}, \tag{2.49}$$

where A is the absorptance of the layer ($A+R+T=1$). From its definition and from Equation 2.49, we see that the potential transmittance is independent of reflections at the surface of the film, meaning it is unaffected by changes made to the structure at the input of the layer. In other words, the potential transmittance is

the transmittance of light through the film that would be obtained if the reflections at the front surface were reduced to zero. The factors that do affect the potential transmittance are the properties of the film itself and the admittance of the exit structure. Also, since the properties of the film are fixed, it will have a maximum potential transmittance obtainable by a specific exit structure admittance, which can be calculated from the properties of the metal layer. In addition, the PT of a series of N layers can be found by multiplying their individual PTs, that is:

$$\mathrm{PT} = \mathrm{PT}_1\mathrm{PT}_2\mathrm{PT}_3 \ldots \mathrm{PT}_N, \tag{2.50}$$

which is apparent if the PT of the overall structure is split into its separate components, as seen in the example in Figure 2.9:

$$\mathrm{PT} = \frac{I_{exit}}{I_{enter}} = \frac{I_d}{I_a} = \frac{I_b}{I_a}\frac{I_c}{I_b}\frac{I_d}{I_c} = \mathrm{PT}_1\mathrm{PT}_2\mathrm{PT}_3. \tag{2.51}$$

The same property also applies to the maximum potential transmittances ($\mathrm{PT_{MAX}} = \mathrm{PT_{1,MAX}PT_{2,MAX}PT_{3,MAX}} \ldots \mathrm{PT_{N,MAX}}$).

Two methods for finding the ideal exit admittance have been outlined by MacLeod [13] and Baumeister [14], although in the interest of brevity only the MacLeod method will be outlined in this thesis. It begins by looking at the linear relationship between the electric and magnetic fields entering and exiting the metal film:

$$\begin{bmatrix} E_{in} \\ H_{in} \end{bmatrix} = [M] \begin{bmatrix} E_{out} \\ H_{out} \end{bmatrix}, \tag{2.52}$$

where $[M]$ is the characteristic matrix of the metal film, given by:

$$[M] = \begin{bmatrix} \cos\delta_M & (i\sin\delta_M)/Y \\ iY\sin\delta_M & \cos\delta_M \end{bmatrix}, \tag{2.53}$$

where the term $\delta_M = 2\pi(n - i\kappa)d/\lambda$ is the complex phase thickness of the metal and $Y = n - i\kappa$ is the admittance of the metal film in free space units (normalized to the admittance of free space, Y_o). Since the admittance of the output structure is defined as $Y_{out} = H_{out}/E_{out}$, normalizing Equation 2.52 by dividing both sides by E_{out} gives:

$$\begin{bmatrix} B \\ C \end{bmatrix} = [M] \begin{bmatrix} 1 \\ Y_{out} \end{bmatrix}, \tag{2.54}$$

where $B = E_{in}/E_{out}$ and $C = H_{in}/E_{out}$. The potential transmittance can be expressed in terms of B, C, and Y_{out} as follows [13]:

$$\mathrm{PT} = \frac{\mathrm{Re}(Y_{out})}{\mathrm{Re}(BC^*)}. \tag{2.55}$$

Expressing Y_{out} as $X + iZ$, and performing a great deal of arithmetic gives an equation for PT in terms of the admittance components:

$$\mathrm{PT} = \left(\begin{array}{c} \frac{\left(n^2-\kappa^2\right)-2n\kappa(Z/X)}{\left(n^2+\kappa^2\right)}\left(\sin^2\alpha\cosh^2\beta + \cos^2\alpha\sinh^2\beta\right) \\ +\left(\cos^2\alpha\cosh^2\beta + \sin^2\alpha\sinh^2\beta\right) \\ +\frac{1}{X}\left(n\sinh\beta\cosh\beta + \kappa\cos\alpha\sin\alpha\right) \\ +\frac{X^2+Z^2}{X\left(n^2+\kappa^2\right)}\left(n\sinh\beta\cosh\beta - \kappa\cos\alpha\sin\alpha\right) \end{array} \right)^{-1}, \tag{2.56}$$

where α and β are the real and imaginary components of δ_M, respectively, i.e., $\delta_M = \alpha - i\beta$, where $\alpha = 2\pi nd/\lambda$ and $\beta = 2\pi\kappa d/\lambda$. From here the values for X and Z that maximize PT can be found:

$$X = \left(\begin{array}{c} \frac{\left(n^2+\kappa^2\right)(n\sinh\beta\cosh\beta+\kappa\cos\alpha\sin\alpha)}{(n\sinh\beta\cosh\beta-\kappa\cos\alpha\sin\alpha)} \\ -\frac{n^2\kappa^2\left(\sin^2\alpha\cosh^2\beta+\cos^2\alpha\sinh^2\beta\right)}{(n\sinh\beta\cosh\beta-\kappa\cos\alpha\sin\alpha)^2} \end{array} \right)^{1/2} \tag{2.57}$$

$$Z = \frac{n\kappa\left(\sin^2\alpha\cosh^2\beta+\cos^2\alpha\sinh^2\beta\right)}{(n\sinh\beta\cosh\beta-\kappa\cos\alpha\sin\alpha)} \tag{2.58}$$

The values calculated for X and Z can be substituted back into Equation 2.56 to find $\mathrm{PT_{MAX}}$.

Once X and Z are known, a stack of dielectric layers can be designed to admittance match the metal layer to the surrounding medium or substrate. As an example, for a silver film of thickness 70 nm, the expected maximum potential transmittance is $\simeq 80.5\%$ at a wavelength of 550 nm. Macleod [13] describes a structure to match the admittance of this film at 550 nm as follows:

$$\mathrm{Glass}\,|\,HLHLHL\prime\,|\,\mathrm{Ag}\,|\,L\prime HLHLH\,|\,\mathrm{Glass}, \tag{2.59}$$

where $n_{Glass} = 1.52$, $N_{\mathrm{Ag}} = 0.055 - i3.32$, H represents a dielectric layer of optical thickness $0.25\lambda_0$ and index 2.35, L represents a dielectric layer of optical thickness $0.25\lambda_0$ and index 1.35, and $L\prime$ represents a layer of optical thickness $0.4417\lambda_0$ and index 1.35. Since the multilayers produce a narrowband admittance matching of the Ag film, the overall structure acts as a bandpass filter, as seen in Figure 2.10.

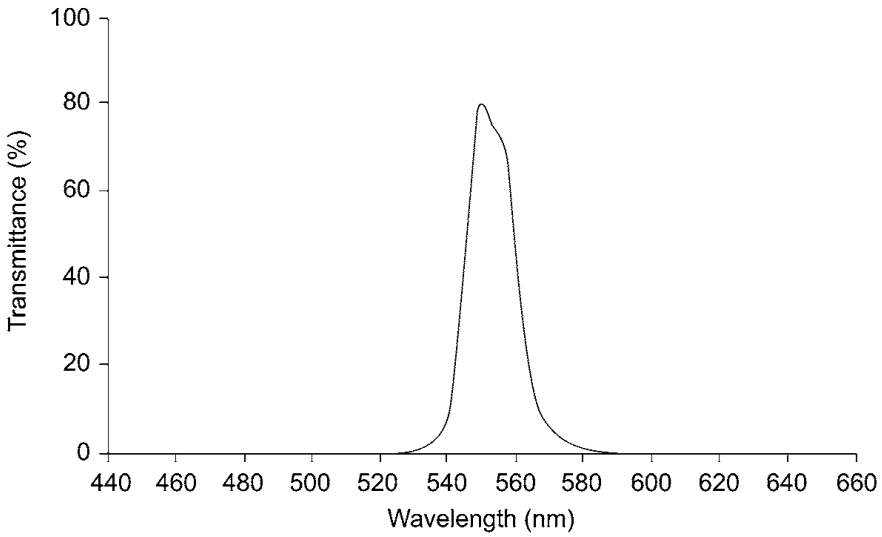

Figure 2.10: Calculated transmission of 550-nm filter design [13].

As expected, the filter reaches a peak transmittance of 80% at 550 nm. In addition, the out-of-band rejection of the filter can be improved by adding extra metal layers, at a cost to overall transmission. Because the induced transmission filter can be viewed as a pair of Fabry-Perot resonant cavities (the L' layers act as cavity cores surrounded by the mirrors formed by the Ag layer and the HL quarter-wave stack multilayers), the transmission band has two peaks because of mode splitting caused by coupling between the two cavities [15]. The transmission of the multi-metal layer structure, assuming perfect admittance matches to the exit and entrance media, will be equal to the products of the individual layer transmittances, as stated in Equation 2.50. Additionally, the overall potential transmittance of a filter with multiple metal layers will be greater than that of a filter containing the same amount of thickness in a single metal layer. This property is discussed further in Chapter 4.

Another interesting property of the potential transmittance relates to the absorptance of absorbing layers. Normally, the bulk absorption coefficient α_{bulk} of an absorbing medium can be determined from the transmission through that

medium in the absence of reflection:

$$\alpha_{bulk} = -\frac{\ln(T)}{d}, \tag{2.60}$$

where d is the thickness of the medium. However, if this equation is applied to the maximum potential transmittance in a structure with one or more metal layers that are correctly admittance-matched with dielectric layers, we can define:

$$\alpha_{eff} = -\frac{\ln(\mathrm{PT_{MAX}})}{d_{total}}, \tag{2.61}$$

where d_{total} is the sum of all metal layer thicknesses. Therefore α_{eff} is an effective absorption coefficient, which for thin metal films is much lower than that predicted by the bulk value. As an example, Figure 2.11 plots effective absorption coefficient for a range of Ag film thicknesses at $\lambda_0 = 550$ nm:

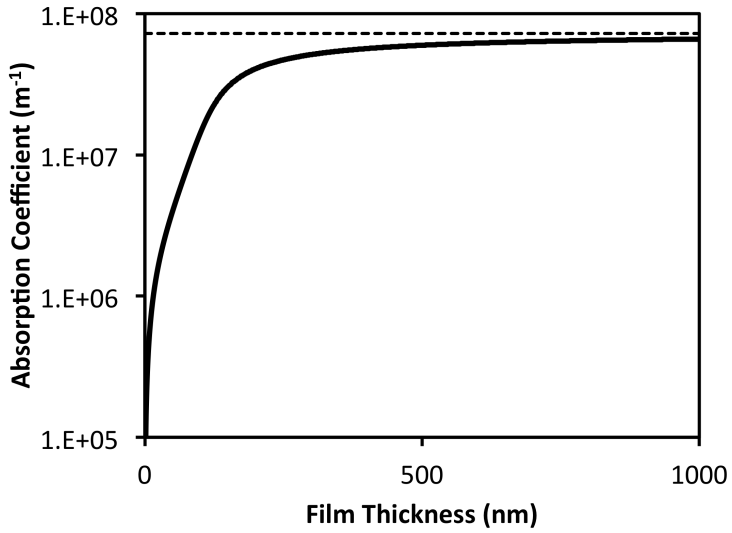

Figure 2.11: Effective absorption coefficient versus Ag film thickness for 550-nm light with normal incidence. For comparison, the dashed line shows the bulk absorption coefficient for Ag at 550 nm.

As can be seen, the effective absorption coefficient is lower than that of the bulk value for a wide range of thicknesses, and is as much as nearly two orders of

magnitude lower for Ag films in the 10-nm thickness range. It is well-known that the properties of very thin films (such as complex refractive index N) can deviate from their bulk values, which would affect results as they are assumed to be constant in the calculation of PT_{MAX}. However, films of Ag as thin as 10 nm have been deposited with no significant change from the bulk values [16] and therefore the results past this thickness can be considered reasonably accurate. In addition, α_{eff} for a series of metal layers (optimally admittance matched) will be the same as that obtained for a single metal layer of equivalent thickness. This property shows the dramatic effect admittance matching has on transmission through metal-dielectric systems. These points are discussed in greater detail in Chapters 4 and 5.

References

[1] M.-W. Moon, K.-R. Lee, K.H. Oh, J.W. Hutchinson, "Buckle delamination on patterned substrates", *Act. Mat.*, vol. 52, pp. 3151-3159, 2004.

[2] J.W. Hutchinson, M.D. Thouless, E.G. Liniger, "Growth and configurational stability of circular, buckling-driven film delaminations", *Acta. Metall. Mater.*, vol. 40, pp. 295-308, 1992.

[3] V.K. Khanna, "Adhesion-delamination phenomena at the surfaces and interfaces in microelectronics and MEMS structures and packaged devices", *J. Phys. D: Appl. Phys.*, vol. 44, pp. 1-19, 2011.

[4] A. Yariv, *Optical Electronics in Modern Communications*. Oxford University Press, 1997.

[5] J.T. Verdeyen, *Laser Electronics, 3rd Edition*. Prentice Hall, 1995.

[6] S. Ramo, J.R. Whinnery, T. Van Duzer, *Fields and Waves in Communication Electronics, 3rd Edition*. John Wiley & Sons, 1994.

[7] ”DrBob” at en.wikipedia, *Gaussian Beam: Higher Order Modes*. (Online, 2004). Available at: http://en.wikipedia.org/wiki/Gaussian_beam#Higher-order_modes (Accessed March 1, 2011).

[8] A.E. Siegman, *Lasers*. University Science Books, 1986.

[9] M.A. Bandres, J.C. Gutiérrez-Vega, “Ince-Gaussian beams”, *Opt. Lett.*, vol. 29, pp. 144-146, 2004.

[10] U.T. Schwarz, M.A. Bandres, J.C. Gutiérrez-Vega, “Observation of Ince-Gaussian modes in stable resonators”, *Opt. Lett.*, vol. 29, pp. 1870-1872, 2004.

[11] M.A. Bandres, J.C. Gutiérrez-Vega, “Ince-Gaussian modes of the paraxial wave equation and stable resonators”, *J. Opt. Soc. Am. A*, vol. 21, pp. 873-880, 2004.

[12] P.H. Berning, A.F. Turner, “Induced transmission in absorbing films applied to band pass filter design”, *J. Opt. Soc. Am.*, vol. 47, pp. 230-239, 1957.

[13] H.A. Macleod, *Thin-Film Optical Filters, 3rd Edition*. Institute of Physics Publishing, 2001.

[14] P.W. Baumeister, “Radiant power flow and absorptance in thin films”, *Appl. Opt.*, vol. 8, pp. 423-436, 1969.

[15] H. van de Stadt, J.M. Muller, “Multimirror Fabry-Perot interferometers”, *J. Opt. Soc. Am. A*, vol. 2, pp. 1363-1370, 1985.

[16] J.A. Scholl, A.L. Koh, J.A. Dionne, “Quantum plasmon resonances of individual metallic nanoparticles”, *Nature*, vol. 483, pp. 421-428, 2012.

3 High-finesse cavities fabricated by buckling self-assembly of a-Si/SiO_2 multilayers[1]

3.1 Introduction and background

MEMS-based Fabry-Perot cavities have many applications in fibre and sensing systems and for fundamental physics studies. However, the quality factor (Q) and finesse (F) of flat-mirror cavities has typically been limited by defects such as surface roughness and non-parallelism or uncontrolled curvature of the mirrors [1, 2]. Furthermore, to mitigate finesse reduction arising from walk-off of non-collimated beams, flat-mirror cavities typically must operate in a low mode order with relatively large lateral dimensions [3]. Tayebati *et al*. [4] demonstrated half-symmetric cavities with improved stability and finesse, by using thin-film stress to control the curvature of a tethered mirror in a surface micromachining process. Similar results were obtained by Halbritter *et al*. [5], using a bulk (two-wafer) micromachining process. Half-symmetric cavities with $F \sim 3 \times 10^3$ are reportedly used in commercial MEMS-based micro-spectrometers [6].

Curved mirror resonators have also been applied to the study of cavity quantum electrodynamics (CQED), including Bose-Einstein condensation [7], cavity optomechanics [8], and optical interrogation of single atoms [9]. For these studies, open-access air-core cavities with ultra-high finesse and low modal volume (V_m) are sought [10]. Since mirror roughness and shape deformations can ultimately limit the finesse, researchers have used novel fabrication processes such as transfer of a thin-film mirror from a lens to a fibre [7], CO_2-laser ablation of glass fibres or substrates [9], and focused ion beam drilling in silicon [10]. Recently, single cavities with $F > 10^5$ [11] and arrays of microcavities with $F \sim 460$ [10] have been reported. For the most part, the devices mentioned were fabricated using

[1] This chapter was published as a paper in *Optics Express*, vol. 19, pp. 18903-18909, 2011.

relatively time-consuming, serial processing techniques. For applications in lab-on-chip systems, there is a need for parallel fabrication of microcavity arrays [12].

Here, we describe a method that employs standard silicon processing steps (film deposition, lithography) to produce variable-size microcavities on a single chip. Circular regions of low adhesion were embedded within Si/SiO_2 multilayer stacks, and delamination buckles were subsequently induced to form in these regions. The resulting structures closely resemble half-symmetric resonators with one flat mirror and one nearly spherical mirror, and their optical properties were found to be in excellent agreement with the well-known predictions (derived from the paraxial wave equation) for macroscopic cavities of that type. Due to the nearly perfect symmetry of the cavities, modes from both the Laguerre-Gaussian and Hermite-Gaussian basis sets could be coupled and observed. The cavities exhibit F as high as 3×10^3 and Q as high as 4×10^4.

3.2 Fabrication and morphology of buckled dome microcavities

General details of the fabrication process were provided elsewhere [13] in the context of air-core waveguide channels, but a brief summary is as follows. First, a Bragg mirror (4 periods of SiO_2 and a-Si) was deposited by reactive magnetron sputtering onto a double-side-polished Si wafer. Next, a low adhesion, vapor-phase deposited fluorocarbon layer ($\sim$ 10 nm thick) was patterned on the top (a-Si) surface of this mirror. Subsequently, a second 4-period mirror (starting with a-Si), capped by a double-thickness a-Si layer, was deposited. All layers in both the upper and lower mirror were targeted as quarter-wave layers at 1550 nm, except for the half-wavelength (latent) capping layer. The capping layer was added to increase the stiffness of the upper mirror, thereby improving the thermal stability as discussed below. The total thickness of the upper mirror with capping layer is

$\sim$ 1.7 μm. Sputtering parameters were as described previously [13], except that here we used a slightly lower background pressure (3 mTorr) for the a-Si layers and a slightly higher substrate temperature (170 °C). For magnetron sputtered a-Si, these conditions have been associated with higher film density, higher index, and lower loss [14]. Our process produced a-Si layers with refractive index ~ 3.7 and extinction coefficient ~ 0.001 at 1550 nm, as estimated from VASE measurements. The SiO_2 layers were estimated to have refractive index ~ 1.47 in the same range. Using well-known formulae (and confirmed by transfer matrix results), these values imply a best-case reflectance $R \sim 0.999$ for the 4-period mirrors, corresponding to a best-case (reflectance-limited) finesse $F_R \sim 3140$ in the absence of defects.

After deposition of the upper mirror, samples were placed on a hot plate and subjected to an empirically optimized heating process, to induce loss of adhesion between the upper and lower Bragg mirrors in the regions of the embedded fluorocarbon. The multilayers exhibit an effective medium compressive stress $\sim$ 200 MPa immediately after deposition, and this stress reduces with subsequent annealing [13]. From numerous trials, delamination buckles formed at a sample-dependent temperature, typically in the 250- to 350-°C range. Variation in the buckling temperature is likely due to uncontrolled variation in the properties (i.e. thickness, roughness) of the fluorocarbon layer, although this is the subject of ongoing work. In any case, it results in uncertainty regarding the effective stress at the time of buckle formation.

As shown schematically in Figure 3.1(a), the compressive stress causes the upper Bragg mirror to buckle away from the substrate, producing a hollow cavity between a curved mirror and a flat mirror. Within a certain range of diameter for a given net stress, the circular delamination produced a dome-shaped buckle with a nearly spherical shape at its centre. The cavities have diameters in the 100- to

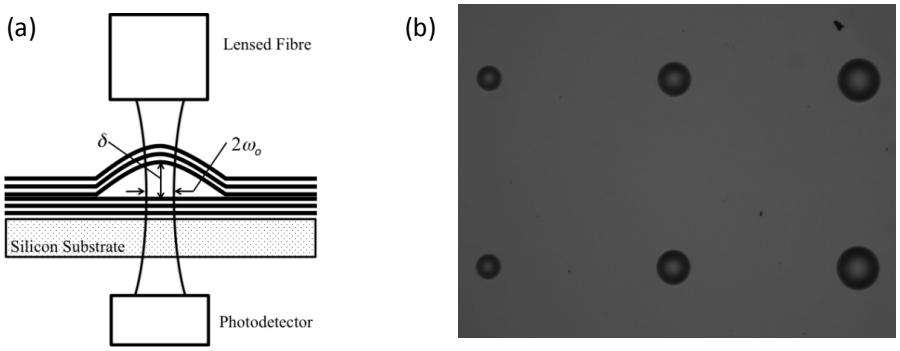

Figure 3.1: Buckled dome microcavities: (a) schematic cross-section showing optimized coupling to the fundamental cavity mode by a nearly Gaussian beam (with waist radius ω_0) from a lensed fibre. For most cavities tested, the fibre mode field diameter was actually larger than $2\omega_0$, resulting in the excitation of multiple modes. (b) Microscope image of pairs of 150-, 200-, and 250-μm diameter domes. Some dust particles are also visible.

800-μm range and peak heights in the $\sim$ 2- to 25-μm range. However, larger buckles exhibited greater deviation from a spherical shape, such as partial collapse or flattening of the central region. In the following, we focus mainly on buckles with diameters of 400 μm or less (see Figure 3.1(b)), which exhibited the best morphology and optical properties.

Neglecting plastic deformation, the theory for elastic buckling of a clamped circular plate can be used to predict the preconditions and height of a circular delamination buckle [15]. The critical buckling stress is $\sigma_c = 1.2235\left[E/\left(1-v^2\right)\right](h/a)^2$, where E is Young's modulus, v is Poisson's ratio, and h and $a = D/2$ are the thickness and radius of the plate. For a given stress and assuming fixed E, v, and h, this implies a minimum diameter (D_{min}) for buckling to occur. For $D > D_{min}$, the peak deflection of the plate can be approximated as:

$$\delta = h\left[1.9\left(\frac{\sigma}{\sigma_c}-1\right)\right]^{1/2} \approx \left[\frac{1.9\sigma\left(1-v^2\right)}{1.2235E}\right]^{1/2}\frac{D}{2}, \tag{3.1}$$

where σ is the biaxial compressive stress, and the last approximation holds for

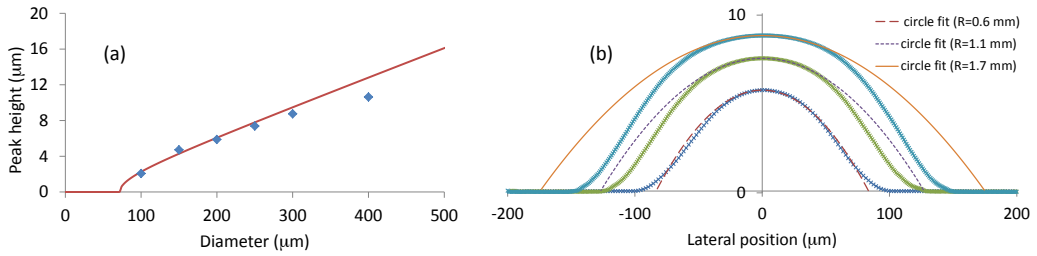

Figure 3.2: (a) The red curve shows peak height versus buckle diameter as predicted by elastic buckling theory, using the film parameters described in the main text and an effective medium compressive stress of 150 MPa. The blue symbols show dome height measured using a profilometer. An average height value is displayed when more than one dome height measurement is available. In these cases (200-, 250-, and 400-μm domes) the variation in heights range from ±1.2 to 5.8%. (b) The symbols show experimental profiles for representative 200-, 250-, and 300-μm diameter domes. The curves are circular sections with radius of curvature estimated by fitting the profile data from the top portion of each buckle, as described in the text.

$\sigma \gg \sigma_c$ (i.e. for $D \gg D_{min}$). Thus, for a given σ, ν, and E, and for $D \gg D_{min}$, Equation 3.1 predicts that buckle height will increase approximately linearly with diameter. However, Equation 3.1 is an approximate closed-form solution to a nonlinear problem [15], and is expected to over-estimate the height for large σ/σ_c (i.e. for large D). In fact, bifurcation to a nonaxisymmetric buckling mode is predicted at high values of stress (for $\sigma/\sigma_c > 56$ when $\nu = 1/3$ [15]).

Figure 3.2(a) shows average peak height versus diameter, as obtained from profilometer scans (Alpha-Step IQ, KLA-Tencor) on several domes of each diameter. From previous work [13] (and the layer thicknesses described above), we estimated effective medium parameters $h \sim 1.7$ μm, $E \sim 50$ GPa and $\nu \sim 0.3$ for the buckled mirror with the capping layer. Using these and a buckling stress $\sigma = 150$ MPa produced good agreement between Equation 3.1 and the measured heights. Consistent with the plot, Equation 3.1 is expected to be most accurate in the small diameter range, while over-estimating the height for large dome diameters.

The radius of curvature of the buckled mirror is a key parameter, since it determines the modal volume and the spacing of the high-order transverse modes. However, there is no closed-form expression for the profile of a circular buckled plate, even if the buckling is assumed to be an elastic deformation [15]. Moreover, thin-film buckling often deviates from the predictions of elastic theory, due to plastic deformation of the layers near the buckle boundaries [16]. Assuming for simplicity a perfectly spherical dome shape, the expected radius of curvature is given by:

$$R_{CD} = \frac{D^2}{8\delta} + \frac{\delta}{2}, \tag{3.2}$$

where D is the buckle diameter (i.e. chord length of the dome) and δ is the peak height of the buckle (i.e. the sagittal length of the spherical section).

The experimental radius of curvature was estimated by fitting to data from the scanning profilometer. Typical scans are shown in Figure 3.2(b), along with circular fits to the top portions of the buckled mirrors. Somewhat arbitrarily, but with the intent of capturing the curvature for the portion of the mirror sampled by the low-order cavity modes, the fit in each case was based on the profile data within ± 20 μm (along the lateral direction) of the peak. Smaller domes (diameters of 200 μm or less) exhibited an approximately spherical shape, whereas larger domes appear somewhat flattened at the top. This flattening is exacerbated by the force of the profilometer needle, which might also explain the slight asymmetry for the 200-μm dome. However, the same basic trends were also observed using a non-contact optical profilometer (Zygo). For the 200-, 250-, and 300-μm-diameter domes shown in Figure 3.2(b), Equation 3.2 predicts $R_{CD} \sim 0.9$, 1.1, and 1.3 mm, respectively. Rather than being flattened, the measured radius of curvature R_C (at the peak) of the smallest domes was smaller than the value predicted by Equation 3.2. This is reminiscent of the profile for a straight-sided (Euler) buckle [15],

$w(x) = (\delta/2)[1+\cos(\pi x/a)]$, where w is the vertical deflection, x is the distance across the buckle, and a is the half-width of the buckle, which exhibits minimum radius of curvature at its centre.

3.3 Optical properties and characterization

Assuming a spherical shape for the buckled upper mirror, the domes form half-symmetric Fabry-Perot cavities [4]. Depending on the degree of cylindrical symmetry, mode-fields for such cavities are traditionally described using one of two alternative sets of orthogonal basis functions [17, 18]. In a rectangular coordinate system, the solutions are Hermite-Gaussian (HG) functions $H_{\ell,m}(x,y,z)$, where ℓ and m are integer mode indices for the x and y transverse coordinates. In a cylindrical coordinate system, the solutions are Laguerre-Gaussian (LG) functions $L_{p,l}(r,\phi,z)$, where p and l are integer mode indices for the radial and azimuthal coordinate directions, respectively. In most macroscopic cavities, deviation from cylindrical symmetry is significant so that it is predominately HG modes that are observed experimentally [18]. However, a predominance of LG modes has been reported for some microcavities [19].

Each family of solutions forms a complete set of orthogonal basis functions, so that a given HG mode can be expressed as a linear weighted sum of degenerate LG modes, or vice-versa [20]. The degeneracy condition requires that the modes have equivalent Gouy phase shift, and is expressed as follows:

$$g = \ell + m = 2p + l. \tag{3.3}$$

For example, the $HG_{1,1}$, $LG_{1,0}$, and $LG_{0,2}$ modes form a nominally degenerate set. Degenerate modes are expected to share the same resonance frequency, although slight imperfections (such as deviations from spherical mirror symmetry)

Table 3.1: Predicted and measured optical properties for representative microcavities. Predicted values are based on the measured peak height and effective radius of curvature near the peak, as described in the text.

Cavity diameter (μm)	Cavity height (μm)	Estimated Radius of Curvature (mm)	Predicted FSR (nm)	Predicted Rayleigh Range z_o (μm)	Predicted fundamental spot size $2\omega_o$ (μm)	Predicted $\Delta\lambda_T$ (nm)	Measured $\Delta\lambda_T$ (nm)	Measured FWHM (nm)	Measured Q-Factor	Measured Finesse
200	5.68	0.62	210	59	11.0	7.0	6.1	0.08	2.1E+04	2.7E+03
250	7.47	1.09	160	90	13.5	4.5	4.3	0.05	3.2E+04	3.2E+03
300	8.75	1.75	130	123	15.6	3.1	3.0	0.05	3.1E+04	2.6E+03
400	10.49	4.98	120	228	21.6	1.8	2.0	0.04	4.0E+04	3.0E+03

will perturb this degeneracy [10]. For $R_C \gg \delta$, the nominal wavelength spacing between non-degenerate transverse spatial modes can be approximated [17] as:

$$\Delta\lambda_T = \frac{\lambda^2}{2\pi z_o}\Delta g, \tag{3.4}$$

where λ is the resonant wavelength, and z_o is the Rayleigh range, of the fundamental cavity mode. Table 1 shows predicted and measured mode properties for 4 representative cavities, where the predictions are based on the R_C fit described above (± 20 μm from the peak).

Optical properties of the cavities were tested using the experimental setup illustrated in Figure 3.1(a). Light from a tunable laser was coupled into the cavities via a lensed optical fibre with focal spot diameter ~ 20 μm, somewhat larger than the fundamental mode field diameter for most of the cavities tested. This resulted in significant coupling to higher-order spatial modes. However, lower-order modes could be isolated and imaged by tuning the laser to the corresponding resonant wavelength of a given mode. Transmitted light was captured by either an infrared camera or a cooled photodetector.

Given the estimated mirror reflectance (~ 0.999), the circulating power at resonance is predicted to be greater than 1000 times the incident power [17]. Even for low input power (< 0.1 mW), significant drift (on the time scale of seconds) in the transmitted power was observed when the laser was tuned to a fundamental

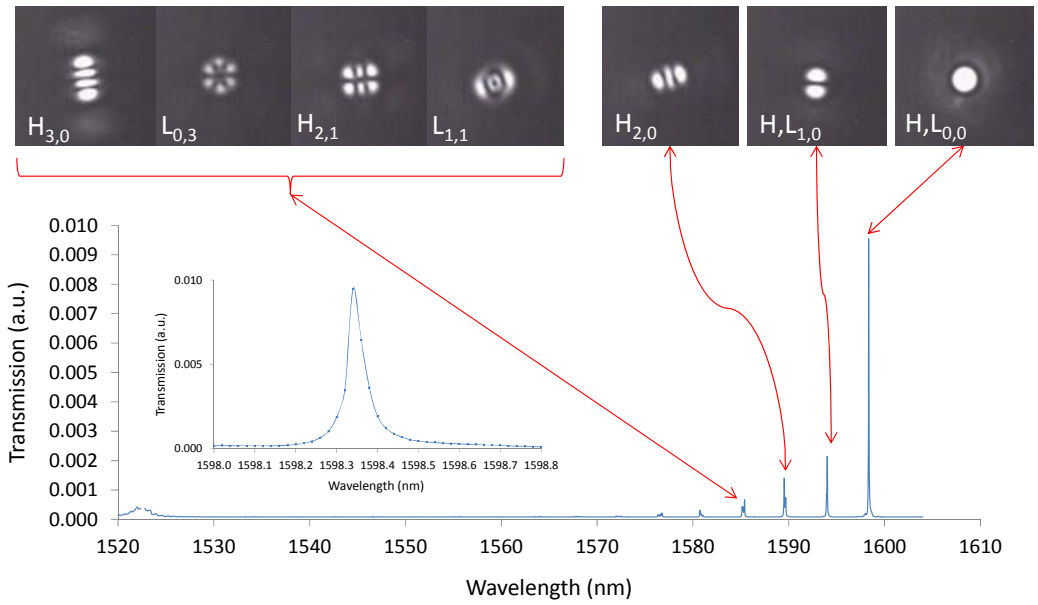

Figure 3.3: The plot shows the transmission spectrum for a 250-μm diameter cavity, with peak height ~ 7.5 μm. The broad peak near 1522 nm is due to a transmission resonance outside the buckled areas. The inset plot shows the fundamental resonance line in greater detail. Mode-field images were captured with the laser tuned near one of the resonance lines, as indicated. Images for the four nominally degenerate modes associated with the third-order resonance were captured by making fine adjustments to the laser wavelength.

resonance frequency. We speculated that this was caused mainly by thermal expansion [21] related to residual absorption in the mirrors. This instability was reduced significantly by addition of the a-Si capping layer, as described in Section 3.2. To minimize error in estimating experimental line-widths, scans were performed at low laser power. Also, measurements were repeated at various scan rates, and for both decreasing and increasing laser wavelength. Experimental Q and F were estimated from the FWHM line-width of the fundamental resonance. The predicted FSR takes mirror penetration into account [22], and was confirmed using a white-light source and spectrum analyzer setup (not shown). As listed in Table 1, the experimental finesse for each cavity was in good agreement with the reflectance limited prediction ($F_R \sim 3140$).

Representative results for a 250-μm diameter dome are shown in Figure 3.3.

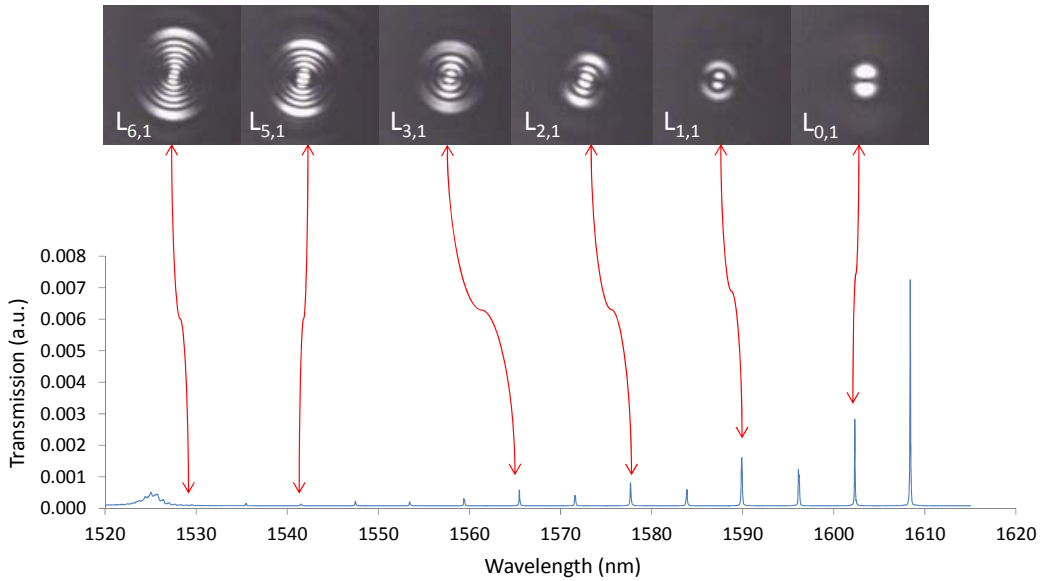

Figure 3.4: The plot shows the transmission spectrum for a 200-μm diameter dome, with peak height ~ 5.7 μm. Representative $L_{p,1}$ mode images are shown; they were captured by tuning the laser source to one of the resonance lines as indicated.

Transverse modes exhibited fixed spacing with values in good agreement with the predictions from paraxial theory, as summarized in Table 1. As mentioned, associated with each higher-order resonance line is a set of nominally degenerate HG and LG modes, whose degeneracy is perturbed by any deviation from cylindrical/spherical symmetry, such as spherical aberration or astigmatism [10, 19]. Such perturbations are apparent from the multiple sub-peaks within the $g = 2$ and $g = 3$ resonant lines in Figure 3.3. By making fine adjustments (typically on the order of a few picometers) to the laser wavelength, it was possible to visually isolate individual HG and LG modes within a given resonant line. As an example, the $H_{3,0}$, $H_{2,1}$, $L_{0.3}$, and $L_{1,1}$ modes shown represent the complete set of HG and LG modes possessing $g = 3$ degeneracy. To our knowledge, such direct experimental evidence for the intrinsic relationship between LG and HG modes is rarely reported. We believe it is made possible, in part, by the near-cylindrical symmetry and geometrical perfection of the self-assembled microcavities.

For the smallest cavities, the LG modes were dominant and it was in fact more

difficult to isolate HG modes. Moreover, there was less evidence for the existence of multiple peaks within the high-order resonance lines, suggesting a higher degree of symmetry. As an example, Figure 3.4 shows the transmission spectrum for a 200-μm diameter cavity. Also shown are representative images of $L_{p,1}$ modes, which were found to be dominant in this case. As predicted by Equation 3.3, this family of modes occupies the odd-order ($g = 1, 2, 5, ...$) resonance lines. The mismatch between the incident beam and the fundamental cavity mode is particularly large here, resulting in significant coupling to higher order modes. As above, these modes exhibit a fixed spacing in good agreement with paraxial theory. Finally, the effective fundamental mode volume is on the order of $V_m \sim 100\lambda^3$ for the smallest cavities, comparable to values reported for similar cavities [10, 11].

3.4 Summary and Conclusions

The reflectance-limited optical properties of the cavity modes can be taken as evidence that the 'defect finesse' [1] of the cavities is high. This suggests that cavities formed by buckling can have very low roughness and a highly regular geometric shape. In principle, the finesse could be improved by using higher reflectance mirrors. For example, reflectance of the present mirrors is mainly limited by absorption in the a-Si layers, which could be reduced by the use of hydrogenated a-Si. Furthermore, operation at shorter wavelengths might be possible by replacing a-Si with TiO_2 or another similar material, provided compressively stressed layers are possible.

The shape of the cavities, and especially the minimum radius of curvature and thus cavity modal volume, will ultimately be limited by the restricted combination of film thicknesses, cavity size, and stress that produces dome-shaped buckles. A full exploration of these details is left for future work. Nevertheless, the Q, F, and V_m demonstrated are already competitive with values reported in the literature

[10, 11, 12]. Another major issue, particularly for sensing and atomic physics studies, is the possibility of implementing 'open-access' versions of the dome cavities. A possible solution might involve intersecting air channels, which we have demonstrated previously using the buckling process [13].

References

[1] E. J. Eklund, A.M. Shkel, "Factors affecting the performance of micromachined sensors based on Fabry-Perot interferometry," *J. Micromech. Microeng.*, vol. 15, pp. 1770-1776, 2005.

[2] W. Liu, J.J. Talghader, "Thermally invariant dielectric coatings for micromirrors," *Appl. Opt.*, vol. 41, pp. 3285- 3293, 2002.

[3] R. R. A. Syms, "Principles of free-space optical microelectromechanical systems," in *Part C: Journal of Mechanical Engineering Science, Vol. 222 of Proceedings of the Institution of Mechanical Engineers*. Sage Publications, pp. 1-17, 2008.

[4] P. Tayebati, P. Wang, M. Azimi, L. Maflah, D. Vakhshoori, "Microelectromechanical tunable filter with stable half symmetric cavity," *Electron. Lett.*, vol. 34, pp. 1967-1968, 1998.

[5] H. Halbritter, M. Aziz, F. Riemenschneider, P. Meissner, "Electrothermally tunable two-chip optical filter with very low-cost and simple concept," *Electron. Lett.*, vol. 38, pp. 1201-1202, 2002.

[6] R. Crocombe, "MEMS technology moves process spectroscopy into a new dimension," *Spectroscopy Europe*, June–July, pp. 16–19, 2004.

[7] Y. Colombe, T. Steinmetz, G. Dubois, F. Linke, D. Hunger, J. Reichel, "Strong atom-field coupling for Bose-Einstein condensates in an optical cavity on a chip," *Nature*, vol. 450, pp. 272-276, 2007.

[8] I. Favero, K. Karrai, "Optomechanics of deformable optical cavities," *Nature Photonics*, vol. 3, pp. 201-205, 2009.

[9] C. Toninelli, Y. Delley, T. Stoferle, A. Renn, S. Gotzinger, V. Sandoghdar, "A scanning microcavity for in situ control of single-molecule emission," *Appl. Phys. Lett.*, vol. 97, 021107, 2010.

[10] P. R. Dolan, G.M. Hughes, F. Grazioso, B.R. Patton, J.M. Smith, "Femtoliter tunable optical cavity arrays," *Opt. Lett.*, vol. 35, pp. 3556-3558, 2010.

[11] A. Muller, E.B. Flagg, J.R. Lawall, G.S. Solomon, "Ultrahigh-finesse, low-mode-volume Fabry-Perot microcavity," *Opt. Lett.*, vol. 35, pp. 2293-2295, 2010.

[12] M. Trupke, E.A. Hinds, S. Eriksson, E. A. Curtis, Z. Moktadir, E. Kukharenka, M. Kraft, "Microfabricated high-finesse optical cavity with open access and small volume," *Appl. Phys. Lett.*, vol. 87, 211106, 2005.

[13] E. Epp, N. Ponnampalam, W. Newman, B. Drobot, J.N. McMullin, A.F. Meldrum, R.G. DeCorby, "Hollow Bragg waveguides fabricated by controlled buckling of Si/SiO_2 multilayers," *Opt. Express*, vol. 18, pp. 24917-24925, 2010.

[14] S. Bruynooghe, N. Schmidt, M. Sundermann, H. W. Becker, S. Spinzig, "Optical and structural properties of amorphous silicon coatings deposited by magnetron sputtering," in *Optical Interference Coatings, OSA Technical Digest, Optical Society of America*, 2010, paper ThA9.

[15] J.W. Hutchinson, M.D. Thouless, E.G. Liniger, "Growth and configurational stability of circular, buckling-driven film delaminations," *Acta Metall. Mater.*, vol. 40, pp. 295-308, 1992.

[16] L. Freund, S. Suresh, *Thin Film Materials, Stress, Defect Formation, and Surface Evolution*. Chap. 5, Cambridge University Press, 2003.

[17] A. Yariv, P. Yeh, *Photonics: Optical Electronics in Modern Communications, 6th ed*. Chap. 4, Oxford University Press, 2007.

[18] A. E. Siegman, *Lasers*. University Science Books, 1986.

[19] R. C. Pennington, G. D'Alessandro, J. J. Baumberg, and M. Kaczmarek, "Tracking spatial modes in nearly hemispherical microcavities," *Opt. Lett.*, vol. 32, pp. 3131-3133, 2007.

[20] Kimel, L.R. Elias, "Relations between Hermite and Laguerre Gaussian modes," *IEEE J. Quant. Electron.*, vol. 29, pp. 2562-2567, 1993.

[21] E. Epp, N. Ponnampalam, J. N. McMullin, and R. G. DeCorby, "Thermal tuning of hollow waveguides fabricated by controlled thin-film buckling," *Opt. Express*, vol. 17, pp. 17369-17375, 2009.

[22] E. Garmire, "Theory of Quarter-Wave-Stack Dielectric Mirrors Used in a Thin Fabry-Perot Filter," *Appl. Opt.*, vol. 42, pp. 5442-5449, 2003.

4 Assessing the maximum transmittance of periodic metal-dielectric multilayers[2]

4.1 Introduction and Background

When resonant tunneling conditions are satisfied [1], metal-dielectric (MD) multilayers containing many skin depths of metal can exhibit bands of high transparency [2, 3, 4]. For problems involving propagating waves inside the dielectric layers, the MD stack can be viewed as a series of coupled Fabry-Perot cavities. Structures of that type have been studied for use as transparent conductors [3] and nonlinear media [5]. More recently, the propagation of evanescent waves through MD stacks has been explored for metamaterial and superlensing applications [6]. The mechanism for evanescent wave transfer is the excitation of coupled surface plasmon resonances at the metal-dielectric boundaries [7, 8].

For both propagating [3] and evanescent [9] waves, it has been recognized that higher transmittance (for a given total thickness of metal) is possible when the metal is sub-divided into a series of thin films. This fact has long been known by optical engineers [2], however, owing to the potential transmittance (PT) theory of Berning and Turner [10]. PT theory shows that low transmittance through a thin metal film is most often due mainly to an impedance mismatch between the film and the external media, rather than absorption by the metal. A given metal film has a maximum PT, by adding appropriate impedance-matching assemblies to the entrance and exit surfaces of the film. For example, a narrowband impedance match is the basis of the induced transmission (IT) filter [10]. In our view, the work of Berning and Turner remains somewhat under-appreciated. For example, a recently proposed strategy [11] for maximizing transparency of a single metal layer is essentially identical to

[2]This chapter was published as a paper in the *Journal of the Optical Society of America B*, vol. 28, pp. 2529-2536, 2011.

the half-century-old IT filter concept (for which a detailed description is provided in the text book by MacLeod [12]).

PT theory was derived from considerations of Poynting power flow [10], and thus provides a general framework for assessing the transparency of MD stacks. On that basis, the primary contributions of the present study can be summarized as follows:

1. We show that the maximum transmittance predicted by PT theory is a useful upper limit for assessing the transparency of MD stacks, such as those recently studied as transparent metals [3].

2. For propagating waves in a stack comprising DMD unit cells, we show that PT theory combined with the theory of equivalent layers [13, 14, 15] can aid in the understanding of the impedance matching role of the dielectric spacer layers. This approach illustrates that thinner metal films can be impedance matched (to an external air medium) by lower index spacer layers.

3. We generalize the PT results for arbitrary (effective) angles of propagation, and confirm that the maximum PT of an absorbing assembly always represents an upper limit for the intensity transmittance of tunneling waves, regardless of the type of resonance (Fabry-Perot or surface-plasmon) associated with the tunneling.

4.2 Maximum potential transmittance of metal (Ag) films

As mentioned, the opacity of thin metal films is often attributable to an impedance mismatch with the external media [16]. For example, Bloemer *et al.* [3] showed that MD stacks can have a band of high transparency (in the visible region for example) while exhibiting high opacity for all other frequencies. The opacity derives mainly from the impedance mismatch between the incident medium and the multilayer,

while absorption by the metal plays a much smaller role. In the same sense, high transmittance can be interpreted as a band-limited impedance matching condition, determined by the particular index and thickness of the dielectric layers separating adjacent metal layers.

Impedance matching to maximize power flow through absorbing layers is precisely the problem addressed by PT theory [2, 10, 12, 13, 14, 15]. PT of an absorbing layer (or assembly of absorbing layers) is the ratio of the transmitted intensity to the intensity entering the front surface:

$$\mathrm{PT} = \frac{T}{1-R} = \frac{T}{T+A} \tag{4.1}$$

where T, R, and A are the transmittance, reflectance, and absorbance of the layer or assembly of layers. For $R = 0$ (i.e. with a perfect antireflection coating on the incident side), the transmittance is equal to the potential transmittance. While T depends on the properties of both the incident and exit media, PT is determined solely by the properties of the absorbing assembly and the exit medium. For a given absorptive layer, PT has a limiting value ($\mathrm{PT_{MAX}}$), which is attained by appropriate choice of the exit medium admittance and can be calculated from the properties of the layer [2, 10, 12, 13, 14]. Typically, the PT concept has been applied to the design of filters for normally incident plane waves. However, the underlying equations can be generalized to allow for arbitrary values of the in-plane wave vector as follows [15]:

$$\mathrm{PT_{MAX}} = \sigma - \left(\sigma^2 - 1\right)^{1/2}, \tag{4.2}$$

where:

$$\sigma = \frac{\cosh\left(2\mu_i\right) + \Gamma^2 \cos\left(2\mu_r\right)}{\left(1+\Gamma^2\right)}. \tag{4.3}$$

Γ is unique for TE- and TM-polarized waves, and is given by:

$$\begin{aligned} \Gamma_{\mathrm{TE}} &= \mathrm{Im}\left(N_M b\right)/\mathrm{Re}\left(N_M b\right) \\ \Gamma_{\mathrm{TM}} &= \mathrm{Im}\left(N_M/b\right)/\mathrm{Re}\left(N_M b\right) \end{aligned}, \tag{4.4}$$

where $b = \cos(\theta_M)$, θ_M is the complex angle of propagation in the absorptive (metal) layer and $N_M = n_M - i\kappa_M$ is its complex refractive index. Finally, the complex phase thickness of the absorptive layer (with thickness d_M) is defined as follows:

$$\mu_c = \mu_r + i\mu_i = \left(\frac{2\pi}{\lambda}\right) N_M d_M \cos(\theta_M). \tag{4.5}$$

A very useful property, in the present context, is that for a layered sequence of N absorbing assemblies having individual potential transmittances PT_1, PT_2, ...PT_N, the overall potential transmittance is the product of that for each assembly [15]; i.e. $\mathrm{PT}_{total} = \mathrm{PT}_1 \cdot \mathrm{PT}_2 \cdot \ldots \cdot \mathrm{PT}_N$, and it follows that $\mathrm{PT}_{\mathrm{MAX}} = \mathrm{PT}_{1,\mathrm{MAX}} \cdot \mathrm{PT}_{2,\mathrm{MAX}} \cdot \ldots \cdot \mathrm{PT}_{N,\mathrm{MAX}}$. The maximum potential transmittance of a multilayer can thus be predicted from the properties of its constituent absorptive layers. The actual transmittance of the multilayer depends on the media (index, thickness, and order of layers) in which these absorptive layers are embedded. Finally, it can be shown [15] that the maximum transparency condition (i.e. $T = \mathrm{PT}_{\mathrm{MAX}}$) occurs when the system containing absorbing layers is perfectly AR-coated for both left and right incidence (i.e. when the system is optimally impedance matched to both the incident and emergent media).

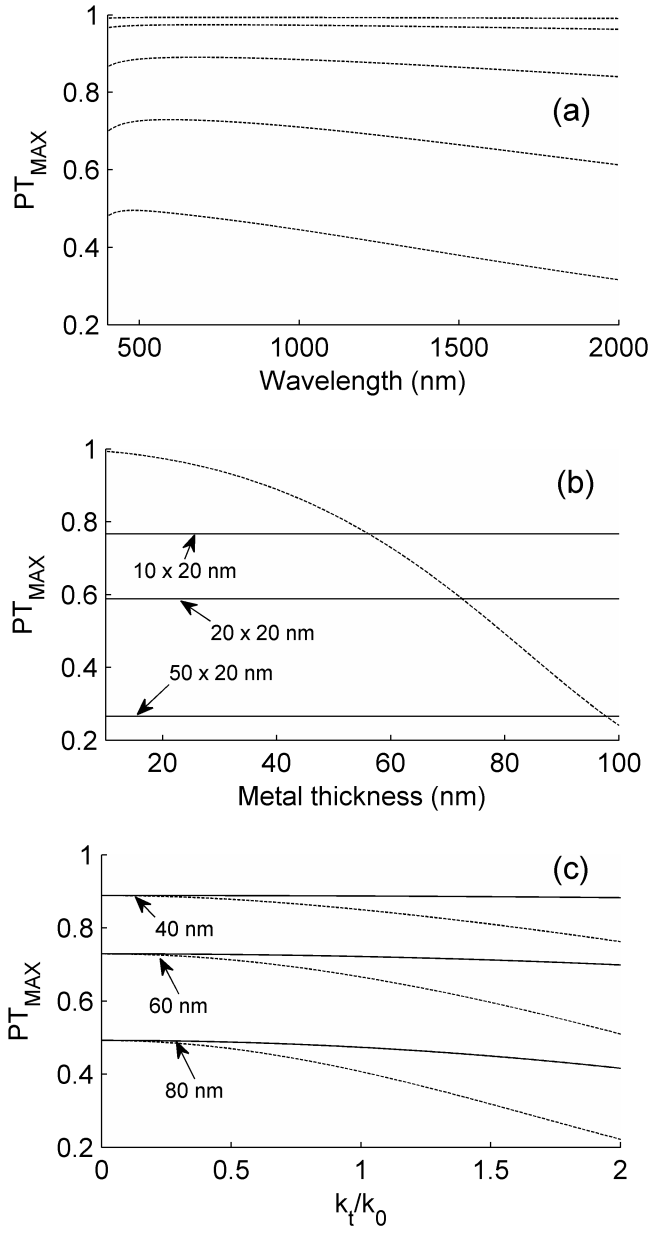

Figure 4.1: (a) Normal-incidence PT_{MAX} of a silver film versus wavelength, for film thicknesses of 10, 20, 40, 60 and 80 nm (top to bottom). (b) The dotted line shows the normal-incidence PT_{MAX} versus film thickness, for a silver film at 550-nm wavelength. The solid lines indicate the maximum potential transmittance for a multilayer containing 10, 20, and 50 Ag films, where each Ag film is 20 nm thick. (c) PT_{MAX} versus transverse component of the wave propagation vector (transverse spatial frequency), for 3 different thicknesses (as indicated by the labels) of an Ag film at 550-nm wavelength. The solid curves correspond to TE polarization and the dotted curves correspond to TM polarization.

Figure 4.1(a) shows the normal-incidence PT_{MAX} versus wavelength for a single Ag film of varying thickness. Except where indicated otherwise, the optical constants of Ag were modeled using the Lorentz-Drude expressions provided by Rakic et al. [17]. In keeping with the discussion above and below, very thin metal films can exhibit significant transparency in the visible-near IR region, where the metal refractive index is dominated by its imaginary part.

Figure 4.1(b) plots the normal-incidence PT_{MAX} versus Ag film thickness at 550-nm wavelength, where the Rakic model predicts Ag refractive index $N_M = 0.1342 - 3.1688i$. PT_{MAX} increases rapidly with decreasing film thickness, allowing a sequence of very thin films to have much higher transparency than a single relatively thick film. For 20-nm thickness, as an example, the plot predicts $PT_{1,MAX} = 0.975$. For a multilayer containing N Ag films, each 20 nm thick, and no other absorbing layers, it follows from above that $PT_{MAX} = (0.975)^N$, as indicated by the horizontal lines in Figure 4.1(b) for the cases $N = 10$, 20, and 50. A multilayer with 50 such films (total Ag thickness ~ 1 μm) has the same potential for transparency as a single film ~ 100 nm thick. In general, for a given total thickness of Ag (d_{TOT}), PT_{MAX} increases as the metal is subdivided into a larger number of distinct films with smaller thickness (d_{TOT}/N) [2]. Clearly, this property is one of the bases for the multilayer transparent metal concept [3].

In Figure 4.1(c), PT_{MAX} at 550-nm wavelength is plotted versus the normalized transverse component of the wave vector. Note that for a dielectric index n_D, evanescent wave behavior (in that dielectric) corresponds to the range $k_t > n_D k_0$, where k_0 is the free-space wave number. For TE-polarized waves, PT_{MAX} is relatively insensitive to the effective angle of incidence in the metal layer. However, for TM-polarized waves, PT_{MAX} drops off quite rapidly with increasing transverse component of the wave vector. Since it is TM-polarized surface plasmons that mediate the tunneling of evanescent waves [9], we can

expect that the maximum intensity transmittance of such waves will decrease monotonically with increasing (transverse) spatial frequency, as discussed further in Section 4.4.

4.3 Impedance matching of DMD structures for propagating waves

The use of impedance matching layers to enhance the transmission of single metal films is an established technique in various fields, including work on heat-reflecting windows [18] and surface-emitting LEDs [19]. For example, it is known from empirical studies [18] that the transparency of a noble metal film can be greatly enhanced if the film is sandwiched by high-index dielectric layers of appropriate thickness. In the context of periodic metal-dielectric stacks [3], high-index spacer layers have been shown to provide enhanced peak transmittance, a wider transparency band, and improved omnidirectionality [6, 20, 21]. As above, these insights have been derived mainly from empirical and numerical studies. In the present section, our goal is to provide new insights into the impedance matching role played by the dielectric spacer layers. We consider a finite stack embedded in air, with a fundamental dielectric-metal-dielectric (DMD) unit cell (see Figure 4.2), and for simplicity we assume normal incidence. Note that this type of stack is equivalent to the 'AR-coated transparent metal' described by Bloemer *et al*. [3, 6] and others [21], where the terminating dielectric layers are half the thickness of the spacer layers. At a given frequency, symmetric unit cells of this type can be replaced by a single equivalent layer [13, 14, 15]. A key motivation for the unit cell approach is as follows: if conditions for optimal impedance matching ($R_1 = 0$) of the unit cell are established, then any sequential stack of N unit cells is also optimally impedance matched ($R_N = 0$) [15].

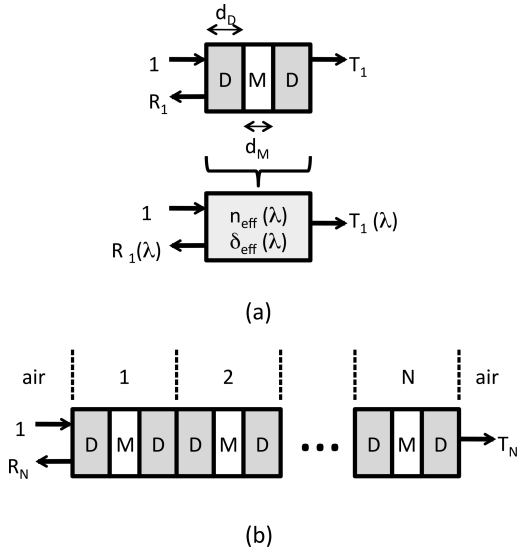

Figure 4.2: (a) Schematic diagram of a DMD unit cell in air with normal incidence light. The symmetric DMD cell can be replaced by a single layer with frequency-dependent effective index and phase thickness. (b) Schematic diagram of a 1-dimensional metal-dielectric multilayer constructed from a sequence of N unit cells.

At a given wavelength, the symmetric DMD cell can be replaced by a single equivalent layer with an effective phase thickness (δ_{eff}) and an effective index (n_{eff}) (see Figure 4.2(a)). General expressions for these parameters (in terms of the layer thicknesses and indices) are available, but do not readily lend themselves to analytical insight [13]. Simplification is possible if a purely imaginary metal index is assumed (i.e. an ideal metal assumption), in which case the effective index can be expressed [14]:

$$n_{eff} = n_D \left\{ \frac{\sin 2\delta \cosh \mu - \frac{1}{2}(\kappa_M/n_D - n_D/\kappa_M)\cos 2\delta \sinh \mu - \frac{1}{2}(\kappa_M/n_D + n_D/\kappa_M)\sinh \mu}{\sin 2\delta \cosh \mu - \frac{1}{2}(\kappa_M/n_D - n_D/\kappa_M)\cos 2\delta \sinh \mu + \frac{1}{2}(\kappa_M/n_D + n_D/\kappa_M)\sinh \mu} \right\}^{1/2}, \quad (4.6)$$

where n_D is the real dielectric index, $N_M = -i \cdot \kappa_M$ is the purely imaginary metal index, $\delta = (2\pi n_D d_D)/\lambda_o$ is the phase thickness of the dielectric layers, $\mu = (2\pi \kappa_M d_M)/\lambda_o$ is an effective phase thickness for the metal layer, d_D is the dielectric layer thickness, d_M is the metal layer thickness, and λ_o is the free-space

wavelength. The approximation is reasonable for metals with high potential transmittance, for which the refractive index is necessarily dominated by its imaginary part [10].

It is interesting to consider the conditions for unity transmittance through the idealized DMD unit cell in air. Considering the equivalent layer from Figure 4.2(a), $T_1 = 1$ can occur under two scenarios: (i) the effective index is real and the effective phase thickness is an integer multiple of π ($\delta_{eff} = m\pi$, where $m = 0, 1, 2...$) or (ii) the effective index is equal to 1. The first scenario corresponds to the Fabry-Perot resonance condition for a lossless layer embedded in air [22]. However, numerical studies reveal that δ_{eff} is an integer multiple of π only in regions where n_{eff} is complex [13]. The second scenario represents a perfect impedance match between the DMD cell and the air medium. For a given dielectric index, this condition can be satisfied by appropriate choice of d_D, provided the metal thickness is below some maximum value (see Figure 4.3). Further insight into this interesting behavior is possible by setting $n_D = \kappa_M$, in which case Equation 4.6 reduces to:

$$n_{eff} = \kappa_M \left\{ \frac{\sin 2\delta \cosh \mu - \sinh \mu}{\sin 2\delta \cosh \mu + \sinh \mu} \right\}^{1/2}. \tag{4.7}$$

Since μ is positive by definition, the maximum real value for n_{eff} occurs when the dielectric layers are tuned such that $\sin 2\delta = +1$:

$$n_{eff,\mathrm{MAX}} = \kappa_M e^{-\mu}. \tag{4.8}$$

For $T_1 = 1$, the maximum allowable metal thickness follows by setting $n_{eff,\mathrm{MAX}} = 1$:

$$d_{M,\mathrm{MAX}} = \left(\frac{\lambda_o}{2\pi\kappa_M} \right) \ln(\kappa_M); \quad [\text{for} \, n_D = \kappa_M]. \tag{4.9}$$

For example, using $\lambda_0 = 638.3$ nm and $\kappa_M = 5$, Equation 4.9 predicts $d_{M,\mathrm{MAX}} =$

32.7 nm, in agreement with the numerical result shown in Figure 2 of reference [16]. While restricted to a special case, Equation 4.9 nevertheless provides insight with respect to the numerical results below, and to our knowledge it has not been derived previously.

To explore the effect of varying the dielectric index, we used a standard transfer matrix technique. The transmittance is a periodic function of d_D, and the maximum transmittance was extracted from plots of the type shown in Figure 4.4(a) below. Figure 4.3(a) shows typical plots of the maximum transmittance versus ideal metal thickness, with n_D as a parameter. In keeping with the analysis above, a perfect impedance match in air ($n_{eff} = 1$) is possible up to a maximum value in each case, beyond which a higher dielectric index is required. Although not obvious from the plot, the transfer matrix result for the case $n_D = \kappa_M = 3.1688$ reveals perfect agreement ($d_{M,\mathrm{MAX}} = 31.86$ nm) with Equation 4.9.

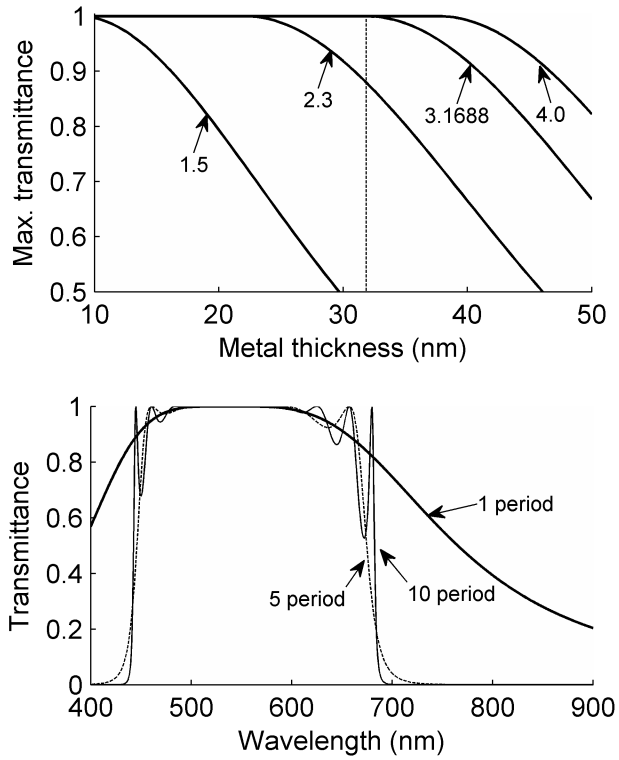

Figure 4.3: (a) Maximum transmittance versus ideal metal layer thickness is plotted for a DMD unit cell in air, at a wavelength of 550 nm. A metal refractive index $N_M = -3.1688i$ was assumed, approximating Ag at 550 nm. The labels indicate the real refractive index (n_D) assumed for the dielectric layers. The vertical dotted line indicates the analytical result predicted by Eq. (9) for the case $n_D = \kappa_M = 3.1688$. (b) Transmittance is plotted for N (1, 5, and 10 as indicated by the labels) period multilayers under an ideal metal assumption, with $n_D = 3.1688$, $d_D = 21.7$ nm, $d_M = 31.86$ nm.

As mentioned, an optimally matched unit cell automatically leads to an optimally matched multilayer constructed from N unit cells. Stated another way, if the unit cell is characterized by equivalent parameters δ_{eff} and n_{eff}, then a symmetric multilayer containing N unit cells can itself be replaced by a single equivalent layer with effective phase thickness $N \cdot \delta_{eff}$ and the same effective index [13]. Thus, the condition $n_{eff} = 1$ for the unit cell extends to the multilayer constructed from that unit cell. This is numerically verified in Figure 4.3(b), for the particular case $n_D = \kappa_M$ (550 nm) = 3.1688 and $d_M = d_{M,\mathrm{MAX}} = 31.86$ nm;

$d_D = 21.7$ nm is the thinnest dielectric layer thickness that produces $n_{eff} = 1$ in this case. A non-dispersive dielectric index and dispersive metal extinction coefficient (from the Rakic model) were used. Unity transmittance at 550 nm is predicted for any number of periods N. Of course, the periodic multilayer is a photonic bandgap structure, and the transmittance band in the 450-700-nm range lies between two stop bands.

In the case of real metals, unity transmittance is not possible and the goal is instead to realize $T = \mathrm{PT}_{\mathrm{MAX}}$. From the discussion above and since the structure is assumed symmetric, the PT of the DMD unit cell is maximized when $R_1 = 0$. The statements regarding equivalent layers still hold [13], and for a multilayer constructed of unit cells with $R_1 = 0$ it follows that $R_N = 0$ and $T_N = (\mathrm{PT}_{1,\mathrm{MAX}})^N$. In words, if we can construct a DMD unit cell that is optimally matched to the ambient medium, then a multilayer constructed from N repeat units of that same cell is also optimally matched to the ambient medium.

Figure 4.4(a) plots the predicted transmittance for 25-nm Ag thickness versus d_D, with n_D as a parameter. In general, the transmittance is a periodic function of the dielectric layer's thickness. The peak transmittance increases with dielectric index, reaching $\mathrm{PT}_{1,\mathrm{MAX}}$ at a particular value, given by $n_D = 4.75$ in this case. For the more realistic, but still high, dielectric index $n_D = 3.5$, peak transmittance is very close to $\mathrm{PT}_{1,\mathrm{MAX}}$. Figure 4.4(b) plots the maximum transmittance versus metal thickness with n_D as a parameter. Similar to the ideal metal case, there is an overall trend that for increasing dielectric index it is possible to impedance match (i.e. to make $T_{1,\mathrm{MAX}}$ close to $\mathrm{PT}_{1,\mathrm{MAX}}$) for increasingly thick metal films.

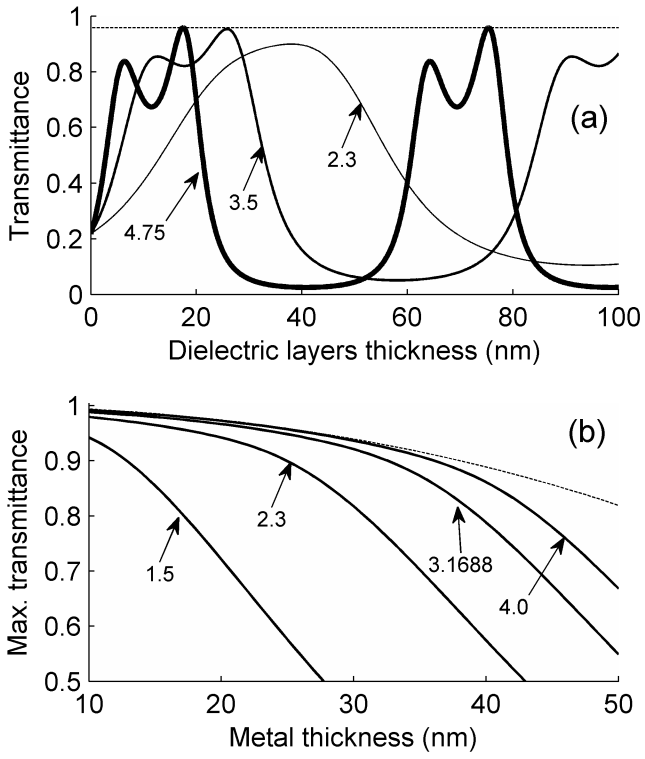

Figure 4.4: (a) Normal-incidence transmittance versus thickness of the dielectric layers (for three different values of the dielectric refractive index as indicated by the labels) is plotted for a DMD unit cell in air at 550-nm wavelength, with metal index $N_M = 0.1342 - 3.1688i$ (representing Ag at 550 nm) and metal thickness 25 nm. The dotted line indicates $\mathrm{PT}_{1,\mathrm{MAX}}$. (b) Maximum transmittance is plotted versus metal thickness at 550-nm wavelength, for various dielectric indices as labeled. The dotted line indicates $\mathrm{PT}_{1,\mathrm{MAX}}$.

Figure 4.5(a) shows the variation in maximum transmittance versus n_D, for several values of metal thickness. Interestingly, for a given wavelength, metal thickness, and metal index, only a specific dielectric index can enable perfect impedance matching of the unit cell. As shown in Figure 4.5(b), the required index does not vary monotonically with metal thickness. For illustration purposes, unrealistically high values of dielectric index were considered. Indeed, for materials with reasonable transparency in the visible range, refractive index is typically less than ~ 3.5 [6]. For thinner metal layers (< 25 nm thick), a nearly optimal impedance match is provided by realistic dielectrics with index in the 2 to

3.5 range. This is consistent with the high transparency reported for metal-dielectric multilayers comprising thin ($\sim$ 20 nm) metal films and high index spacers [3, 6]. Related to this discussion, it has been previously suggested [20, 21] that an optimal impedance match is attained when $n_D = \kappa_M$. However, that conclusion was derived either from considerations of a thin metal film embedded in an infinite dielectric medium [20] or of a dielectric anti-reflection layer on an infinitely thick metal film [21]. Our results suggest that when the finite thickness of both dielectric and metal films is taken into account, the problem is more subtle. Based on our numerical treatment (and that in [16]), the dielectric index required to produce an optimal impedance match varies with the thickness of the metal film.

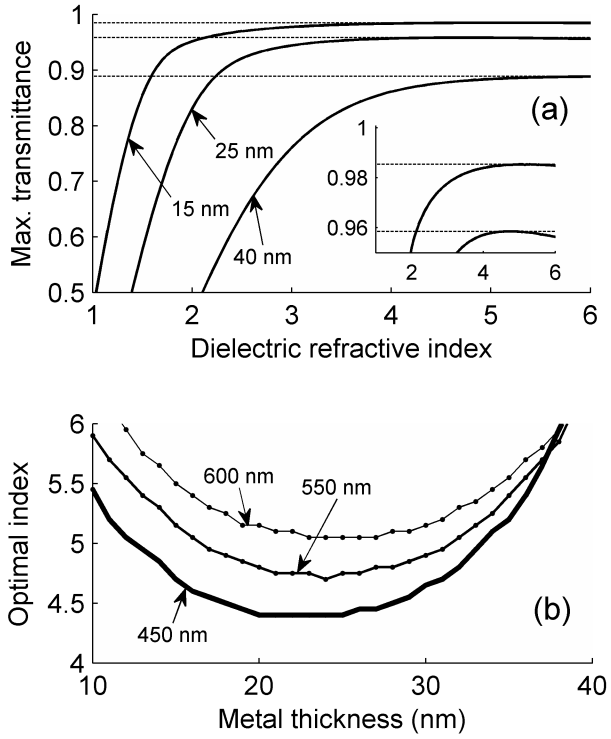

Figure 4.5: (a) Maximum transmittance at 550-nm wavelength for a DMD unit cell is plotted versus the refractive index of the dielectric layers, for Ag layer thicknesses of 15, 25, and 40 nm. The dotted lines indicate $PT_{1,MAX}$. The inset shows the top of the curves for 15 and 25 nm thick Ag layers. (b) The refractive index that enables optimal impedance matching of an Ag film in a DMD structure is plotted versus the Ag film thickness, for 3 different wavelengths.

However, to our knowledge, a complete physical explanation for this behavior has not been provided. Equation 4.9 provides some analytical insight, but only for a particular case. Analytical treatments for the general case would be an interesting topic for future study.

Figure 4.6 shows transmittance plots for periodic multilayers with 5, 10, and 20 unit cells, each cell containing a 25-nm thick Ag film, and for two different dielectric spacer layers. In the first case, a fictitious dielectric with $n_D = 4.75$ and $d_D = 17.5$ nm was assumed, since this represents the optimal impedance matching condition for a 25-nm thick Ag film at 550 nm (see Figure 4.5). As per the discussion above, a multilayer constructed from any number of such unit cells is also optimally impedance matched, so that the transmittance at 550 nm is identical to $(\mathrm{PT}_{1,\mathrm{MAX}})^N$ for any value of N. In the second case, $n_D = 2.3$ was assumed, representative of TiO_2. Furthermore, $d_D = 45.5$ nm was used in order to produce a peak transmittance near 550 nm. Note that this is different than the optimal thickness for a single unit cell of the same type (~ 38 nm, see Figure 4.4). The peak transmittance T_{MAX} is in each case significantly greater than $(T_{1,\mathrm{MAX}})^N \sim (0.9)^N$, and the ratio $T_{\mathrm{MAX}}/(T_{1,\mathrm{MAX}})^N$ actually grows with increasing N. This represents an impedance matching advantage arising from field redistribution inside the periodic medium, and was interpreted as anomalous loss scaling by Blair [23]. Of course, in all cases the peak transmittance lies below the maximum potential transmittance curve. PT theory thus provides useful insight into the transparency (relative to optimized transparency) of a given MD stack, and offers a valuable framework for evaluating transparent metals [3].

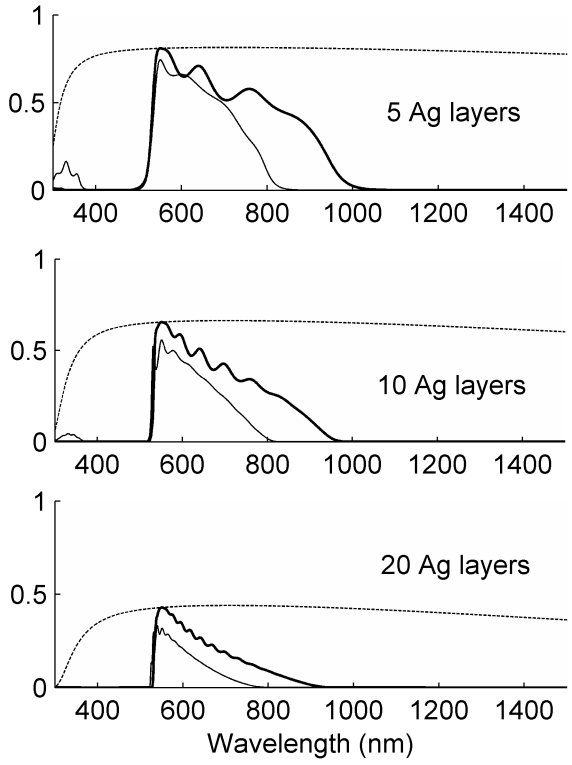

Figure 4.6: Spectrally dependent, normal-incidence transmittance of metal-dielectric multilayers is plotted for $N = 5$, 10, and 20. 25 nm thick Ag layers and a non-dispersive dielectric with $n_D = 4.75$ (thick solid line) or $n_D = 2.3$ (thin solid line) were assumed. The unit cell dielectric thickness was set to $d_D = 17.5$ nm and $d_D = 45.5$ nm for the higher and lower index cases, respectively. The dotted curves indicate $\mathrm{PT}_{\mathrm{MAX}}$ of a multilayer containing N Ag layers (each 25 nm thick).

4.4 Impedance matching of DMD structures in the evanescent wave regime

As discussed in Section 4.2, PT theory can be generalized for non-normal incidence. Moreover, since it is based on the flow of photon flux, the theory applies even when Snell's law predicts complex angles (i.e. evanescent behavior) inside the lossless layers of a stack. While tunneling of evanescent fields (mediated by TM-polarized surface plasmon resonances) [7, 8] is the basis for practical implementation of the superlens [6, 9], the optimization of power flow in that

context is still the subject of ongoing research [24] and careful interpretation of the transmittance is necessary. For example, when framed in terms of a near-field (evanescent) input, a transmission coefficient much greater than 1 can be predicted [6, 9]. This reflects the fact that the evanescent field is coupled to a guided mode resonance of the layered structure, via which it is effectively transferred to the output side. Energy associated with the input evanescent wave is not transmitted into the output far-field (unless a curved geometry [25] or diffraction grating [26] is added to facilitate such a coupling), but rather is dissipated by absorption in the metal layers [27]. On the other hand, the interpretation of transmittance is straightforward if the evanescent waves are coupled (via prisms in practice) to propagating waves in the input and output medium [7, 8, 28]. Below, we illustrate that PT theory provides a useful framework for assessing these types of problems. To parallel the treatment in Section 4.3, we again consider a general N-period stack with symmetric DMD unit cells, but here bounded by high-index input and output media (see Figure 4.7) to facilitate the coupling of fields that are evanescent within the dielectric layers.

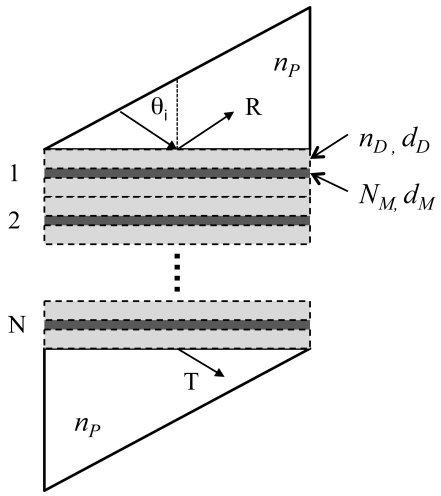

Figure 4.7: The schematic diagram illustrates prism-based coupling of evanescent waves through an N-period metal-dielectric stack with symmetric DMD unit cells. The prisms have refractive index $n_P > n_D$.

Surface-plasmon mediated tunneling through a single-period DMD structure was first studied by Dragila et al. [7]. They provided closed-form expressions for reflectance and transmittance, and also provided an approximate expression for the angle of incidence (inside the prism) that produces peak transmittance (θ_{MAX}). The expressions are quite involved and are not repeated here; however, a key conclusion was that the maximum transmittance occurs when $R = 0$. Given the general nature of PT theory, this can be placed in context with the discussion in Section 4.2. Specifically, $R \sim 0$ is the hallmark of a nearly perfect impedance match, in which case we should expect $T \sim \mathrm{PT}_{\mathrm{MAX}}$. Furthermore, a multilayer constructed from N repeat units of an impedance-matched unit cell will also be impedance matched to the external media, and will thus exhibit $T \sim (\mathrm{PT}_{1,\mathrm{MAX}})^N$. In the following, we use transfer matrix theory to verify these relationships. Note that a variable incident angle introduces an additional free parameter, so that impedance matching is not solely dependent on the refractive index of the dielectric spacer layers [16]. For non-normal incidence, the energy flow normal to the boundaries of the films can be analyzed by assigning a so-called 'tilted optical admittance' [12] to each medium. For TM polarization, this effective admittance for medium i is given by $n_i/(Z_0 \cos\theta)$, where n_i is the refractive index, Z_0 is the impedance of free space, and θ is the angle (predicted by Snell's law) inside the medium. In a sense, for non-normal incidence the medium has an effective refractive index, which is $n_i/\cos\theta$ for TM polarization.

We first consider the geometry described in [7], with a 60-nm Ag film symmetrically bounded by MgF_2 layers ($n_D = 1.38$) and coupled by glass prisms ($n_P = 1.515$). To facilitate direct comparison, we assumed the same wavelength and Ag index as used in [7]. As shown in Figure 4.8, the transfer matrix calculation reproduces their results for the case of 300-nm MgF_2 layers. As mentioned, however, their expression for θ_{MAX} contains an approximation. From a

numerical optimization, an improved impedance match (i.e. R closer to zero) is possible using 220-nm thick MgF_2 layers, and occurs at a slightly higher incident angle. Also plotted in Figure 4.8 is the maximum potential transmittance, as predicted by the expressions from Section 4.2. As expected from the discussion above, the transmittance curve is perfectly bounded by the PT_{MAX} curve, with $T \sim PT_{MAX}$ occurring at the incident angle ($\sim$ 80 degrees) that produces nearly optimal impedance matching.

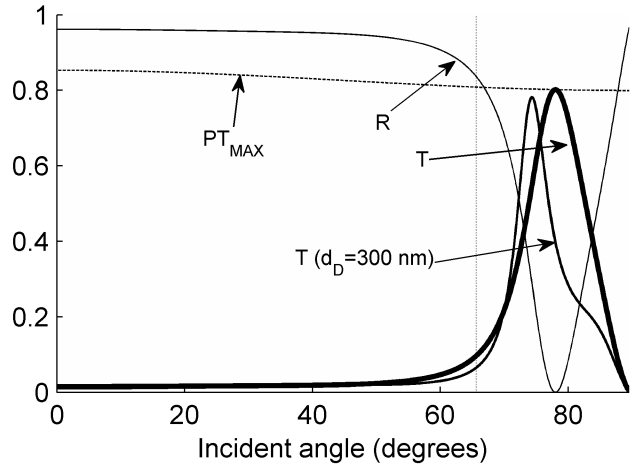

Figure 4.8: Theoretical reflectance (thin solid line), transmittance (thick solid line), and PT_{MAX} (dotted line) for a 1-period DMD structure with $n_D = 1.38$, $d_D = 220$ nm, $N_M = 0.066 - 4.0i$, and $d_M = 60$ nm. The wavelength is 632.8 nm, and data is plotted versus incident angle inside a prism medium with $n_P = 1.515$. The vertical dotted line indicates the critical angle for total internal reflection between the prism and the dielectric medium. The thin solid line shows the transmittance for $d_D = 300$ nm, to facilitate direct comparison with [7].

To illustrate that impedance-matched unit cells can be cascaded to form impedance-matched MD stacks, we first consider a similar geometry as used in Figure 4.8, but with a thinner Ag layer ($d_M = 25$ nm). Also, we reverted to using the Ag optical constants from the Rakic model so that spectral plots could be generated. Given these assumptions, a nearly optimal impedance match at 632.8-nm wavelength is obtained for $d_D = 230$ nm and at an incident angle of

~ 67.1 degrees (i.e. $k_t \sim 1.4k_0$). Figure 4.9(a) plots the transmittance and PT_{MAX} for MD stacks comprising 1, 5, 10, and 20 unit cells of this type, versus the transverse component of the wave vector. Note that $k_t > 1.38k_0$ corresponds to evanescent behavior in the MgF_2 layers. Thus, the nearly optimal impedance match at $k_t \sim 1.4k_0$ corresponds to tunneling mediated by a surface plasmon resonance. The transmission band at lower incident angles ($0.5k_0 < k_t < k_0$) is due to Fabry-Perot mediated tunneling of propagating waves. While the reflectance curves are not shown in the interest of clarity, the nearly optimal impedance match ($R \sim 0$) is retained for an arbitrary number of unit cells and, as expected from the discussion above, $T \sim (PT_{1,MAX})^N$ at the resonant angle. Note that mode splitting related to the multiplicity of metal-dielectric interfaces is clearly observed in the angular domain.

In Figure 4.9(b), the predicted spectral dependences are plotted for conditions of resonant tunneling ($k_t \sim 1.4k_0$). Interestingly, relatively featureless (i.e. flat) and broad transparency bands are observed. The existence of such 'transparent bands' has been described previously by Feng et al. [28], although their theoretical analysis was restricted to the case of ideal lossless metal layers (in which case 100% transmission is predicted regardless of N). The transparent band arises only in symmetric structures, and corresponds to excitation of field profiles that match the Bloch modes of an equivalent structure with infinite extent. The present results confirm analogous behavior in the case of a real metal. However, the transmittance is necessarily within the limits predicted by PT theory, and thus reduces with increasing number of periods N.

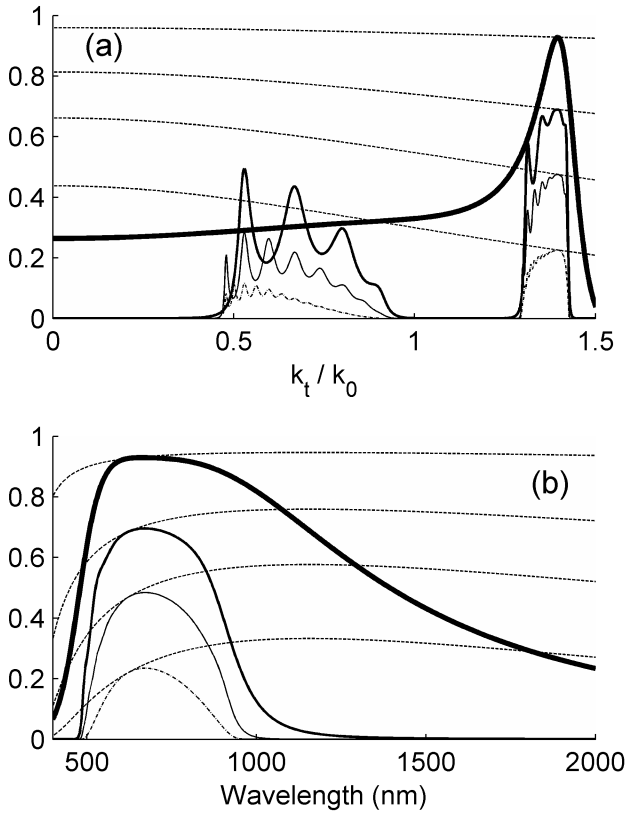

Figure 4.9: (a) Transmittance (solid and dash-dot curves), and PT_{MAX} (dotted curves) predicted for 1-, 5-, 10-, and 20-period DMD stacks (note: T_{MAX} and PT_{MAX} reduce with increasing number of periods), versus the normalized transverse wave vector component. Dielectric indices and wavelength are the same as in 4.8, but here $d_D = 230$ nm, $N_M = 0.1436 - 3.8045i$ (from the Rakic model) and $d_M = 25$ nm. (b) Transmittance and maximum potential transmittance for the structures in part (a) versus wavelength, and for the incidence angle (i.e. $k_t = 1.4k_0$) that produces an impedance match at 632.8-nm wavelength.

As a final illustration, we consider a structure more closely aligned with those studied in [28], and more typical of the MD stacks studied for superlens applications. Figure 4.10(a) shows results analogous to those in Figure 4.9(a), but with $n_D = 1.631$, $n_P = 4$, $d_D = d_M = 50$ nm, and at 500-nm wavelength. Simulations were repeated for different values of n_P, but the reflectance and transmittance curves exhibit little dependence on that parameter. In agreement with Figure 7 of [28], a transmission peak is observed at $(k_t/k_0) \sim 2.18$. However,

the peak transmittance falls off rapidly (compared to Figure 4.9) with increasing number of periods, for two reasons. First, $\mathrm{PT_{MAX}}$ is considerably lower for 50-nm Ag films compared to 25-nm Ag films. Second, $\mathrm{PT_{MAX}}$ for TM-polarized waves drops off considerably with increasing k_t/k_0, as discussed in Section 4.2. As above, the transmittance in all cases is perfectly bounded by PT theory results, with $T \sim (\mathrm{PT_{1,MAX}})^N$ under impedance-matched conditions.

Figure 4.10(b) shows the spectral dependence for the structure described in Figure 4.10(a), for $(k_t/k_0) = 2.18$, illustrating the existence of the transparent band. As above, the transmittance is perfectly bounded by the $\mathrm{PT_{MAX}}$ curves and the peak transmittance drops off accordingly with increasing number of periods. We stress that the results shown in Figures 4.8, 4.9 and 4.10 are intended to be illustrative. The statements regarding the PT theory are generally applicable to problems of this type, not restricted to the particular structures shown.

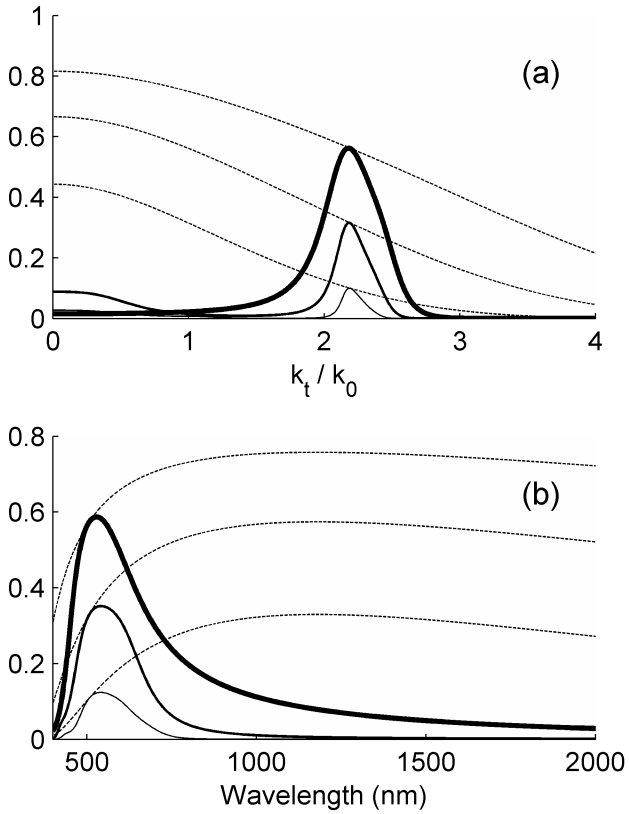

Figure 4.10: (a) As in 4.9(a), except for 1, 2, and 4 periods of a DMD stack with $d_D = d_M = 50$ nm, $n_D = 1.631$, and at a wavelength of 500 nm where $N_M = 0.1436 - 3.8045i$ (from the Rakic model) (b) As in 4.9(b), but for the parameters in part (a) and for the incident angle (i.e. $k_t = 2.18k_0$) that produces an impedance match in this case.

4.5 Summary and Conclusions

We reviewed the main results from PT theory, and demonstrated its general utility for analyzing power flow through MD stacks. For a given stack, PT theory provides the maximum potential transmittance ($\mathrm{PT_{MAX}}$), which represents a useful reference for assessing the transmittance of any tunneling-based transparency band.

For propagating waves inside the dielectric layers, our results help to clarify the impedance matching conditions for MD stacks embedded in air. Confirming a previous result in the literature [16], we showed that for ideal metal films

sandwiched by dielectric layers, unity transmittance is predicted up to a maximum metal thickness that scales with the dielectric index. While the impedance matching conditions are more complicated for real metal films, there is an analogous trend that thicker metal films require higher index dielectrics in order to be well-matched to an air medium.

For evanescent waves inside the dielectric layers, we confirmed that the intensity transmittance is bounded (as for propagating waves) by the predictions of the PT theory. The numerical study was restricted to a prism-coupled system modeled using standard transfer-matrix techniques. However, we expect that the PT theory will always correctly predict the maximum power transmittance, even if the evanescent waves are coupled by diffraction gratings or other means. This is possibly an interesting topic for further studies.

References

[1] P.W. Baumeister, "Optical tunneling and its applications to optical filters," *Appl. Opt.*, vol. 6, pp. 897-906, 1967.

[2] P.W. Baumeister, "Radiant power flow and absorptance in thin films," *Appl. Opt.*, vol. 8, pp. 423-436, 1969.

[3] M.J. Bloemer, M. Scalora, "Transmissive properties of Ag/MgF_2 photonic band gaps," *Appl. Phys. Lett.*, vol. 72, pp. 1676-1678, 1998.

[4] C.-S. Kee, K. Kim, H. Lim, "Optical resonant transmission in metal-dielectric multilayers," *J. Opt. A: Pure Appl. Opt.*, vol. 6, pp. 267-269, 1999.

[5] R.S. Bennink, Y.-K. Yoon, R.W. Boyd, J.E. Sipe, "Accessing the optical nonlinearity of metals with metal-dielectric photonic bandgap structures," *Opt. Lett.*, vol. 24, pp. 1416-1418, 1999.

[6] M. Bloemer, G. D'Aguanno, N. Mattiucci, M. Scalora, N. Akozbek, "Broadband super-resolving lens with high transparency in the visible range," *Appl. Phys. Lett.*, vol. 90, 174113, 2007.

[7] R. Dragila, B. Luther-Davies, S. Vukovic, "High transparency of classically opaque metallic films," *Phys. Rev. Lett.*, vol. 55, pp. 1117-1120, 1985.

[8] S. Hayashi, H. Kurokawa, H. Oga, "Observation of resonant photon tunneling in photonic double barrier structures," *Optical Review*, vol. 6, pp. 204-210, 1999.

[9] S. Anantha Ramakrishna, J.B. Pendry, M.C.K. Wiltshire, W.J. Stewart, "Imaging the near field," *J. Mod. Opt.*, vol. 50, pp. 1419-1430, 2003.

[10] P.H. Berning, A.F. Turner, "Induced transmission in absorbing films applied to band pass filter design," *J. Opt. Soc. Am.*, vol. 47, pp. 230-239, 1957.

[11] G.-Q. Du, H.-T. Jiang, L. Wang, Z.-S. Wang, H. Chen, "Enhanced transmittance and fields of a thick metal sandwiched between two dielectric photonic crystals," *J. Appl. Phys.*, vol. 108, 103111, 2010.

[12] H.A. Macleod, *Thin-Film Optical Filters, Third Edition*. Institute of Physics Publishing, 2001.

[13] B.V. Landau, P.H. Lissberger, "Theory of induced-transmission filters in terms of the concept of equivalent layers," *J. Opt. Soc. Am.*, vol. 62, pp. 1258-1264, 1972.

[14] H.A. Macleod, "A new approach to the design of metal-dielectric thin-film optical coatings," *Optica Acta*, vol. 25, pp. 93-106, 1978.

[15] P.H. Lissberger, "Coatings with induced transmission," *Appl. Opt.*, vol. 20, pp. 95-104, 1981.

[16] I.R. Hooper, T.W. Preist, J.R. Sambles, "Making tunnel barriers (including metals) transparent," *Phys. Rev. Lett.*, vol. 97, 053902, 2006.

[17] A.D. Rakic, A.B. Djurisic, J.M. Elazar, and M.L. Majewski, "Optical properties of metallic films for vertical-cavity optoelectronic devices," *Appl. Opt.*, vol. 37, pp. 5271-5283, 1998.

[18] G. Leftheriotis, P. Yianoulis, D. Patrikios, "Design and optical properties of optimized ZnS/Ag/ZnS thin films for energy saving applications," *Thin Sol. Films*, vol. 306, pp. 92-99, 1997.

[19] H. Cho, C. Yun, S. Yoo, "Multilayer transparent electrode for organic light-emitting diodes: tuning its optical characteristics," *Opt. Express*, vol. 18, pp. 3404-3414, 2010.

[20] D. Owens, C. Fuentes-Hernandez, B. Kippelen, "Optical properties of one-dimensional metal-dielectric photonic band-gap structures with low-index dielectrics," *Thin Sol. Films*, vol. 517, pp. 2736-2741, 2009.

[21] Y.-K. Choi, Y.-K. Ha, J.-E. Kim, H.Y. Park, K. Kim, "Antireflection film in one-dimensional metallo-dielectric photonic crystals," *Opt. Comm.*, vol. 230, pp. 239-243, 2004.

[22] P. Yeh, *Optical Waves in Layered Media*. Wiley, 2005.

[23] S. Blair, "Anomalous loss scaling in periodically absorbing media," *J. Opt. Soc. Am. B*, vol. 18, pp. 1943-1948, 2001.

[24] M. Yoshida, S. Tomita, H. Yanagi, S. Hayashi, "Resonant photon transport through metal-insulator-metal multilayers consisting of Ag and SiO_2," *Phys. Rev. B*, vol. 82, 045410, 2010.

[25] Z. Jacob, L.V. Alekseyev, E. Narimanov, "Optical hyperlens: far-field imaging beyond the diffraction limit," *Opt. Express*, vol. 14, pp. 8247-8256, 2006.

[26] Y. Xiong, Z. Liu, C. Sun, X. Zhang, "Two-dimensional imaging by far-field superlens at visible wavelengths," *Nano Lett.*, vol. 7, pp. 3360-3365, 2007.

[27] N. Mattiucci, G. D'Aguanno, M. Scalora, M.J. Bloemer, C. Sibilia, "Transmission function properties for multi-layered structures: Application to super-resolution," *Opt. Express*, vol. 17, pp. 17517-17528, 2009.

[28] S. Feng, J. Merle Elson, P.L. Overfelt, "Transparent photonic band in metallodielectric nanostructures," *Phys. Rev. B*, vol. 72, 085117, 2005.

5 Conditions for admittance-matched tunneling through symmetric metal-dielectric stacks[3]

5.1 Introduction and background

Tunneling of electromagnetic radiation through metal films has captured the attention of researchers for a variety of reasons. Since the 1970s [1], for example, dielectric-metal-dielectric (DMD) coatings have been studied in the context of solar control and thermal emittance windows [2, 3], and as transparent electrodes for displays [4]. In the late 1990s, Bloemer *et al*. [5] showed that periodic MD multilayers can exhibit wide bands of high transparency, and suggested their application as transparent conductors and radiation shields. Others have explored the analogy between optical tunneling and the quantum mechanical tunneling of electrons over potential barriers [6, 7]. More recently, metal-dielectric stacks have been studied in the context of superlenses [8, 9], since they support plasmon-mediated tunneling of TM-polarized evanescent waves. Energy transport through such structures remains an active topic for study [10, 11, 12].

Symmetric DMD tri-layers have played a central role in the aforementioned research [1, 2, 3, 4, 6, 7], including antireflection-coated MD stacks [5, 11], which are essentially periodic structures with a DMD unit cell. Much of the knowledge about these structures derives from numerical studies which show, for example, that the use of high-index dielectric layers tends to enhance transparency [2, 5, 11]. Theoretical treatments, on the other hand, have typically relied on simplifications such as use of a lossless metal assumption [7, 13]. In our view, it has not been widely recognized that these various bodies of work can be unified within the framework of potential transmittance (PT) theory [14, 15]. For example, PT theory explains [16] the observation that transmittance can be increased by sub-dividing a given

[3]This chapter was published as a paper in *Optics Express*, vol. 20, pp. A578-A588, 2012.

thickness of metal into some number of thinner metal layers, appropriately spaced by dielectrics [5, 8].

The goal of this work is to assess the limits of tunneling-based transparency, given a periodic DMD multilayer containing real, absorbing metal layers. In a previous, transfer-matrix-based numerical study [17], we used PT theory as a general framework for assessing maximum transmittance. Here, we provide an extended theoretical treatment of this approach, and derive a general equation that encapsulates the conditions for admittance-matched tunneling. This approach offers new insight into previously disjointed research on tunneling through MD stacks. Moreover, it directly addresses the important problem of maximizing transmittance (T) and minimizing reflectance (R) in such structures.

5.2 Admittance matching for minimum effective absorptance of a metal film

As first explained by Berning and Turner [14], the transparency of a thin absorbing film is highly dependent on its boundary conditions. In fact, there is a maximum potential transmittance ($\mathrm{PT_{MAX}}$) that, for a sufficiently thin film, is much greater than the maximum transmittance suggested by the bulk optical absorption coefficient. To achieve $\mathrm{PT_{MAX}}$ at a given wavelength (which Berning and Turner termed as 'inducing transmission' [14]), one must design the surrounding media so that the exit optical admittance (viewed from the perspective of the absorbing film) attains a particular value determined by the optical constants and thickness of the film [15]. $T = \mathrm{PT_{MAX}}$ occurs when $R = 0$ for both left and right incidence [17], which illustrates that inducing transmission is essentially equivalent to admittance matching an absorbing film to the ambient media.

Consider a single absorbing film (with index $N_M = n_M - i\kappa_M$) embedded within an arbitrary assembly of otherwise lossless layers, as shown in Figure 5.1(a). The

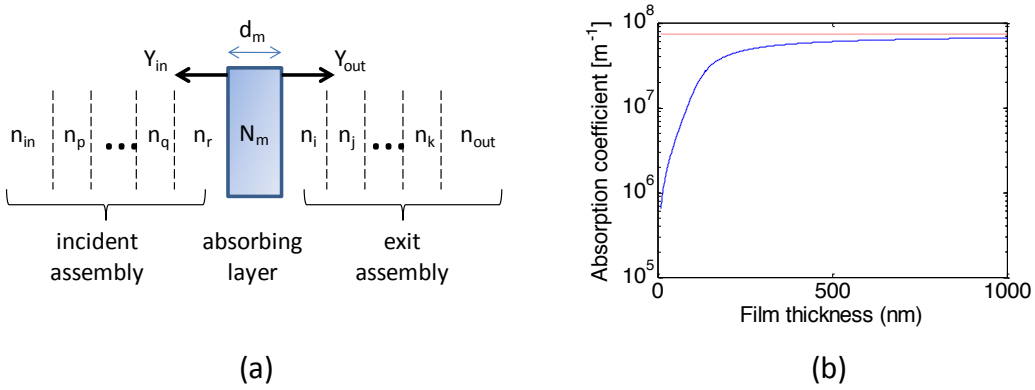

Figure 5.1: (a) Schematic showing a multilayer containing one absorbing layer. The optical admittance viewed from the perspective of the absorbing layer, looking towards the incidence and exit directions, is labeled as Y_{in} and Y_{out} respectively. (b) The optimal (i.e. minimum) optical absorption coefficient, as defined in the text, is plotted versus Ag film thickness at a wavelength of 550 nm and for normal incidence. The bulk absorption coefficient for Ag at the same wavelength is represented by the red dotted line.

potential transmittance ($\mathrm{PT} = T/(1-R)$) of the film depends on the properties (i.e. thickness and index) of the film itself and on the optical admittance presented by the exit assembly ($Y_{out} = H_{out}/E_{out}$), which determines the ratio of the magnetic to electric field at the output interface of the absorbing layer. For a given incident angle and state of polarization, $\mathrm{PT_{MAX}}$ is dependent on the properties of the absorbing film only, and can be calculated using expressions provided previously [17].

While not typically stated in terms of absorption, one implication of PT theory is that the absorptance of a thin film can be significantly lower than the value predicted by the bulk optical constants. This is especially true for very thin films, but the possibility of reduced absorption (with appropriate admittance matching) extends to surprisingly large film thickness. To illustrate, we compared the minimum effective absorption coefficient (α_{min}) for an Ag thin film to the bulk optical absorption coefficient ($\alpha_M = 4\pi\kappa_M/\lambda$) for Ag. Optical constants of Ag were modeled using the Lorentz-Drude expressions provided by Rakic *et al.* [18]. Noting that PT is the ratio of power flux at the entrance and exit interface of the

absorbing film, it follows that $\mathrm{PT_{MAX}} = \exp\left(-\alpha_{min} d_M\right)$, or rearranging:

$$\alpha_{min} = -\ln\left(\mathrm{PT_{MAX}}\right)/d_M. \tag{5.1}$$

As an example, Figure 5.1(b) shows a plot of α_{min} versus Ag film thickness at a wavelength of 550 nm and for normal incidence. Remarkably, for a 10-nm thick Ag film the minimum effective absorption coefficient is 2 orders of magnitude lower than the bulk absorption coefficient. Note that a multilayer containing an arbitrary number of 10-nm thick Ag films can have absorptance embodied by this same α_{min}, provided that the Ag films are separated by appropriate dielectric layers to produce an optimal admittance match. Band-limited admittance matching is the reason for the surprisingly high transparency of MD stacks containing many skin depths of metal [5].

Implicit above, and to PT theory in general, is the assumption that the bulk refractive index $N_M = n_M - i\kappa_M$ remains valid for describing the optical properties of the thin film. As is well known, very thin metal films can exhibit optical properties that deviate from bulk values, such as a higher effective extinction coefficient arising from electron scattering at grain boundaries. Furthermore, quantum confinement effects cannot be neglected for length scales less than ~ 10 nm [19]. Nevertheless, carefully deposited Ag films have been shown [19, 20] to exhibit bulk properties for thickness as low as $\sim 10-12$ nm. Based on this, we restrict our theoretical analysis to films > 10 nm thick, and assume that bulk optical constants can be applied in this range. In practice, deviation from bulk properties is possible depending on the film deposition technique, and should be considered.

As mentioned, to achieve $\mathrm{PT} = \mathrm{PT_{MAX}}$ requires that the exit admittance Y_{out} is set to a specific, optimal value $Y_{op} = X_{op} + iZ_{op}$. In the following, all admittances are expressed in free-space units (i.e. normalized to the admittance of free space). Closed-form expressions for X_{op} and Z_{op} at normal-incidence are provided by

Macleod [15]. Those expressions can be generalized for non-normal incidence as follows:

$$X_{op} = \left(\begin{array}{c} \frac{\left(\eta_R^2 + \eta_I^2\right)\left(\eta_R \sinh\beta\cosh\beta + \eta_I \sin\alpha\cos\alpha\right)}{\left(\eta_R \sinh\beta\cosh\beta - \eta_I \sin\alpha\cos\alpha\right)} \\ -\frac{\eta_R^2\eta_I^2\left(\sin^2\alpha\cosh^2\beta + \cos^2\alpha\sinh^2\beta\right)}{\left(\eta_R \sinh\beta\cosh\beta + \eta_I \sin\alpha\cos\alpha\right)^2} \end{array} \right)^{1/2} . \tag{5.2}$$

$$Z_{op} = \frac{\eta_R\eta_I\left(\sin^2\alpha\cosh^2\beta + \cos^2\alpha\sinh^2\beta\right)}{\left(\eta_R \sinh\beta\cosh\beta - \eta_I \sin\alpha\cos\alpha\right)}$$

Here, η_R and η_I are the real and imaginary parts of the tilted optical admittance [15] of the metal layer, which is unique for TE and TM polarization:

$$\eta_M = \eta_R - i\eta_I = \begin{cases} \left(n_M - i\kappa_M\right)\cdot\cos\theta_M & \text{[TE]} \\ \left(n_M - i\kappa_M\right)/\cos\theta_M & \text{[TM]} \end{cases} \tag{5.3}$$

where θ_M is the complex angle in the metal layer. For consistency with Macleod [15], the effective phase thickness of the metal layer is expressed:

$$\delta_M = \alpha - i\beta = \left(\frac{2\pi}{\lambda}\right)\left(n_M - i\kappa_M\right) d_M \cos\theta_M . \tag{5.4}$$

Note that the last expression differs from the notation and convention ($\mu = \mu_r + i\mu_i$) used for the effective phase thickness of the metal layer in our previous work shown in Chapter 4 [17]. Also note that $\mathrm{PT} = \mathrm{PT_{MAX}}$ occurs when $Y_{out} = Y_{op}$, whereas $T = \mathrm{PT_{MAX}}$ (and $R = 0$) occurs when $Y_{in} = Y_{out} = Y_{op}$. Thus, our goal can be restated as follows: given a periodic DMD multilayer, we seek to identify conditions for attaining $Y_{in} = Y_{out} = Y_{op}$.

Figure 5.2(a) shows a representative plot of X_{op} and Z_{op} versus Ag film thickness, at a wavelength of 550 nm and for normal incidence. For reasons that

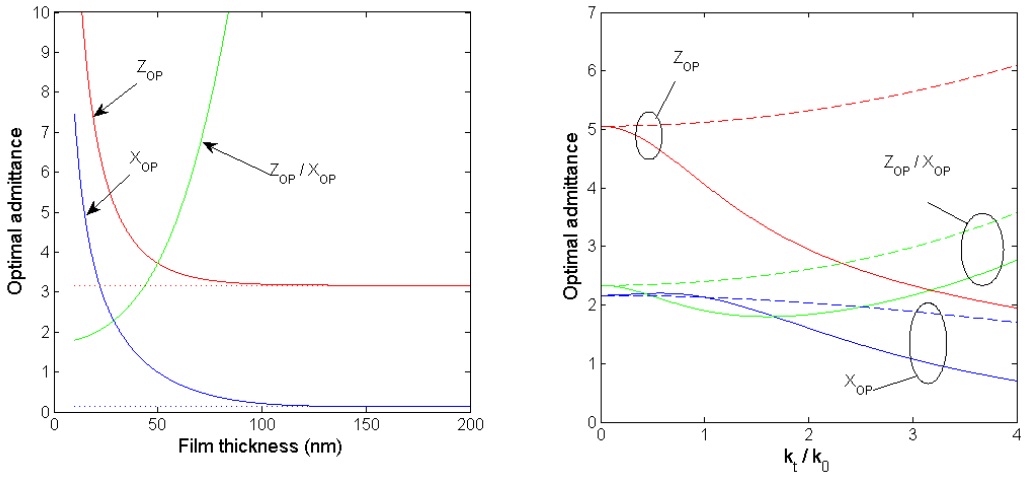

Figure 5.2: (a) Components of the exit admittance (X_{op} and Z_{op}) that produce PT = $\mathrm{PT_{MAX}}$ for normal incidence are plotted versus Ag film thickness, at a wavelength of 550 nm. The green curve shows the ratio Z_{op}/X_{op}. The dashed curves show the real (blue) and imaginary (red) parts of the Ag refractive index at the same wavelength. (b) The same quantities are plotted versus normalized transverse wave vector, for a 30-nm thick Ag film at 550-nm wavelength. The dashed and solid curves correspond to TM and TE polarization, respectively.

will be explained in the following section, the ratio Z_{op}/X_{op} is also plotted. As expected [15], Y_{op} tends toward $N_M^* = n_M + i\kappa_M$ in the limit of a thick metal film (for example, the Rakic model predicts $N_M = 0.1342 - i3.1688$ for Ag at 550-nm wavelength, as indicated by the dashed lines in the figure). Figure 5.2(b) plots the same quantities versus the normalized transverse wave vector, for a 30-nm thick Ag film at the same wavelength and for both TE and TM polarization. For a fixed metal film thickness, the optimal admittance (and the ratio Z_{op}/X_{op}) shows relatively little variation versus the transverse wave vector (i.e. angle).

5.3 Admittance matching conditions for a periodic DMD multilayer

Consider a symmetric DMD unit cell embedded between identical incident and exit media, as shown schematically in Figure 5.3(a). As explained previously [17],

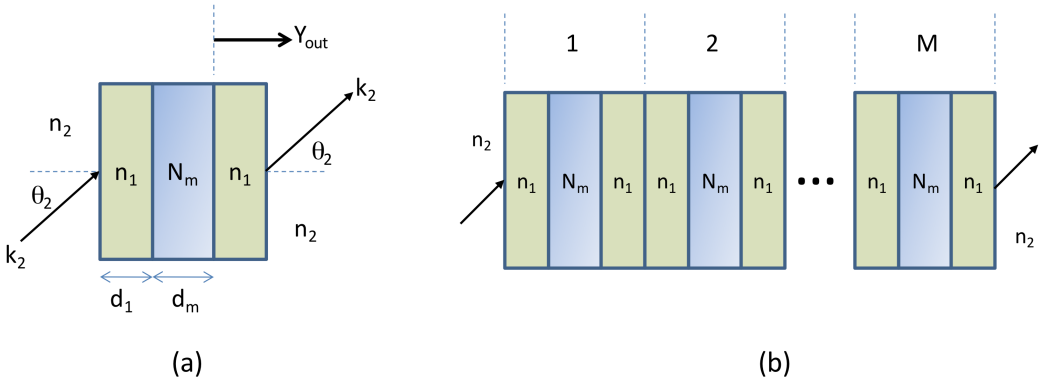

Figure 5.3: (a) Geometry for plane wave incidence on a symmetric DMD unit cell embedded between identical incidence and exit media. The admittance viewed from the perspective of the absorbing metal film (Y_{out}) is that for a thin film (n_1) on a substrate (n_2). (b) Schematic illustration of a periodic MD stack composed of DMD unit cells. Conditions (i.e. n_1, d_1, N_M, d_M, n_2, θ_2) that admittance match the unit cell also result in an admittance-matched multilayer.

conditions (i.e. particular combinations of λ, n_1, d_1, N_M, d_M, n_2, and θ_2) that maximize transmittance (i.e. that produce $T = \mathrm{PT_{MAX}}$) for the unit cell also correspond to conditions for maximum transmittance through the periodic multilayer based on that unit cell.

For the single unit cell, the exit admittance from the perspective of the metal layer is that presented by a single thin film (with real index n_1) on an infinitely thick substrate (with real index n_2) [15]:

$$Y_{out} = \frac{\eta_2 \cos\delta_1 + i\eta_1 \sin\delta_1}{\cos\delta_1 + i(\eta_2/\eta_1)\sin\delta_1}, \tag{5.5}$$

where η_1 and η_2 are the tilted optical admittances of the dielectric layer and the ambient medium, respectively. For TE polarization $\eta_i = n_i \cos\theta_i$ and for TM polarization $\eta_i = n_i/\cos\theta_i$, where n_i and θ_i are the refractive index and the propagation angle (from Snell's law) in medium i. Furthermore, $\delta_1 = (2\pi/\lambda)\, n_1 d_1 \cos\theta_1$ is the phase thickness of the dielectric film. Equating the real and imaginary parts of Equation 5.5 to X_{op} and Z_{op}, respectively, and after some algebraic manipulation, the following admittance matching equation results:

$$X_{op} = \frac{2\eta_2}{\pm\cos\left[\sin^{-1}\left\{\frac{2Z_{op}}{X_{op}(\eta_1/\eta_2 - \eta_2/\eta_1)}\right\}\right]\left(1-\frac{\eta_2^2}{\eta_1^2}\right)+\left(1+\frac{\eta_2^2}{\eta_1^2}\right)}. \tag{5.6}$$

The modifier (+/-) on the cosine term arises because the argument of the arcsine can correspond to an angle in one of two possible quadrants. For a given metal layer (i.e. for a given X_{op} and Z_{op}), the equation predicts that admittance matching (when possible) is dependent on the values of η_1 and η_2 only. However, given a solution to Equation 5.6, the required thickness for the dielectric layer n_1 is fixed by the same set of equations as follows:

$$d_{1,M} = \left(\frac{\lambda}{4\pi n_1 \cos\theta_{1,M}}\right)\sin^{-1}\left\{\frac{2Z_{op}}{X_{op}\left(\eta_{1,M}/\eta_{2,M} - \eta_{2,M}/\eta_{1,M}\right)}\right\}, \tag{5.7}$$

where n_1, $\theta_{1,M}$, $\eta_{1,M}$ and $\eta_{2,M}$ are particular values that resulted in a solution to Equation 5.6. Although not explicitly indicated in Equation 5.7, care must be taken to ensure the angle of the arcsine is taken from the same quadrant that produced the solution to Equation 5.6. Also note that Equation 5.7 corresponds specifically to the minimum thickness that enables the admittance match. At normal incidence, for example, any value $d_1 = d_{1,M} + q\,(\lambda_1/2)$, where q is an integer and $\lambda_1 = \lambda/n_1$, will also produce an admittance match [17]. In general, the admittance matching conditions are attained for periodically repeating values of d_1. As illustrated below, equations Equations 5.6 and 5.7 can be applied to a variety of tunneling problems, including tunneling of propagating waves (i.e. real angles in both the dielectric and ambient media) and tunneling of evanescent waves (i.e. with $n_2 > n_1$ and complex angle θ_1).

Note that X_{op} and Z_{op} are real numbers by definition, and that η_2 is a real number for all cases considered below (i.e. lossless ambient media with real incident angle). Thus, in all cases for which η_1 is purely real (i.e. for non-evanescent wave solutions

in dielectric layers n_1), solutions to Equation 5.6 are restricted to the following range:

$$\left(\frac{\eta_1}{\eta_2} - \frac{\eta_2}{\eta_1}\right) \geq \frac{2Z_{op}}{X_{op}}. \tag{5.8}$$

For a given metal layer, Equation 5.8 places a lower limit on the ratio η_1/η_2, below which solutions to Equation 5.6 are not possible. The ratio Z_{op}/X_{op} is typically high (see Figure 5.2), and diverges for increasing Ag film thickness. Thus, an admittance match is typically reliant on high values of η_1/η_2, especially for large metal thickness.

5.3.1 Normal incidence in air

We first consider the simplest but practically important case of normal incidence from an ambient air medium (i.e. $n_2 = 1$). For normal incidence, the admittance of a medium in free-space units is simply equal to its refractive index. From the preceding discussion, solutions to Equation 5.6 are possible provided $(n_1 - 1/n_1) > 2Z_{op}/X_{op}$. Given typical values of X_{op} and Z_{op} for a thin Ag film in the visible range (see Figure 5.2), this implies that high values of dielectric index n_1 (> 4) are necessary to achieve a perfect admittance match. Moreover, with fixed n_2 and for a given metal layer at a given wavelength, only a specific value of n_1 results in a solution to Equation 5.6. This observation was made previously [17], but in that case solely on the basis of a transfer-matrix numerical study. Solutions to Equations 5.6 and 5.7 were obtained as a function of Ag film thickness using a commercial software tool (Matlab), and representative data is shown in Figures 5.4(a) and 5.4(b).

The results in Figure 5.4(a) provide a theoretical underpinning for, and are in exact agreement with, the transfer-matrix results seen in Figure 4.5(b), other than some numerical noise in the earlier results. Clearly, an impractically large

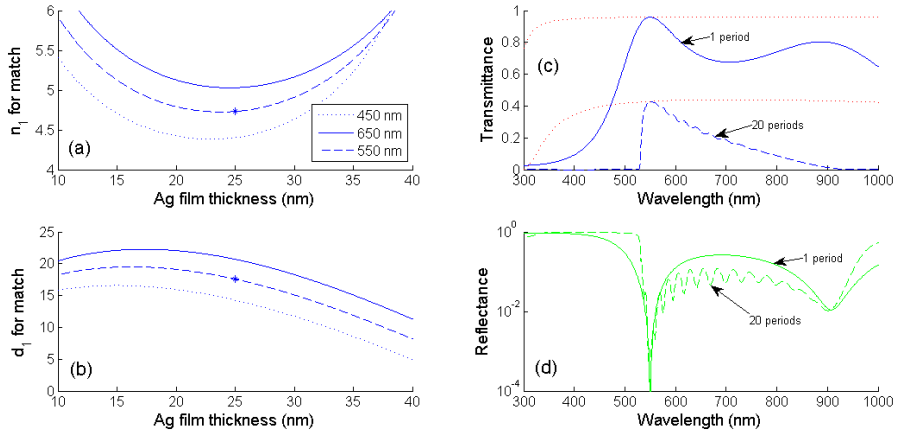

Figure 5.4: (a) The dielectric index required for admittance-matched tunneling of normally incident waves through a periodic DMD stack (with Ag metal layers and air ambient) is plotted for three different wavelengths. The symbol indicates the data point used in subsequent examples. (b) The minimum dielectric layers thickness that results in admittance-matched tunneling when combined with the dielectric indices in part (a). (c) Predicted transmittance for a 1-period (blue solid line) and 20-period (blue dashed line) DMD multilayer with $d_M = 25$ nm, $n_1 = 4.732$ and $d_1 = 17.5$ nm (as indicated by the symbols in parts (a) and (b)). The red dashed lines indicate $\mathrm{PT}_{\mathrm{MAX}}$ for each case. (d) Predicted reflectance for the structures in part (c). Note that the reflectance diverges at 550 nm, indicating a perfect admittance match for any number of periods.

dielectric index is required to facilitate a perfect admittance match for the Ag film at normal incidence. Nevertheless, it is illustrative to consider the implications of the solutions to Equations 5.6 and 5.7. As an example, Figures 5.4(c) and (d) show the predicted T, $\mathrm{PT}_{\mathrm{MAX}}$, and R for a specific admittance-matched case ($\lambda = 550$ nm, and assuming a unit cell with $d_M = 25$ nm, $n_1 = 4.732$ and $d_1 = 17.5$ nm) indicated by the symbols in Figures 5.4(a) and (b). T and R were calculated using a transfer matrix technique, and $\mathrm{PT}_{\mathrm{MAX}}$ was calculated using previously described expressions [17]. As expected, a perfect admittance match (i.e. $T = \mathrm{PT}_{\mathrm{MAX}}$ and $R = 0$) is verified at $\lambda = 550$ nm. This perfect admittance match holds, in principle, for a DMD multilayer comprising an arbitrary number of such unit cells. To illustrate this, data for both 1- and 20-period cases are shown.

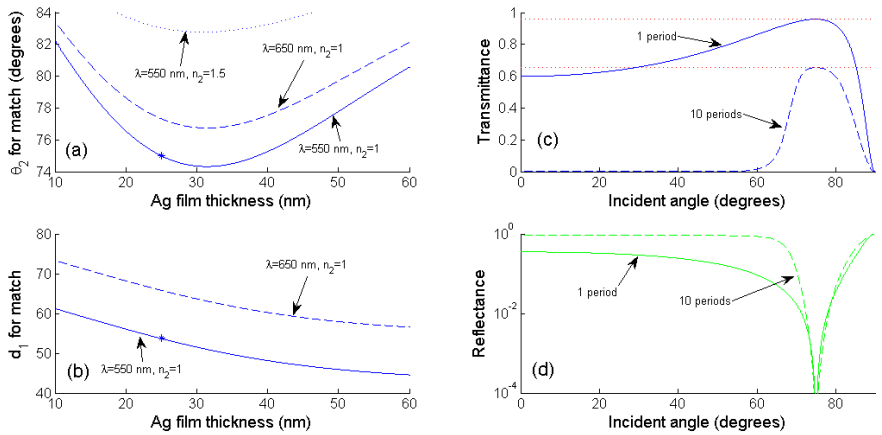

Figure 5.5: (a) Incident angle that results in admittance-matched tunneling of TE waves is plotted versus Ag film thickness, for $n_1 = 2.3$ and $n_2 = 1$, and at two different wavelengths. The dotted curve plots the tunneling angle for $\lambda = 550$ nm, $n_1 = 2.3$, and $n_2 = 1.5$. The symbol indicates the data point used in subsequent examples. (b) The minimum dielectric layers thickness that results in admittance-matched tunneling when combined with the indices and tunneling angles from part (a). (c) Predicted transmittance versus incident angle for a 1-period (blue solid line) and 10-period (blue dashed line) DMD multilayer with $n_1 = 2.3$, $n_2 = 1$, $\lambda = 550$ nm, $d_M = 25$ nm, and $d_1 = 53.7$ nm (as indicated by the symbols in parts (a) and (b)). The red dashed lines indicate $\mathrm{PT}_{\mathrm{MAX}}$ for each case. (d) Predicted reflectance for the structures in part (c). Note that the reflectance diverges at 75.01 degrees, indicating a perfect admittance match.

5.3.2 Admittance-matched tunneling of TE-polarized propagating waves

Given the difficulty of achieving a perfect match at normal incidence, it is interesting to consider tunneling at off-normal incidence. We first consider structures with $n_1 > n_2$, such as the air-ambient case in the previous section. From above, admittance matching requires a sufficiently high value of the ratio η_1/η_2. Interestingly, for a given n_2 and $n_1 > n_2$, this ratio increases with increasing incident angle (θ_2) for TE polarization, but decreases with increasing incident angle for TM polarization. This implies that when $n_1 > n_2$, solutions to Equation 5.6 are possible for off-normal incidence of TE-polarized light only. Tunneling of this kind was described by Hooper et al. [7], but not in the context of the PT theory formalism employed here.

As an example, solutions to Equations 5.6 and 5.7 were obtained for fixed indices $n_1 = 2.3$ and $n_2 = 1$, with results at two different wavelengths plotted in Figures 5.5(a) and (b). For a given wavelength and Ag film thickness, admittance-matched tunneling of TE-polarized light is predicted at a specific incident angle. To further illustrate, a specific data point from these solutions ($\lambda = 550$ nm, $d_M = 25$ nm, $d_1 = 53.71$ nm) was used to generate plots of T and R versus incident angle, shown in Figures 5.5(c) and (d). As expected, admittance-matched tunneling occurs at the incident angle of 75.01 degrees indicated by the symbol in Figure 5.5(a). As for the normal-incidence case, this admittance match extends to a multilayer with arbitrary number of unit cells. The 1- and 10-period cases are shown as examples.

To our knowledge, this efficient tunneling of off-normal TE-polarized waves through multi-period DMD stacks has not been studied previously. It might have implications for the realization of polarizing and angularly selective filters. However, it should be noted that the perfect admittance match is dependent on the symmetry of the structures considered, including the assumption of identical input and exit media. The air-ambient case considered would certainly present practical challenges. Solutions exist for higher values of n_2; example data is shown for $n_2 = 1.5$ in Figure 5.5(a). This could represent a DMD stack symmetrically embedded between glass plates, for example. Note, however, that the solutions lie at even higher incident angles in this case. For propagating waves in an external air medium to access these tunneling angles, coupling prisms [7] or equivalent momentum matching interfaces are required.

5.3.3 Admittance-matched tunneling of TM-polarized evanescent waves

Plasmon-mediated tunneling through symmetric, single-period DMD stacks was originally reported by Dragila *et al.* [21] and later by Hayashi *et al.* [6].

Analogous tunneling through multi-period DMD stacks was studied experimentally by Tomita *et al.* [22] and theoretically by Feng *et al.* [13], who proposed optical filters and modulators based on the concept. Relevant to the present discussion, the low transmittance reported in [22] can be attributed in part to non-optimal admittance matching in their structures.

Consider the structure in Figure 5.3 for cases when $n_2 > n_1$, which might represent a periodic DMD multilayer coupled at its entrance and exit faces by high index prisms. This geometry allows plane waves in the ambient media to couple with evanescent waves in the dielectric layers, thereby enabling a straightforward analysis of the Poynting power flow associated with surface-plasmon-mediated tunneling [13, 17]. Excitation of evanescent waves occurs for $\theta_2 > \theta_C = \sin^{-1}(n_1/n_2)$, where θ_C is the critical angle for total internal reflection. Assuming n_1 and n_2 represent lossless dielectrics, it follows that η_1 and $\sin\delta_1$ are both purely imaginary under these conditions. In that case, the admittance expressed by Equation 5.5 has the same general form as for the propagating wave case, which means that Equations 5.6 and 5.7 retain their validity. However, with $n_2 > n_1$, the ratio η_1/η_2 is expected to increase for TM waves and decrease for TE waves as the incident angle is increased. Thus, opposite to the situation described in the previous section, solutions to Equation 5.6 are expected for TM-polarized waves only.

The existence and the nature of the solutions to Equation 5.6 were found to depend on the stack parameters (λ, d_M, n_1, n_2). However, typically two solutions were found in the evanescent range for a given Ag film thickness and wavelength, as shown by the representative data in Figures 5.6(a) and (b). Note that the transverse wave vector is defined by $k_t = (2\pi/\lambda)\, n_2 \sin\theta_2$, and that waves in the n_1 layers are evanescent when $(k_t/k_0) > n_1$. We assumed $n_1 = 1.631$ and a fictitious coupling medium with $n_2 = 4$, to enable comparison with similar structures studied by Feng

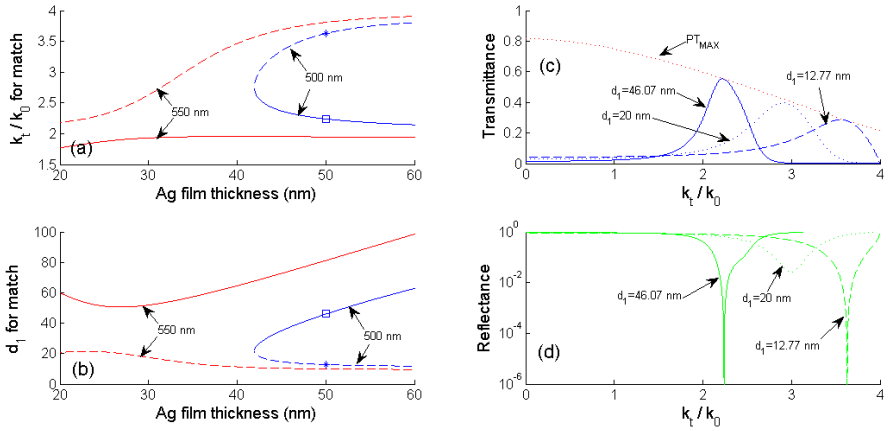

Figure 5.6: (a) Normalized transverse wave vectors that result in admittance-matched tunneling of TM waves is plotted versus Ag film thickness, for $n_1 = 1.631$, $n_2 = 4$, and two different wavelengths ($\lambda = 500$ nm and $\lambda = 550$ nm). The symbols indicate data points used in subsequent examples. (b) The minimum dielectric layers thicknesses that result in admittance-matched tunneling when combined with the indices and tunneling angles from part (a). (c) Predicted transmittance for a 1-period DMD multilayer for $\lambda = 500$ nm, $d_M = 50$ nm, $n_1 = 1.631$, $n_2 = 4$, and various d_1 as indicated by the labels. Note that d_1 values corresponding to the data points indicated by the symbols in part (b) result in admittance-matched tunneling at the transverse wave vector values indicated by the corresponding symbols in part (a). The red dashed line indicates $\mathrm{PT_{MAX}}$. (d) Predicted reflectance for the structures in part (c). Note that the reflectance diverges for the two cases that produce a perfect admittance match.

et al. [13]. For some combinations of λ and d_M (such as for $\lambda = 550$ nm and $d_M <\sim 42$ nm in Figure 5.6(a)), no solutions are found.

The implications of the solutions to Equations 5.6 and 5.7 are analogous to those for the propagating wave cases above. As an example, T and R were plotted in Figures 5.6(c) and (d) for a particular admittance-matched case ($\lambda = 500$ nm, $d_M = 50$ nm. Consistent with the solutions in Figures 5.6(a) and (b), dielectric thicknesses $d_1 = 12.77$ nm and 46.07 nm result in a perfect admittance match ($T = \mathrm{PT_{MAX}}$ and $R = 0$) at normalized wave vector values of 2.18 and 3.61, respectively. Other values of d_1 result in a partial tunneling peak at a different angle, but without a perfect admittance match. The data for $d_1 = 20$ nm is shown as an example.

From an experimental perspective, coupling prisms with $n_2 = 4$ are not practical.

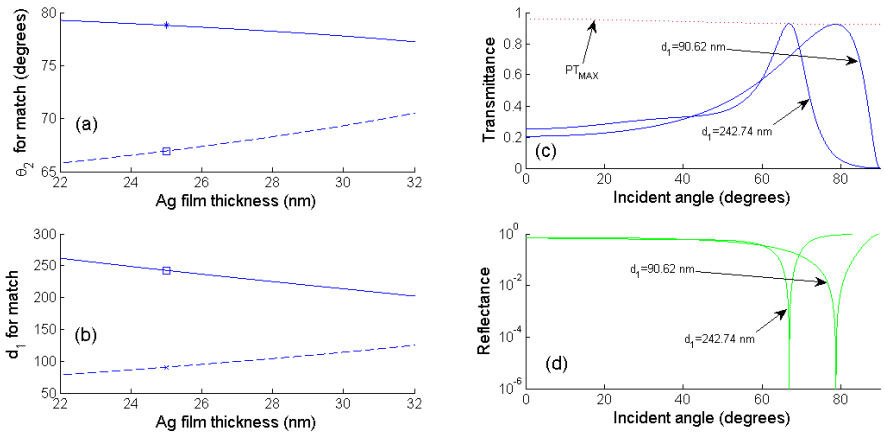

Figure 5.7: As in Figure 5.6, except with $n_2 = 1.515$, $n_1 = 1.38$, and for a 632.8-nm wavelength. (a) Incident angle in external medium (θ_2) that produces a perfect admittance match. (b) Dielectric layers thickness that produces admittance-matched tunneling when combined with the incidence angles from part (a). (c) Transmittance versus incidence angle for a 1-period DMD structure, with $\lambda = 632.8$ nm, $d_M = 25$ nm, and d_1 set to the values indicated by the symbols in part (b), verifying a tunneling peak at the corresponding angles from part (a). (d) Reflectance versus incidence angle for the same conditions as in part (c).

Figure 5.7 shows results for a more practical combination of indices, $n_1 = 1.38$ and $n_2 = 1.515$, representing the MgF_2-based tunneling structures studied by Dragila *et al.* [21].

As mentioned in the introduction, much of the recent interest in plasmon-mediated tunneling through DMD structures is motivated by their potential to transmit the evanescent fields from an object [8]. In these superlens applications, there is a need to design MD structures offering both high transmittance and low reflectance, ideally for a wide range of transverse wave vectors and over the entire operational wavelength range of the lens. In particular, significant reflectance of energy back towards the object contributes to image distortion [10]. The model system studied above (a symmetric DMD stack, symmetrically embedded in lossless ambient media) is not expected to capture all pertinent details of the superlens. For example, transfer of energy associated with the evanescent fields of an object necessarily involves optical absorption by the

detector (at the image plane) and finite reflection from the lens [12]. Nevertheless, the prism-coupled DMD stack can provide insight regarding the qualitative nature of tunneling through the multilayer superlens [22, 23].

5.4 Summary and conclusions

Using potential transmittance theory, we derived a general equation describing the conditions for admittance-matched tunneling through periodic DMD multilayers. We furthermore verified its applicability to tunneling problems involving both propagating and evanescent waves. For normal incidence, the equation predicts that a perfect match occurs only for specific and large values of the dielectric refractive index. For off-normal incidence and assuming fixed dielectric and ambient medium indices, the equation predicts that a perfect admittance match occurs at specific tunneling angles. For TE-polarized light, solutions are found in the propagating wave regime. For TM-polarized light solutions are found in the evanescent-wave regime.

In all cases, matching is predicted to occur at a single wavelength and/or tunneling angle. It seems probable that using two or more dielectrics would enable structures that are matched at more than one wavelength or tunneling angle. The rich body of literature on multilayer anti-reflection coatings and on induced transmission filters might provide substantial guidance in this regard, but such studies are left for future work.

References

[1] C.J. Fan, F.J. Bachner, "Transparent heat mirrors for solar-energy applications," *Appl. Opt.*, vol. 15, pp. 1012-1017, 1976.

[2] G. Leftheriotis, P. Yianoulis, D. Patrikios, "Design and optical properties of optimized ZnS/Ag/ZnS thin films for energy saving applications," *Thin Sol. Films*, vol. 306, pp. 92-99, 1997.

[3] C.G. Granqvist, "Transparent conductors for solar energy and energy efficiency: a broad-brush picture," *Int. J. Nanotechnol.*, vol. 6, pp. 785-797, 2009.

[4] X. Liu, X. Cai, J. Qiao, J. Mao, N. Jiang, "The design of ZnS/Ag/ZnS transparent conductive multilayer films," *Thin Sol. Films*, vol. 441, pp. 200-206, 2003.

[5] M.J. Bloemer, M. Scalora, "Transmissive properties of Ag/MgF_2 photonic band gaps," *Appl. Phys. Lett.*, vol. 72, pp. 1676-1678, 1998.

[6] S. Hayashi, H. Kurokawa, H. Oga, "Observation of resonant photon tunneling in photonic double barrier structures," *Optical Review*, vol. 6, pp. 204-210, 1999.

[7] I.R. Hooper, T.W. Preist, J.R. Sambles, "Making tunnel barriers (including metals) transparent," *Phys. Rev. Lett.*, vol. 97, 053902, 2006.

[8] S. Anantha Ramakrishna, J.B. Pendry, M.C.K. Wiltshire, W.J. Stewart, "Imaging the near field," *J. Mod. Opt.*, vol. 50, pp. 1419-1430, 2003.

[9] Y. Xiong, Z. Liu, C. Sun, X. Zhang, "Two-dimensional imaging by far-field superlens at visible wavelengths," *Nano Lett.*, vol. 7, pp. 3360-3365, 2007.

[10] M. Tsang, D. Psaltis, "Theory of resonantly enhanced near-field imaging," *Opt. Express*, vol. 15, pp. 11959-11970, 2007.

[11] M. Bloemer, G. D'Aguanno, M. Scalora, N. Mattiucci, D. de Ceglia, "Energy considerations for a superlens based on metal/dielectric multilayers," *Opt. Express*, vol. 16, pp. 19342-19353, 2008.

[12] E. Fourkal, I. Velchev, A. Smolyakov, "Energy and information flow in superlensing," *Phys. Rev. A*, vol. 79, 033846, 2009.

[13] S. Feng, J. Merle Elson, P.L. Overfelt, "Optical properties of multilayer metal-dielectric nanofilms with all-evanescent modes," *Opt. Express*, vol. 13, pp. 4113-4124, 2005.

[14] P.H. Berning, A.F. Turner, "Induced transmission in absorbing films applied to band pass filter design," *J. Opt. Soc. Am.*, vol. 47, pp. 230-239, 1957.

[15] H.A. Macleod, *Thin-Film Optical Filters, Third Edition*, Institute of Physics Publishing, 2001.

[16] P.W. Baumeister, "Radiant power flow and absorptance in thin films," *Appl. Opt.*, vol. 8, pp. 423-436, 1969.

[17] T.W. Allen, R.G. DeCorby, "Assessing the maximum transmittance of periodic metal-dielectric multilayers," *J. Opt. Soc. Am. B*, vol. 28, pp. 2529-2536, 2011.

[18] A.D. Rakic, A.B. Djurisic, J.M. Elazar, and M.L. Majewski, "Optical properties of metallic films for vertical-cavity optoelectronic devices," *Appl. Opt.*, vol. 37, pp. 5271-5283, 1998.

[19] W. Chen, M.D. Thoreson, S. Ishii, A.V. Kildishev, V.M. Shalaev, "Ultra-thin ultra-smooth and low-loss silver films on a germanium wetting layer," *Opt. Express*, vol. 18, pp. 5124-5134, 2010.

[20] D. Owens, C. Fuentes-Hernandez, B. Kippelen, “Optical properties of one-dimensional metal-dielectric photonic band-gap structures with low-index dielectrics,” *Thin Sol. Films*, vol. 517, pp. 2736-2741, 2009.

[21] R. Dragila, B. Luther-Davies, S. Vukovic, “High transparency of classically opaque metallic films,” *Phys. Rev. Lett.*, vol. 55, pp. 1117-1120, 1985.

[22] S. Tomita, T. Yokoyama, H. Yanagi, B. Wood, J.B. Pendry, M. Fujii, S. Hayashi, "Resonant photon tunneling via surface plasmon polaritons through one-dimensional metal-dielectric metamaterials,” *Opt. Express*, vol. 16, pp. 9942-9950, 2008.

[23] E. Ray, R. Lopez, “Numerical design and scattering losses of a one-dimensional metallo-dielectric multilayer with broadband coupling of propagating waves to plasmon modes in the visible range,” *J. Opt. Soc. Am. B*, vol. 28, pp. 1778-1781, 2011.

6 Fabrication and testing of dielectric-metal-dielectric multilayers

Although the study of dielectric-metal-dielectric filters in this thesis was primarily theoretical in nature, some preliminary experimental work was also done. This chapter outlines that work, which demonstrates some of the benefits of admittance matching of DMD multilayers. Further experimental studies are left for future work.

6.1 Admittance matching of SiO_2/Ag-based multilayer structures

For certain applications, DMD multilayers with low-index dielectric layers provide advantages such as lower loss, reduced nonlinearities, and ease of deposition [1]. However, the gap between T_{max} and PT_{MAX} is relatively large when the dielectric index is low, due to an unavoidable admittance mismatch with the external air medium. In terms of the equivalent layer representation discussed in Chapter 4, the effective index can assume real values but typically $n_{eff} \ll 1$ [2]. In principle, this index offset can be compensated (at a desired wavelength) by terminating the DMD cell or multilayer with an appropriate admittance matching assembly [2, 3, 4, 5, 6].

Figure 6.1 shows three different assemblies intended to mitigate admittance mismatches between a 5-period SiO_2/Ag multilayer and an ambient air medium. The first (m1) adds a single SiO_2 half-layer on both sides of the structure, forming a DMD unit cell like those studied in Chapters 4 and 5. The second (m2) adds a single TiO_2 layer with a similar phase thickness to the SiO_2 half-layer used in m1, and was intended to examine the effects of a higher-index outer layer. For the third structure (m3), the entire multilayer was designed to be an induced transmission filter at a wavelength of ~500 nm, according to the standard procedures described

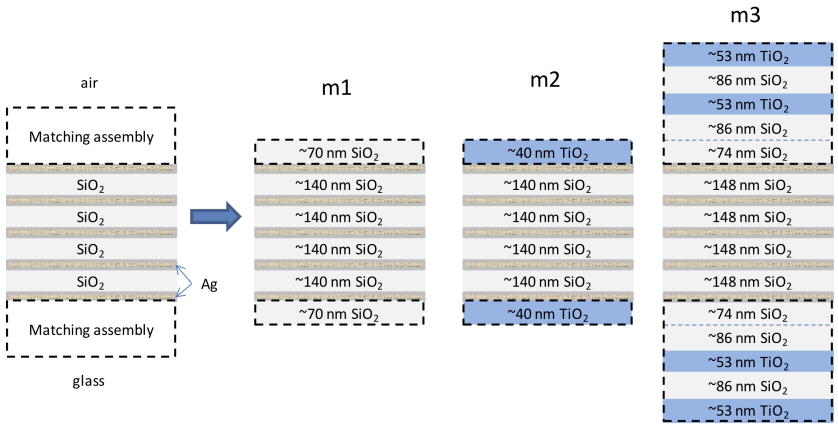

Figure 6.1: Schematic diagrams of SiO_2/Ag multilayers with matching assemblies for fabrication and use in simulations. The Ag layers are nominally ~25 nm thick.

in Chapter 7 of the textbook by Macleod[8]. The 74-nm SiO_2 layer is a phase-matching layer that converts the admittance of the 25-nm Ag films into a real value, and the Ag films were separated by SiO_2 layers of twice the phase-matching thickness. Finally, the structure was terminated on both ends by 2-period quarter-wave stacks (QWS) of TiO_2 and SiO_2 layers with quarter-wave thicknesses appropriate for the ~500-nm wavelength light. With appropriate choice of the number of periods, stacks transform the effective index of the multilayer to a value close to 1 [8]. For the design and for the transfer matrix simulations below, Ag optical constants were calculated from the Rakic model [10], TiO_2 optical constants were from the model of Kim [11], and a fixed index $n = 1.45$ was used for SiO_2. These models were verified by ellipsometric measurements (not shown) on TiO_2 and SiO_2 films. The presence of a glass substrate (instead of air) was also taken into account, but does not greatly affect the design or the predicted optical response.

Figure 6.2 shows the results of normal-incidence transfer matrix simulations (source code given in Appendix A) for both the unmatched multilayer and for sample m1, as shown in Figure 6.1. The addition of a simple half-layer significantly increases the transmittance of the metal-dielectric structure. The

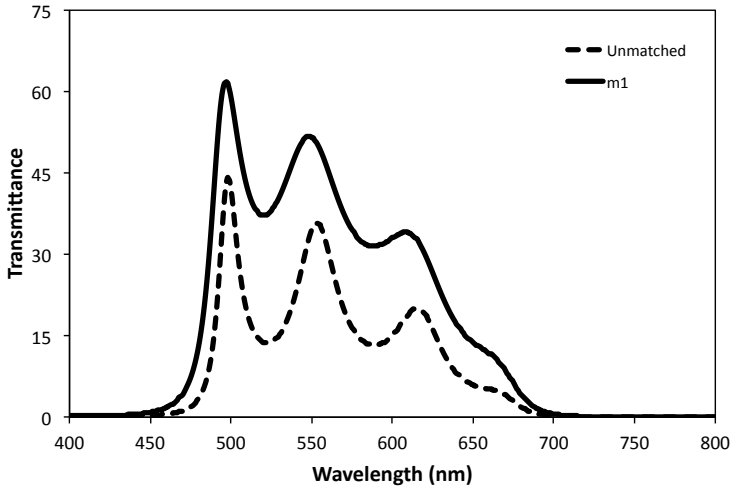

Figure 6.2: Simulated transmittance curves for the unmatched assembly and multilayer m1 shown in Figure 6.1.

results for the three multilayer structures, as well as a structure that uses TiO_2 exclusively for the dielectric (with 76-nm layers separating the Ag layers and the same 40-nm matching layer as in m2), are shown in Figure 6.3 (a). As expected, the m3 induced transmission filter has $T \sim \mathrm{PT_{MAX}}$ at the designed wavelength, at a cost of reduced bandwidth in comparison to the other structures. The simple design (m1) has a relatively low transmittance and significant ripple in the passband. In comparison, the m2 design shows higher transmittance, increased bandwidth and reduced ripple. It also has benefit of being simpler to implement than the induced transmission design, with only slightly lower transmittance. When compared to the structure using all TiO_2 layers, the m2 design shows a slightly higher peak transmittance and a reduced bandwidth. This behaviour is interesting in that it shows that some of the benefits associated with high-index dielectrics [1, 13, 14] can be obtained by replacing only the SiO_2 half-layer with TiO_2, and may be a useful compromise in some situations.

In preliminary experimental work, structures were grown in a multi-pocket e-beam evaporation system. Target materials were Ag, SiO_2, and TiO_2, and films were deposited onto glass substrates that had been previously cleaned using a

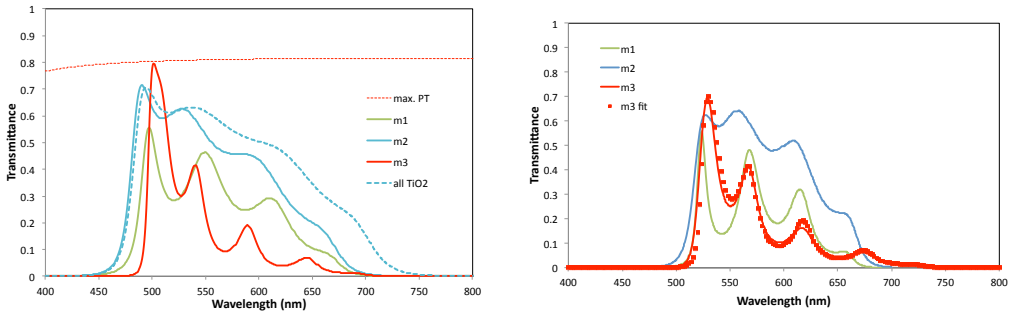

Figure 6.3: (a) Theoretical transmittance for the three multilayer structures shown in Figure 6.1. The additional blue dashed line shows the transmittance for a TiO_2-only structure, with the Ag layers spaced by 76-nm TiO_2 layers. The red dotted line shows the PT_{MAX} for a structure containing five 25-nm thick Ag films. (b) Experimental transmittance for the fabricated structures based on the three structures shown in Figure 6.1. The symbols show another theoretical prediction for m3, with the addition of a +7% error in the thickness of all SiO_2 layers that produces a better fit to the experimental result.

piranha solution. Chamber base pressure was $\sim 10^{-6}$ Torr. TiO_2 films (only) were deposited in an oxygen environment at pressure $\sim 5 \times 10^{-5}$ Torr, in order to ensure stoichiometry [11]. Normal-incidence transmittance curves were obtained using a VASE instrument (J.A. Woollam Co. Inc.) and verified using a spectrophotometer (Perkin-Elmer Lambda 900). The transmittance in each case was normalized to that for a blank glass substrate.

Experimental and theoretical results showed reasonable agreement (Figure 6.3), although the experimental transmittance was slightly less than the predicted value in each case. This reduction in transmittance was likely due in part to the use of Ag bulk constants in the simulation results, because thin films have a tendency to exhibit higher loss from roughness-induced scattering [1, 12]. The experimental curves also show a shift to higher wavelengths, which we attribute to a systematic error in the thickness of the SiO_2 layers. For example, introducing a 7% increase in thickness of the SiO_2 layers of the m3 structure produced a transmittance curve with a much better fit (as shown in Figure 6.3(b)). Another discrepancy shown by the curves is a slight reduction in bandwidth compared to the predicted curves. This

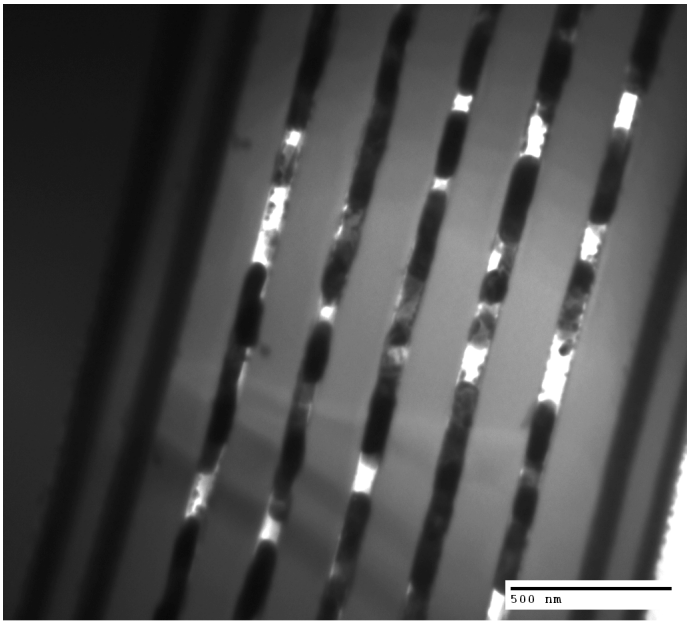

Figure 6.4: Cross-sectional TEM image of structure m3. The glass substrate is visible in the upper-left of the picture.

reduction could potentially be caused by random layer thickness errors, leading to a reduction in the splitting of the coupled cavity modes [7, 15]. Tighter controls in the deposition process could most likely reduce or eliminate these discrepancies. Nevertheless, the relative transparency and shape of the transmission curves show similar trends in the theoretical and experimental results.

We have also performed preliminary transmission electron microscopy (TEM) analysis of the samples, as shown for example in Figure 6.4, and the results are consistent with the aforementioned hypotheses. However, accurate thickness estimation was hindered by difficulties with sample preparation, which resulted in Ag layers appearing erroneously thick. Work aimed at improving the deposition accuracy and the TEM analysis of layer thickness is ongoing, and we hope to obtain a more complete set of experimental results in future work.

6.2 Transmission of oblique-incidence light through SiO_2/Ag multilayers

In addition to the measurements detailed above, preliminary measurements have been performed to determine the transmission response of the basic single-layer multilayers (m1 and m2) for oblique-incidence light. The m3 multilayer was not measured since it is an induced transmission filter designed specifically for normal incidence light. Transmission scans were obtained with a spectrophotometer (Perkin-Elmer Lambda 900), using a rotation stage to orient the sample to the desired incidence angle, and simulation results were obtained using the transfer matrix formulation code used in Section 6.1 and outlined in Appendix A, modified to calculate transmittance for both TE and TM waves for different incidence angles. Since the spectrometer's light source was unpolarized, the simulation results for TE and TM were averaged to find total transmittance values for comparison to the measured results. Results for m1 and m2 are shown in Figures 6.5 and 6.6, respectively.

As in the normal incidence case, the actual measured curves show a reduction in bandwidth and transmittance, as well as a shift to higher wavelengths. Despite these discrepancies, the shapes of the curves maintain a level of consistency between experiment and theory in terms of their shapes and an overall shift of the curves to lower wavelengths as the angle of incidence is increased. The change in number of peaks and curve shape remains consistent for different angles, even in a case such as the m2 multilayer at 30 degrees angle of incidence, where both the simulated and measured curves become smooth. However, as mentioned previously, a more controlled deposition process will be necessary for more accurate and predictable results to be obtained.

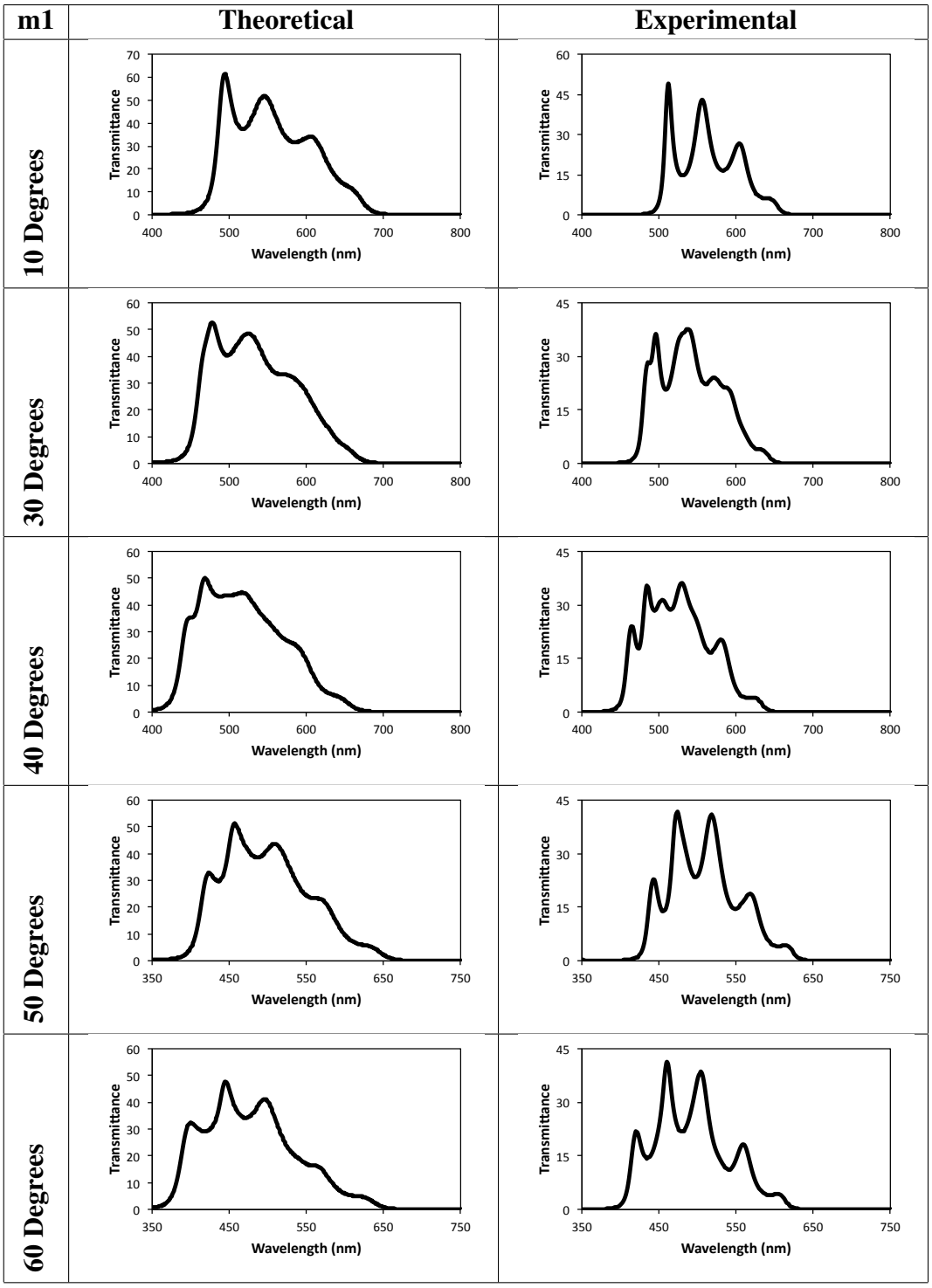

Figure 6.5: Theoretical and experimental transmittance curves at different light incidence angles (relative to normal) for the multilayer structure m1 shown in Figure 6.1. Theoretical transmittance was obtained by averaging the predicted transmittance for TE and TM polarization. The experimental and theoretical curves are plotted on different scales in order to facilitate comparison of their shapes.

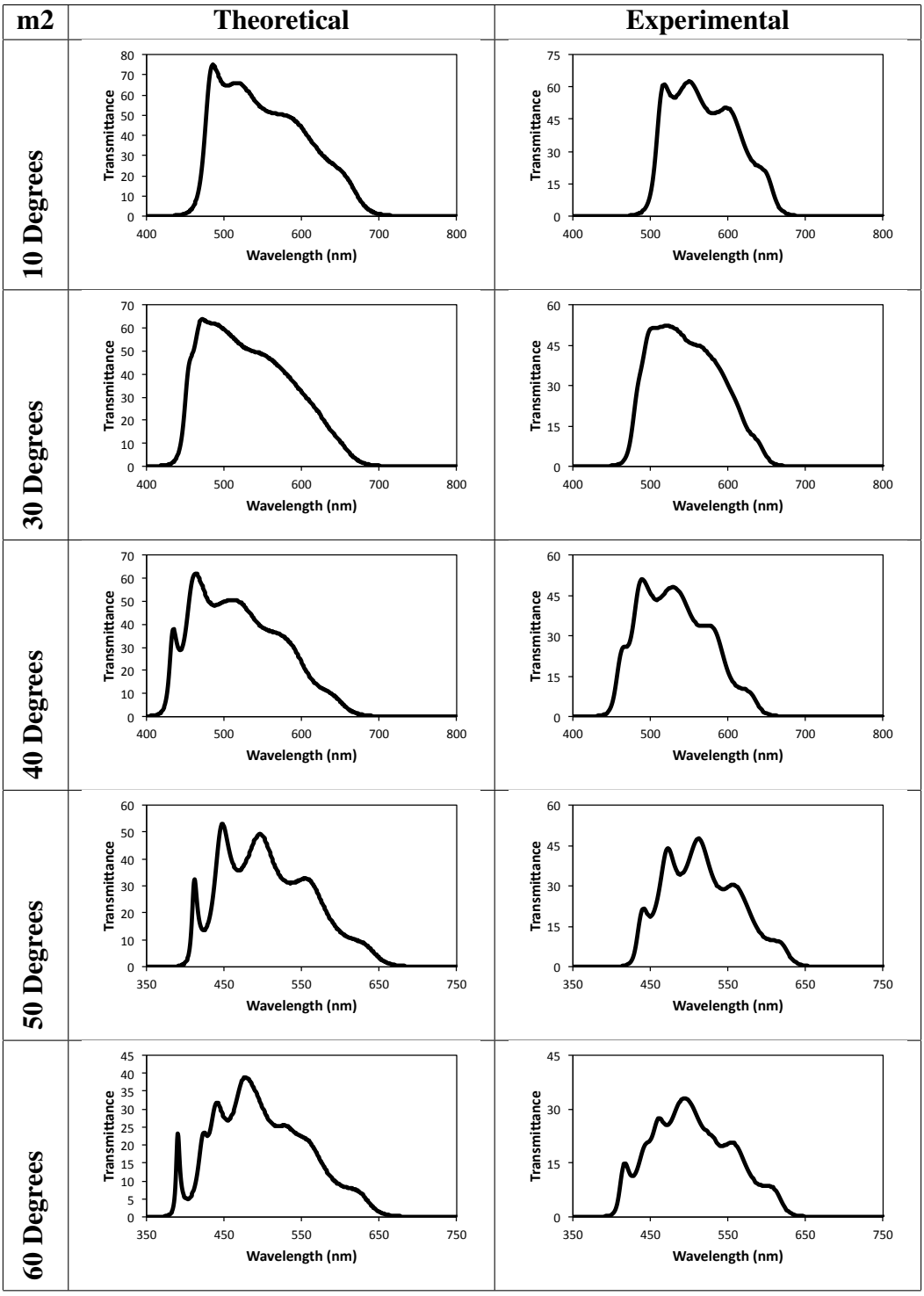

Figure 6.6: Theoretical and experimental transmittance curves at different light incidence angles (relative to normal) for the multilayer structure m2 shown in Figure 6.1. Theoretical transmittance was obtained by averaging the predicted transmittance for TE and TM polarization. The experimental and theoretical curves are plotted on different scales in order to facilitate comparison of their shapes.

References

[1] D. Owens, C. Fuentes-Hernandez, B. Kippelen, "Optical properties of one-dimensional metal-dielectric photonic band-gap structures with low-index dielectrics," *Thin Sol. Films*, vol. 517, pp. 2736-2741, 2009.

[2] B.V. Landau, P.H. Lissberger, "Theory of induced-transmission filters in terms of the concept of equivalent layers," *J. Opt. Soc.*, Am. vol. 62, pp. 1258-1264, 1972.

[3] P.H. Berning, A.F. Turner, "Induced transmission in absorbing films applied to band pass filter design," *J. Opt. Soc. Am.*, vol. 47, pp. 230-239, 1957.

[4] P.W. Baumeister, "Radiant power flow and absorptance in thin films," *Appl. Opt.*, vol. 8, pp. 423-436, 1969.

[5] H.A. Macleod, "A new approach to the design of metal-dielectric thin-film optical coatings," *Optica Acta*, vol. 25, pp. 93-106, 1978.

[6] P.H. Lissberger, "Coatings with induced transmission," *Appl. Opt.*, vol. 20, pp. 95-104, 1981.

[7] M.J. Bloemer, M. Scalora, "Transmissive properties of Ag/MgF_2 photonic band gaps," *Appl. Phys. Lett.*, vol. 72, pp. 1676-1678, 1998.

[8] H.A. Macleod, *Thin-Film Optical Filters, 3rd Edition*. Institute of Physics Publishing, 2001.

[9] H.A. Macleod, *Thin-Film Optical Filters, Third Edition*. Institute of Physics Publishing, 2001.

[10] A.D. Rakic, A.B. Djurisic, J.M. Elazar, and M.L. Majewski, "Optical properties of metallic films for vertical-cavity optoelectronic devices," *Appl. Opt.*, vol. 37, pp. 5271-5283, 1998.

[11] S. Y. Kim, "Simultaneous determination of refractive index, extinction coefficient, and void distribution of titanium dioxide thin film by optical methods," *Appl. Opt.*, vol. 35, pp. 6703-6707, 1996.

[12] M. Bloemer, G. D'Aguanno, N. Mattiucci, M. Scalora, N. Akozbek, "Broadband super-resolving lens with high transparency in the visible range," *Appl. Phys. Lett.*, vol. 90, 174113, 2007.

[13] M. Scalora, M.J. Bloemer, C.M. Bowden, "Laminated photonic band structures with high conductivity and high transparency: metals under a new light," *Optics and Photonics News*, vol. 10, pp. 24-27, 1999.

[14] Y.-K. Choi, Y.-K. Ha, J.-E. Kim, H.Y. Park, K. Kim, "Antireflection film in one-dimensional metallo-dielectric photonic crystals," *Opt. Comm.*, vol. 230, pp. 239-243, 2004.

[15] C.-S. Kee, K. Kim, H. Lim, "Optical resonant transmission in metal-dielectric multilayers," *J. Opt. A: Pure Appl. Opt.*, vol. 6, pp. 267-269, 1999.

7 Conclusions

7.1 Summary

This thesis describes several contributions that are relevant to the future development of integrated lab-on-a-chip systems. These include:

- The fabrication of novel resonant microcavities using buckling self-assembly. The cavities were shown to have good quality factor and finesse, and exhibited some of the cleanest Hermite- and Laguerre-Gaussian mode structures ever reported for on-chip microcavities.

- The application of potential transmittance theory to resonant tunneling through MD stacks, for both propagating and evanescent wave tunneling. To our knowledge, this work is the first to unify these separate classes of tunneling problems.

- The derivation of a general expression that encapsulates the admittance matching conditions for a dielectric-metal-dielectric unit cell, and for periodic structures based on such unit cells. We furthermore applied this admittance matching expression to the two classes of tunneling problems (i.e. tunneling of propagating and evanescent waves) mentioned above.

7.1.1 Resonant microcavities formed through buckling self-assembly

As summarized in Chapter 1, this thesis was partly motivated by previous work on microstructures fabricated by controlled buckling of multilayer films. After studying waveguides made with this technique [1, 2, 3], we turned our attention to dome-shaped microcavities, as outlined in Chapter 3. Arrays of cavities with diameters varying from 200-400 μm were fabricated in a Si/SiO_2 multilayer system and subsequently measured to determine their optical and morphological properties. Measurements of the profiles of the domes showed peak heights to be in agreement with those predicted by elastic buckling theory, and optical

transmission measurements showed the quality factor Q, finesse F and mode volume V_m to be similar or superior to those seen in other cavities reported in the literature [4, 5, 6]. The measured Q-factor and finesse of the domes were as high as 4×10^4 and 3×10^3, respectively, quite high for cavities on this scale [4]. The domes also allowed straightforward isolation of individual Hermite- and Laguerre-Gaussian modes, indicating a high degree of cylindrical symmetry in the shape of the cavities.

Buckling self-assembly is a novel method of manufacturing these cavities, given that these devices have typically been made using relatively time-intensive serial processing techniques [4, 5]. The buckling technique allows microcavity arrays to be quickly made in parallel using standard silicon processing methods such as film deposition and lithography. This process also allows for the creation of structures with very smooth features and highly regular shapes (verified by the high Q and F values measured for our domes), important properties for the creation of resonant cavities.

7.1.2 Optimization of transmittance of periodic metal-dielectric multilayers

Since bucking self-assembly has been shown to be a viable method of creating structures in multilayer thin films, we undertook a theoretical study of optimizing transmittance through metal layers, with the goal of eventually forming buckled structures within metal-dielectric (MD) multilayers. Thin metal films have several properties that make them desirable to various applications including filters, resonators and spectroscopic devices, and have seen a great deal of recent study as transparent conductors [7], in which it has been observed that metals (normally highly absorptive in bulk form) can be transparent for certain wavelengths when deposited as thin films and admittance matched using dielectric layers. We showed that transparency in MD multilayers is aptly explained by the theory of potential

transmittance (PT), developed by Berning and Turner in 1957 [8], a fact that has been somewhat under appreciated in current literature. Furthermore, we showed that PT theory is a useful tool for finding the upper limit on metal transparency, for both Fabry-Perot (propagating wave) and surface plasmon (evanescent wave) resonances. To our knowledge, ours is the first study that has unified these two tunneling mechanisms within a single theoretical framework. In combination with equivalent layer theory, it can also be used to help understand and clarify the conditions for admittance matching, and we found in general that to achieve a reasonably good admittance match, higher index dielectrics are needed as metal thickness is increased. This work is outlined in Chapter 4.

We extended our work into MD multilayers and derived an expression to find the conditions for reflection-less tunneling through a periodic stack with a dielectric-metal-dielectric unit cell. This equation was then used to examine admittance matching for different input light configurations. We found that for perfect matching with normal incidence light, a dielectric layer with specific and impractically large refractive index is needed. For TE-polarized light, perfect matching is obtainable for a specific incidence angle determined by the refractive indices of the dielectric and ambient media, and the thickness and refractive index of the metal. For TM-polarized light, perfect matching is possible in the evanescent wave regime. In all cases, matching occurred at a single wavelength and/or tunneling angle. This work is outlined in Chapter 5.

In addition, we also designed, fabricated and performed preliminary measurements on several different MD multilayer structures. A quarter-wave stack based structure designed to be an induced transmission filter showed transparency limited only by the potential transmittance of the metal layers, although at a cost of reduced bandwidth and increased fabrication complexity. A simpler design, using a single high-index matching layer on each end of the multilayer structure showed

a lesser increase in transmittance, but had a wider bandwidth that may be useful in appropriate applications. The single layer design also was improvable in transmission and bandwidth by using TiO_2 instead of SiO_2 as the matching layer.

7.2 Future work

7.2.1 Resonant microcavities formed through buckling self-assembly

The microcavities studied in Chapter 3 offer significant potential for future work. It should be possible to improve the Q and F of the cavities through improvements to the fabrication process; for example, reducing the absorption losses from the a-Si layers by replacing them with hydrogenated Si. In addition, the cavities could be tailored for shorter wavelength regions by using different dielectric materials such as TiO_2, assuming that they can be deposited in a way that induces the needed compressive stress in the layers. As mentioned in Chapter 3, the transmitted power from the domes experienced significant drift when input light was set to the dome resonant frequency. Further study could determine the source of the drift - whether it was due to thermal expansion from absorption in the mirrors, environmental factors such as humidity or temperature, radiation pressure induced by resonant photons in the cavity, or a combination of other factors. Moreover, these variations could be harnessed for useful applications such as sensing of temperature or pressure. Perhaps the most interesting possibility for future work is to integrate the domes with other hollow structures formed with buckling self-assembly. Hollow waveguide channels could potentially be used to introduce fluids or gases into the domes, which would present interesting options for microfluidic sensing applications. An early prototype of such a system is shown in Figure 7.1.

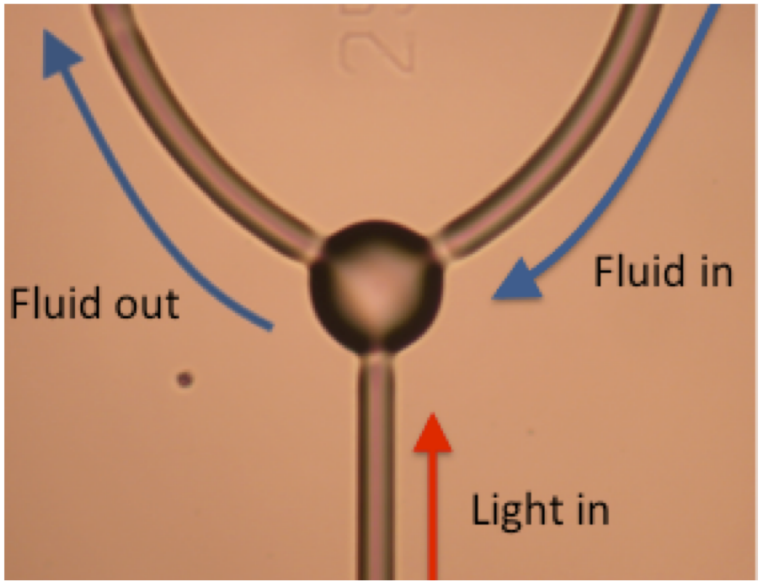

Figure 7.1: Example of a microfluidic system fabricated as a test to see if hollow waveguide channels and a dome microcavity could be integrated using the buckling self-assembly process. This device could potentially be used as a junction point to introduce a laser probe or pump beam into a fluid.

7.2.2 Optimization of transmittance of periodic metal-dielectric multilayers

Since our study of MD multilayers was primarily theoretical, the most obvious next step is to expand the experimental results to further verify the results seen in Chapters 4 and 5. In addition, further theoretical studies are warranted. For example, in our study of the maximization of transmission of evanescent waves, we limited our scope to waves in a prism coupling system. It would be interesting to extend the study to a consideration of other coupling systems, such as diffraction gratings. Also, it could be interesting to study the effect of matching assemblies consisting of multiple dielectric layers with different refractive indices, to see their effect on the transmission spectrum of the overall MD multilayer structure. A final possibility for future work would be to combine the knowledge obtained on maximizing transmittance through MD multilayers with the microstructures made through buckling self-assembly. Adding metal to these structures might provide for mirrors with better reflectance or interesting spectral

transmittance properties, making them highly useful for many applications such as optical resonators, filters and superlenses. However, much work would need to be done to determine the effects of the metal layers on the buckling process.

References

[1] R.G. DeCorby, N. Ponnampalam, H.T. Nguyen, M.M. Pai, T.J. Clement, "Guided self-assembly of integrated hollow Bragg waveguides", *Opt. Express*, vol. 15, pp. 3902-3915, 2007.

[2] E. Epp, N. Ponnampalam, J.N. McMullin, R.G. DeCorby, "Thermal tuning of hollow waveguides fabricated by controlled thin-film buckling", *Opt. Express*, vol. 17, pp. 17369-17375, 2009.

[3] E. Epp, N. Ponnampalam, W. Newman, B. Drobot, J.N. McMullin, A.F. Meldrum, R.G. DeCorby, "Hollow Bragg waveguides fabricated by controlled buckling of Si/SiO_2 multilayers", *Opt. Express*, vol. 18, pp. 24917-24925, 2010.

[4] P. R. Dolan, G.M. Hughes, F. Grazioso, B.R. Patton, J.M. Smith, "Femtoliter tunable optical cavity arrays," *Opt. Lett.*, vol. 35, pp. 3556-3558, 2010.

[5] A. Muller, E.B. Flagg, J.R. Lawall, G.S. Solomon, "Ultrahigh-finesse, low-mode-volume Fabry-Perot microcavity," *Opt. Lett.*, vol. 35, pp. 2293-2295, 2010.

[6] M. Trupke, E.A. Hinds, S. Eriksson, E. A. Curtis, Z. Moktadir, E. Kukharenka, M. Kraft, "Microfabricated high-finesse optical cavity with open access and small volume," *Appl. Phys. Lett.*, vol. 87, 211106, 2005.

[7] M.J. Bloemer, M. Scalora, "Transmissive properties of Ag/MgF_2 photonic band gaps," *Appl. Phys. Lett.*, vol. 72, pp. 1676-1678, 1998.

[8] P.H. Berning, A.F. Turner, "Induced transmission in absorbing films applied to band pass filter design," *J. Opt. Soc. Am.*, vol. 47, pp. 230-239, 1957.

Appendix A: Source code

Determination of optimal admittance matching conditions for a DMD multilayer structure (Chapter 5)

Normal incidence case

This Matlab file calculates the dielectric index required to maximize the potential transmittance of a silver film embedded in air, as a function of film thickness and at a single wavelength for normal incidence light. Results obtained from this code can be seen in Figure 5.4(a) and (b).

```
% Inputs
% lam - free-space wavelength
AgOpCon; %Matlab file that calculates the optical constants of
Ag
nAg=nAgv;
kAg=kAgv;
dAg=9.9e-9;
qa=0;
Xo=1.5;
while Xo>1.1;
   dAg=dAg+0.05e-9;
   qa=qa+1;
   dAgnm(qa)=dAg*1e9;
   aAg=2*pi*nAg*dAg/lam; % Real part of effective phase
thickness of Ag layer
   bAg=2*pi*kAg*dAg/lam; % Imaginary part of effective phase
thickness of Ag layer
   %Calculations for quantities used in equations for Xo and Zo:
   sa=sin(aAg);
   ca=cos(aAg);
   cb=cos(bAg);
   sb=sin(bAg);
   sha=sinh(aAg);
```

```
   shb=sinh(bAg);
   cha=cosh(aAg);
   chb=cosh(bAg);
   Xo=sqrt(((nAg^2+kAg^2)*(nAg*shb*chb+kAg*sa*ca)/(nAg*shb*chb
-kAg*sa*ca))-(nAg^2*kAg^2*(sa^2*chb^2+ca^2*shb^2)^2
/(nAg*shb*chb-kAg*sa*ca)^2));
   Zo=nAg*kAg*(sa^2*chb^2+ca^2*shb^2)/(nAg*shb*chb-kAg*sa*ca);
   Xv(qa)=Xo;
   Zv(qa)=Zo;
   A=2*Zo/Xo;
   ndmin=(A+sqrt(A^2+4))/2;
   Xndm=2*ndmin^2/(ndmin^2+1);
   PTi=(((nAg^2-kAg^2)-2*nAg*kAg*(Zo/Xo))/(nAg^2+kAg^2))
*(sa^2*chb^2+ca^2*shb^2)+(ca^2*chb^2+sa^2*shb^2)
+(nAg*shb*chb+kAg*sa*ca)/Xo+(nAg*shb*chb-kAg*sa*ca)
*(Xo^2+Zo^2)/(Xo*(nAg^2+kAg^2));
   PTm(qa)=1/PTi; %maximum potential transmittance of the Ag
film at current wavelength

   if Xo>Xndm
   nop(qa)=fzero('nopt2',4.5,[],Xo,Zo); % Solves Equation 5.6 to
find optimal index, see below for nopt3
   del=0.5*(pi-asin(2*Zo/(Xo*(nop(qa)-1/nop(qa)))));
   dop=del*lam/(2*pi*nop(qa)); % Calculates optimal thickness
based on optimal index
   dopnm(qa)=1e9*dop;
   else
   nop(qa)=fminsearch('nopt3',4.5,[],Xo,Zo); % Solves Equation
5.6 to find optimal index, see below for nopt3
   del=0.5*(asin(2*Zo/(Xo*(nop(qa)-1/nop(qa)))));
   dop=del*lam/(2*pi*nop(qa)); % Calculates optimal thickness
based on optimal index
   dopnm(qa)=1e9*dop;
   end

end
%
```

```
subplot(2,2,1)
plot(dAgnm,nop)
subplot(2,2,3)
plot(dAgnm,dopnm)
```

nopt2:

This Matlab file encodes the equation for the dielectric refractive index (Equation 5.6) that results in optimal impedance matching of a thin Ag film in air, bounded by a single dielectric layer on each side. The real value of the equation is taken to eliminate numerical noise introduced by Matlab, and is intented for use with the built-in function fzero, for cases where Xo>Xndm.

```
function nd=nopt2(nD,Xz,Zz)
nd=real(2+Xz*(cos(asin(2*Zz/(Xz*(nD-1/nD))))*(1-(1/nD^2))
-(1+(1/nD^2))));
```

nopt3:

This Matlab file encodes the equation for the dielectric refractive index (Equation 5.6) that results in optimal impedance matching of a thin Ag film in air, bounded by a single dielectric layer on each side. The absolute value of the equation is taken to eliminate numerical noise introduced by Matlab, and is intended for use with the built-in function fminsearch, which was found to be more robust for cases where Xo<Xndm.

```
function nd=nopt3(nD,Xz,Zz)
nd=abs(2+Xz*(-cos(asin(2*Zz/(Xz*(nD-1/nD))))*(1-(1/nD^2))
-(1+(1/nD^2))));
```

TE-polarized case

This Matlab code calculates the angular position of the impedance-matched TE tunneling peak versus metal thickness, for a fixed dielectric spacer index, fixed

'prism' index, and fixed wavelength. The data obtained using this code is shown in Figure 5.5(a) and (b).

```
% % Inputs
% dAgv - vector of thicknesses for the Ag film
% lam - free-space wavelength
dAgnm=dAgv*1e9;
AgOpCon; %Matlab file that calculates the optical constants of
Ag
Nm1=nAgv-i*kAgv;
nd1=2.3; %index of dielectric spacer layer
np1=1.5; %index of input/output media

kop1=1; %initial guess for the fzero function
for qa=1:length(dAgv);
   dm1=dAgv(qa);
   kop(qa)=fzero('noptTE',kop1,[],nd1,np1,Nm1,dm1,lam); % Solves
Equation 5.6 to find optimal angle (in terms of transverse wave
vector), see below for noptTE
   kop1=kop(qa);
   dop=doptTE(kop(qa),nd1,np1,Nm1,dm1,lam); % Calculates optimal
thickness, see below for doptTE
   dopnm(qa)=1e9*dop;
end

angop=(180./pi).*asin(kop./np1);
subplot(2,2,1)
plot(dAgnm,angop)
subplot(2,2,3)
plot(dAgnm,dopnm)
```

noptTE:

This Matlab file encodes the equation for the angle in terms of transverse wavevector (ktt) for TE polarization that results in optimal impedance matching of a thin metal film (Nm1), bounded by a single dielectric layer (n1) on each side, and coupled by identical input/output dielectric media (n2).

```
function ktt=noptTE(kt,n1,n2,Nm1,dm1,lam1)
```

```
   angm=asin(kt/Nm1); %complex angle in the Ag medium
   ang1=asin(kt/n1); %imaginary angle in bounding dielectric
layers
   ang2=asin(kt/n2); %real angle in 'prism' media
   i1=conj(n1*cos(ang1)); %admittance of dielectric layers for
TE polarization
   i2=conj(n2*cos(ang2)); %admittance of prism media for TE
polarization
   nm1=real(Nm1);
   km1=abs(real(Nm1));
   dM=(2*pi/lam1)*dm1*Nm1*cos(angm);
   iM=Nm1*cos(angm);
   aAg=real(dM);
   bAg=-imag(dM);
   iR=real(iM);
   iI=-imag(iM);
   sa=sin(aAg);
   ca=cos(aAg);
   cb=cos(bAg);
   sb=sin(bAg);
   sha=sinh(aAg);
   shb=sinh(bAg);
   cha=cosh(aAg);
   chb=cosh(bAg);
   Xz=sqrt(((iR^2+iI^2)*(iR*shb*chb+iI*sa*ca)/(iR*shb*chb
-iI*sa*ca))-(iR^2*iI^2*(sa^2*chb^2+ca^2*shb^2)^2
/(iR*shb*chb-iI*sa*ca)^2));
   Zz=iR*iI*(sa^2*chb^2+ca^2*shb^2)/(iR*shb*chb-iI*sa*ca);
   ktt=real(2*i2+Xz*(cos(asin(2*Zz/(Xz*(i1/i2-i2/i1))))*(1
-(i2^2/i1^2))-(1+(i2^2/i1^2))));
```

doptTE:

This Matlab file encodes the equation to calculate the thickness of the dielectric layers that produces an optimal impedance match for a DMD structure, once the optimal tunneling angle has been determined from noptTE.m.

```
function dop1=doptTE(kt,n1,n2,Nm1,dm1,lam1)
   angm=asin(kt/Nm1); %complex angle in the Ag medium
   ang1=asin(kt/n1); %imaginary angle in bounding dielectric
layers
   ang2=asin(kt/n2); %real angle in 'prism' media
   i1=conj(n1*cos(ang1)); %admittance of dielectric layers for
TE polarization
   i2=conj(n2*cos(ang2)); %admittance of prism media for TE
polarization
   nm1=real(Nm1);
   km1=abs(real(Nm1));
   dM=(2*pi/lam1)*dm1*Nm1*cos(angm);
   iM=Nm1*cos(angm);
   aAg=real(dM);
   bAg=-imag(dM);
   iR=real(iM);
   iI=-imag(iM);
   sa=sin(aAg);
   ca=cos(aAg);
   cb=cos(bAg);
   sb=sin(bAg);
   sha=sinh(aAg);
   shb=sinh(bAg);
   cha=cosh(aAg);
   chb=cosh(bAg);
   Xz=sqrt(((iR^2+iI^2)*(iR*shb*chb+iI*sa*ca)/(iR*shb*chb
-iI*sa*ca))-(iR^2*iI^2*(sa^2*chb^2+ca^2*shb^2)^2
/(iR*shb*chb-iI*sa*ca)^2));
   Zz=iR*iI*(sa^2*chb^2+ca^2*shb^2)/(iR*shb*chb-iI*sa*ca);
   del=0.5*(pi-asin(2*Zz/(Xz*(i1/i2-i2/i1))));
   dop1=real(del*lam1/(2*pi*n1*cos(ang1)));
```

TM-polarized case

This Matlab file calculates the angular position of the impedance matched surface-plasmon mediated tunneling peak versus wavelength, for a fixed dielectric spacer index, fixed 'prism' index, and fixed metal thickness. Results obtained using this code can be found in Figure 5.6(a) and (b) and Figure 5.7(a) and (b).

```
% Inputs
% dAgv - vector of thicknesses for the Ag film
% lam - free-space wavelength
% dAgnm=dAgv*1e9;
AgOpCon; %Matlab file that calculates the optical constants of
Ag
Nm1=nAgv-i*kAgv;
nd1=1.38;%1.631;%; %index of dielectric spacer layer
np1=1.515;%4;% %index of coupling 'prisms'
kop1=1.4;%3.8;%0.2; % initial guess for fzero function
for qa=1:length(dAgv);
   dm1=dAgv(qa);
   kop(qa)=fzero('noptSP',kop1,[],nd1,np1,Nm1,dm1,lam); % Solves
Equation 5.6 to find optimal angle (in terms of transverse wave
vector), see below for noptSP
   kop1=kop(qa);
   dop=doptSP(kop(qa),nd1,np1,Nm1,dm1,lam);
   dopnm(qa)=abs(1e9*dop);
end
angop=(180./pi).*asin(kop./np1);
subplot(2,2,1)
plot(dAgnm,kop)
subplot(2,2,3)
plot(dAgnm,dopnm)
```

noptSP:

This Matlab file encodes the equation for the tunneling angle in terms of transverse wavevector (ktt) that results in optimal impedance matching of a thin

metal film (Nm1), bounded by a single dielectric layer (n1) on each side, and coupled by high index input/output 'prisms' (Nm1,dm1).

```
function ktt=noptSP(kt,n1,n2,Nm1,dm1,lam1)
   angm=asin(kt/Nm1); %complex angle in the Ag medium
   ang1=asin(kt/n1); %imaginary angle in bounding dielectric
layers
   ang2=asin(kt/n2); %real angle in 'prism' media
   i1=conj(n1/cos(ang1)); %admittance of dielectric layers for
TM polarization
   i2=conj(n2/cos(ang2)); %admittance of prism media for TM
polarization
   nm1=real(Nm1);
   km1=abs(real(Nm1));
   dM=(2*pi/lam1)*dm1*Nm1*cos(angm);
   iM=Nm1/cos(angm);
   aAg=real(dM);
   bAg=-imag(dM);
   iR=real(iM);
   iI=-imag(iM);
   sa=sin(aAg);
   ca=cos(aAg);
   cb=cos(bAg);
   sb=sin(bAg);
   sha=sinh(aAg);
   shb=sinh(bAg);
   cha=cosh(aAg);
   chb=cosh(bAg);
   Xz=sqrt(((iR^2+iI^2)*(iR*shb*chb+iI*sa*ca)/(iR*shb*chb
-iI*sa*ca))-(iR^2*iI^2*(sa^2*chb^2+ca^2*shb^2)^2
/(iR*shb*chb-iI*sa*ca)^2));
   Zz=iR*iI*(sa^2*chb^2+ca^2*shb^2)/(iR*shb*chb-iI*sa*ca);
   ktt=real(2*i2+Xz*(-cos(asin(2*Zz/(Xz*(i1/i2-i2/i1))))*(1
-(i2^2/i1^2))-(1+(i2^2/i1^2))));
```

doptSP:

This Matlab file encodes the equation to calculate the thickness of the dielectric layers that produces an optimal impedance match for a DMD structure, once the optimal tunneling angle has been determined from noptSP.m.

```
function dop1=doptSP(kt,n1,n2,Nm1,dm1,lam1)
   angm=asin(kt/Nm1); %complex angle in the Ag medium
   ang1=asin(kt/n1); %imaginary angle in bounding dielectric
layers
   ang2=asin(kt/n2); %real angle in 'prism' media
   i1=conj(n1/cos(ang1)); %impedance of dielectric layers for TM
polarization
   i2=conj(n2/cos(ang2)); %impedance of prism media for TM
polarization
   nm1=real(Nm1);
   km1=abs(real(Nm1));
   dM=(2*pi/lam1)*dm1*Nm1*cos(angm);
   iM=Nm1/cos(angm);
   aAg=real(dM);%2*pi*nAg*dAg/lam;
   bAg=-imag(dM);%2*pi*kAg*dAg/lam;
   iR=real(iM);
   iI=-imag(iM);
   sa=sin(aAg);
   ca=cos(aAg);
   cb=cos(bAg);
   sb=sin(bAg);
   sha=sinh(aAg);
   shb=sinh(bAg);
   cha=cosh(aAg);
   chb=cosh(bAg);
   Xz=sqrt(((iR^2+iI^2)*(iR*shb*chb+iI*sa*ca)/(iR*shb*chb
-iI*sa*ca))-(iR^2*iI^2*(sa^2*chb^2+ca^2*shb^2)^2
/(iR*shb*chb-iI*sa*ca)^2));
   Zz=iR*iI*(sa^2*chb^2+ca^2*shb^2)/(iR*shb*chb-iI*sa*ca);
   del=0.5*asin(2*Zz/(Xz*(i1/i2-i2/i1)));
   dop1=-real(del*lam1/(2*pi*n1*cos(ang1)));
```

Transfer matrix simulation of admittance-matched multilayer structures (Chapter 6)

This Matlab code simulates the optical reflectance, transmittance, absorbance, and potential transmittance versus wavelength for various incidence angles of a periodic metal-dielectric-metal structure, for both TE and TM polarization. The file is set up for a half-space of air on the incident side and a fixed index 'substrate' on the transmission side of the multilayer. The transfer matrix formulation for TE polarization is taken from the 4th edition of the text, *Optics*, by Eugene Hecht [1], and the TM is taken from the 7th edition of *Principles of Optics* by Max Born and Emil Wolfe [2]. The transfer matrix formulations and variables used here are specific to the structures detailed in Chapter 6, but different structures can easily be implemented by defining layer thicknesses and periods for the multilayers structures, calculating the characteristic matrices of the layers, and multiplying the matrices to obtain an overall structure matrix.

```
% % % User inputs
% dl - thickness of the low index (SiO2) layers
% dli - thickness of the low index (SiO2) 'antireflection' phase
matching
% layers (if used), assumed same at input and output sides.
% dh - thickness of the high index (TiO2) layers
% dhi - thickness of high index (TiO2) 'antireflection' layers,
if used.
% dAg - thickness of metal (Ag) layers
% zo - integer number of periods in mirror
% lambda0 - vector of free-space wavelengths
imp=376.8; % impedance of free space
thetain=(pi/180)*[0 10 30 40 50 60]; % vector of input angles,
relative to normal
% Indices for the low and high index layers:
nl=1.45; %modify these as necessary
```

```
AgOpCon; %Matlab file that calculates the optical constants of
Ag
TiO2OpCon; %Matlab file that calculates the optical constants of
TiO2
n=ntio2;
nsub=1; % fixed substrate index

for qt=1:length(thetain)
   angin=thetain(qt);
   for ql=1:length(lambda0)
   nh=n(ql);
   nAg=nAgv(ql);
   kAg=kAgv(ql);
   NAg=nAg-i*kAg;
   lam=lambda0(ql); %current free space wavelength
```

Snell's law is used to determine the angle in each type of layer at the current wavelength and air incidence angle:

```
   angl=asin(sin(angin)/nl); %angle in low index layers
   angh=asin(sin(angin)/nh); %angle in high index layers
   angAg=asin(sin(angin)/NAg); %angle in Ag layers
   angS=asin(sin(angin)/nsub); %angle in substrate
```

Parameters that go into the Hecht transfer matrix formulation are calculated for each type of layer:

```
   kohl=(2*pi/lam)*nl*dl*cos(angl); %phase thickness of low n
layers
   kohli=(2*pi/lam)*nl*dli*cos(angl); %phase thickness of low n
AR layers
   kohh=(2*pi/lam)*nh*dh*cos(angh); %phase thickness of high n
layers
   kohAg=(2*pi/lam)*NAg*dAg*cos(angAg); %phase thickness of Ag
layers
   yote=cos(angin)/imp; %effective admittance of air for TE
polarization
```

```
   zotm=cos(angin)*imp; %effective impedance of air for TM
polarization
   ylte=nl*cos(angl)/imp; %effective admittance of low index
layers for TE
   zltm=(cos(angl)*imp)/nl; %effective impedance of low index
layers for TM
   yhte=nh*cos(angh)/imp; %effective admittance of high index
layers for TE
   zhtm=(cos(angh)*imp)/nh; %effective impedance of high index
layers for TM
   yAgte=NAg*cos(angAg)/imp; %effective admittance of Ag layers
for TE
   zAgtm=(cos(angAg)*imp)/NAg; %effective impedance of Ag layers
for TM
   yste=nsub*cos(angS)/imp;%effective admittance of substrate
for TE
   zstm=(cos(angS)*imp)/nsub; %effective impedance of substrate
for TM
```

The transfer matrices for each type of layer at the current wavelength and indicent angle are calcuated for both TE and TM polarization:

```
   mlte=[cos(kohl) i*sin(kohl)/ylte; i*ylte*sin(kohl)
cos(kohl)];
   mlite=[cos(kohli) i*sin(kohli)/ylte; i*ylte*sin(kohli)
cos(kohli)];
   mltm=[cos(kohl) i*sin(kohl)/zltm; i*zltm*sin(kohl)
cos(kohl)];
   mlitm=[cos(kohli) i*sin(kohli)/zltm; i*zltm*sin(kohli)
cos(kohli)];
   mhte=[cos(kohh) i*sin(kohh)/yhte; i*yhte*sin(kohh)
cos(kohh)];
   %mhite=[cos(kohhi) i*sin(kohhi)/yhte; i*yhte*sin(kohhi)
cos(kohhi)];
   mhtm=[cos(kohh) i*sin(kohh)/zhtm; i*zhtm*sin(kohh)
cos(kohh)];
```

```
   %mhitm=[cos(kohhi) i*sin(kohhi)/zhtm; i*zhtm*sin(kohhi)
cos(kohhi)];
   mAgte=[cos(kohAg) i*sin(kohAg)/yAgte; i*yAgte*sin(kohAg)
cos(kohAg)];
   mAgtm=[cos(kohAg) i*sin(kohAg)/zAgtm; i*zAgtm*sin(kohAg)
cos(kohAg)];
```

Next, the overall transfer matrices for the multilayer at the current wavelength and incident angle are calculated, for both TE and TM. These matrices describe the overall structure of the multilayer, and can be customized to any given structure as long as the characteristic matrix of the layer can be calculated as in the above lines of code. The overall matrix for the first admittance-matched multilayer (m1) in Chapter 6 is shown here for illustrative purposes.

```
   mte=(mlte*mAgte*mlte)^zo; %multilayer 1
   mtm=(mltm*mAgtm*mltm)^zo; %multilayer 1
```

The amplitude reflection coefficients at the current incident angle and wavelength are calculated:

```
   rte=(yote*mte(1,1)+yote*yste*mte(1,2)-mte(2,1)
-yste*mte(2,2))/(yote*mte(1,1)+yote*yste*mte(1,2)+mte(2,1)
+yste*mte(2,2));
   rtm=(zotm*mtm(1,1)+zotm*zstm*mtm(1,2)-mtm(2,1)
-zstm*mtm(2,2))/(zotm*mtm(1,1)+zotm*zstm*mtm(1,2)+mtm(2,1)
+zstm*mtm(2,2));
   tte=(2*yote)/(yote*mte(1,1)+yote*yste*mte(1,2)+mte(2,1)
+yste*mte(2,2));
   ttm=(2*zotm)/(zotm*mtm(1,1)+zotm*zstm*mtm(1,2)+mtm(2,1)
+zstm*mtm(2,2));
```

The reflectances, transmittances and potential transmittances at the current incident angle and wavelength are calculated and stored:

```
   Rte(qt,ql)=rte*conj(rte);
   Rtm(qt,ql)=rtm*conj(rtm);
```

```
    Tte(qt,ql)=tte*conj(tte)*nsub*cos(angS)/cos(angin);
    Ttm(qt,ql)=ttm*conj(ttm)*cos(angS)/(nsub*cos(angin));
    PTte(qt,ql)=Tte(qt,ql)/(1-Rte(qt,ql));
    PTtm(qt,ql)=Ttm(qt,ql)/(1-Rtm(qt,ql));
    end
end
```

The values for TE and TM polarizations are averaged to find total reflectance, transmittance and potential transmittance:

```
Ravg=(Rte+Rtm)./2;
Tavg=(Tte+Ttm)./2;
PTavg=(PTte+PTtm)./2;
```

For the simulations in Chapter 6, the following values and overall matrix equations were used:

m0 - Unmatched multilayer

```
    dl=140e-9
    dAg=25e-9
    zo=4
    mte=(mAgte*mlte)^zo*mAgte
    mtm=(mAgtm*mltm)^zo*mAgtm
```

m1 - Single SiO_2 matching layer

```
    dl=70e-9*
    dAg=25e-9
    zo=5
    mte=(mlte*mAgte*mlte)^zo
    mtm=(mltm*mAgtm*mltm)^zo
```

* In the m1 multilayer, the 140-nm SiO_2 layers are viewed as two 70-nm layers put together for the sake of simplicity in the overall matrix formula.

m2 - Single TiO_2 matching layer

```
    dl=140e-9
    dh=40e-9
    dAg=25e-9
```

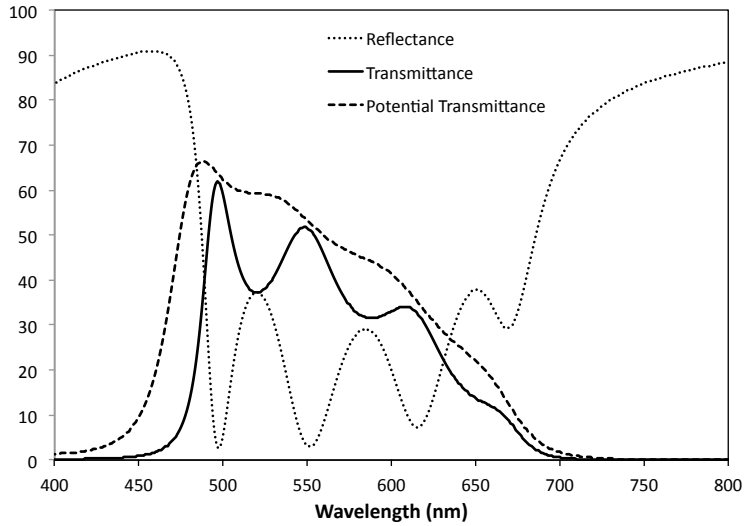

Figure A.1: Curves for reflectance, transmittance and potential transmittance of multilayer m1 at normal incidence, calculated using transfer matrix code.

```
zo=4
mte=mhte*(mAgte*mlte)^zo*mAgte*mhte
mtm=mhtm*(mAgtm*mltm)^zo*mAgtm*mhtm
```

m3 - Induced transmission filter design at 500-nm wavelength

```
dl=74e-9
dli=86e-9
dh=53e-9
dAg=25e-9
zo=5
mte=(mhte*mlite)^2*(mlte*mAgte*mlte)^zo*(mlite*mhte)^2
mtm=(mhtm*mlitm)^2*(mltm*mAgtm*mltm)^zo*(mlitm*mhtm)^2
```

An example of typical data obtained from this program is shown in Figure A.1, for the m1 multilayer at normal incidence.

References

[1] E. Hecht, *Optics, 4th Edition*. Addison Wesley, 2001.

[2] M. Born and E. Wolfe, *Principles of Optics: Electromagnetic Theory of Propagation, Interference and Diffraction of Light*. Cambridge University Press, 1999.

Appendix B: Detailed derivation of DMD admittance matching equation

In Chapter 5, an admittance matching expression for a dielectric-metal-dielectric multilayer was derived using equations from the textbook by Macleod [1]. This equation predicts that for a given metal layer (with a corresponding optimal admittance, $Y_{op} = X_{op} + iZ_{op}$), the admittance match to the dielectric layers depends only on the values of admittances of the dielectric and surrounding material (η_1 and η_2, respectively). This appendix demonstrates the derivation of this equation in more detail.

The derivation begins with the equation for the admittance seen by the metal layer looking into a single thin film (with real index n_1 and admittance η_1) on an infinitely thick substrate (with index n_2 and admittance η_2):

$$Y_{out} = \frac{\eta_2 \cos\delta_1 + i\eta_1 \sin\delta_1}{\cos\delta_1 + i(\eta_2/\eta_1)\sin\delta_1}, \tag{B.1}$$

where δ_1 is the phase thickness of the dielectric film. Multiplying the numerator and denominator by the complex conjugate of the denominator produces a result easily split into its real and imaginary components:

$$Y_{out} = \frac{\eta_2 + i\left(\eta_1 - \left(\eta_2^2/\eta_1\right)\right)\cos\delta_1 \sin\delta_1}{\cos^2\delta_1 + \left(\eta_2^2/\eta_1^2\right)\sin^2\delta_1}, \tag{B.2}$$

where the trigonometric identity $\cos^2\delta_1 + \sin^2\delta_1 = 1$ has been used to simplify the real portion of the equation. Next, the real and imaginary portions can be equated to the real and imaginary portions of the optimal admittance:

$$X_{op} = \frac{\eta_2}{\cos^2\delta_1 + \left(\eta_2^2/\eta_1^2\right)\sin^2\delta_1}, \tag{B.3}$$

$$Z_{op} = \frac{\left(\eta_1 - \left(\eta_2^2/\eta_1\right)\right)\cos\delta_1 \sin\delta_1}{\cos^2\delta_1 + \left(\eta_2^2/\eta_1^2\right)\sin^2\delta_1} \tag{B.4}$$

Dividing the two equations leads to the following expression:

$$\frac{X_{op}}{Z_{op}} = \frac{\eta_2}{\cos\delta_1 \sin\delta_1 \left(\eta_1 - \left(\eta_2^2/\eta_1\right)\right)}, \tag{B.5}$$

which, after slight manipulation and the use of the identity $\sin 2\delta_1 = 2\cos\delta_1 \sin\delta_1$, becomes:

$$X_{op} = \frac{2Z_{op}}{\sin 2\delta_1 \left(\frac{\eta_1}{\eta_2} - \frac{\eta_2}{\eta_1}\right)}. \tag{B.6}$$

Solving for the phase thickness δ_1:

$$2\delta_1 = \sin^{-1}\left(\frac{2Z_{op}}{X_{op}\left(\frac{\eta_1}{\eta_2} - \frac{\eta_2}{\eta_1}\right)}\right) \tag{B.7}$$

This equation gives the dielectric phase thickness necessary for an admittance match for the specified metal layer, and can be substitued into the equation for phase thickness ($\delta_1 = (2\pi/\lambda) n_1 d_1 \cos\theta_1$) to obtain Equation 5.7. Next, if the squared cos and sin in the denominator of Equation B.3 are replaced using the identities $\cos^2\delta_1 = (1+\cos 2\delta_1)/2$ and $\sin^2\delta_1 = (1-\cos 2\delta_1)/2$, Equation B.7 can be substituted in to the resulting equation to obtain the impedance matching expression shown in Equation 5.6:

$$X_{op} = \frac{2\eta_2}{\pm\cos\left[\sin^{-1}\left\{\frac{2Z_{op}}{X_{op}(\eta_1/\eta_2 - \eta_2/\eta_1)}\right\}\right]\left(1 - \frac{\eta_2^2}{\eta_1^2}\right) + \left(1 + \frac{\eta_2^2}{\eta_1^2}\right)}. \tag{B.8}$$

The (+/-) modifier is necessary since the arcsine can produce an angle in one of two different quadrants.

References

[1] H.A. Macleod, *Thin-Film Optical Filters, Third Edition*, Institute of Physics Publishing, 2001.

Appendix C: Optical properties of metals

This appendix serves as an introduction to the properties of metals pertaining to their interaction with light, which plays a large role in the work outlined in Chapters 4, 5 and 6 of this thesis.

Optical properties of conductive media

In a conductive medium such as a metal, the optical properties are determined largely by free carriers, i.e., carriers that are not bound to any particular atomic site. Accordingly, the conduction term of the general wave equation is of greater interest than the polarization term, and the polarization term will be negligible in most cases. The general wave equation then reduces to:

$$\nabla^2\mathbf{E} + \frac{1}{c^2}\frac{\partial^2\mathbf{E}}{\partial t^2} = -\mu_0\frac{\partial\mathbf{J}}{\partial t}, \tag{C.1}$$

where $\mathbf{E}$ is the electric field in vector form, c is the speed of light in vacuum, μ_0 is the permeability of air and $\mathbf{J}$ is the current density. However, because of the inertia of the electrons, $\mathbf{J}$ cannot simply be replaced using the basic conductivity equation $\mathbf{J} = \sigma\mathbf{E}$. To derive a more general expression for $\mathbf{J}$, we can start by with the equation for a linear harmonic oscillator with no restoring force to describe the displacement of the electrons (the restoring force term goes to zero because the electrons are unbound):

$$m\frac{d^2\mathbf{X}}{dt^2} + m\gamma\frac{d\mathbf{X}}{dt} = -e\mathbf{E} \tag{C.2}$$

where m is the electron mass, $\mathbf{X}$ is the displacement of the electrons, γ is the damping coefficient (equal to the inverse of the relaxation time, τ), and e is the electron charge. In terms of the velocity ($V = dX/dt$):

$$m\frac{d\mathbf{V}}{dt} + m\tau^{-1}\mathbf{V} = -e\mathbf{E}, \tag{C.3}$$

and since the current density can also be expressed as $\mathbf{J} = -Ne\mathbf{V}$:

$$\frac{d\mathbf{J}}{dt} + \tau^{-1}\mathbf{J} = \frac{Ne^2}{m}\mathbf{E}. \tag{C.4}$$

For a static field (i.e.: $\omega = 0$), $d\mathbf{J}/dt$ becomes zero and we obtain the expression for static conductivity:

$$\sigma = \frac{Ne^2}{m}\tau. \tag{C.5}$$

However, if $\mathbf{E}$ is assumed to have a harmonic time dependence (i.e., $\mathbf{E} = \mathbf{E_o}e^{i\omega t}$) Equation C.4 becomes:

$$\left(i\omega + \tau^{-1}\right)\mathbf{J} = \frac{Ne^2}{m}\mathbf{E}, \tag{C.6}$$

which gives a dynamic expression for $\mathbf{J}$:

$$\mathbf{J} = \frac{\sigma}{1 + i\omega\tau}\mathbf{E} \tag{C.7}$$

Equation C.7 can be substituted into Equation C.1 to obtain:

$$\nabla^2\mathbf{E} = \frac{1}{c^2}\frac{\partial^2\mathbf{E}}{\partial t^2} + \frac{\mu_0\sigma}{1 - i\omega\tau}\frac{\partial\mathbf{J}}{\partial t}. \tag{C.8}$$

This equation will have homogeneous plane wave solutions of the form:

$$\mathbf{E} = \mathbf{E_o}e^{i(Kz - \omega t)}, \tag{C.9}$$

where the complex wavenumber K is given by:

$$K^2 = \frac{\omega^2}{c^2} + \frac{i\omega\mu_0\sigma}{1 - i\omega\tau}. \tag{C.10}$$

At very low frequencies ($\omega \to 0$), $K^2 \simeq i\omega\mu_0\sigma$, or $K = -\sqrt{i\omega\mu_0\sigma} = (1-i)\sqrt{\omega\mu_0\sigma/2}$ (since $\left(\frac{1-i}{\sqrt{2}}\right)^2 = -i$). Since the complex wavenumber is related to the complex refractive index through $K = Nk_o = N\omega/c$, the real and imaginary components of the refractive index ($N = n - i\kappa$) in the low frequency limit are given by:

$$n \simeq \kappa \simeq \sqrt{\frac{\sigma}{2\omega\varepsilon_o}}. \tag{C.11}$$

This equation indicates that n and κ will diverge in the low frequency region. In addition, it can be used to find the skin depth δ of the metal, defined as the distance a plane wave at normal incidence will travel into a metal before either its electric field amplitude or intensity (depending on the reference) decays to $1/e$ of its initial value. In terms of intensity, the absorption coefficient α can be used to derive an expression for skin depth since $\alpha = 2k_o\kappa$:

$$\delta_I = \frac{1}{\alpha} = \sqrt{\frac{1}{2\omega\mu_0\sigma}}. \tag{C.12}$$

When going to higher frequencies, the general expression for K given in Equation C.10 is more useful. Again, using the fact that $K = Nk_o = N\omega/c$, we obtain:

$$N^2 = \varepsilon_r = 1 - \frac{\omega_p^2}{\omega^2 - i\omega\tau^{-1}}, \tag{C.13}$$

where ε_r is the permittivity of the metal, $\omega_p = \sqrt{\frac{Ne^2}{m\varepsilon_o}}$ is the plasma frequency of the metal, and ε_o is the permittivity of free space. This equation is also sometimes called the Drude model. The plasma frequency is the natural oscillation frequency

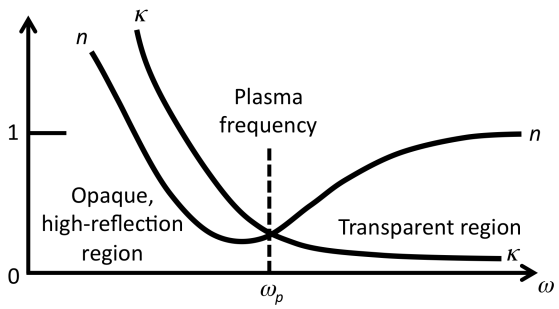

Figure C.1: Typical plot of index of refraction n and extinction coefficient κ for a metal. [3]

of the free electrons in the conductor. For example, if the electrons in a conductor were somehow arranged in to alternating planes of high and low electron density, the charge density would oscillate at the plasma frequency, which depends on the inertia and forces between the electrons [1]. Quanta of the energy associated with these oscillations are called plasmons.

Since $N = n - i\kappa$, we can use Equation C.13 to find expressions for n and κ:

$$n^2 - \kappa^2 = 1 - \frac{\omega_p^2}{\omega^2 + \tau^{-2}}, \tag{C.14}$$

$$2n\kappa = \frac{\omega_p^2}{\omega^2 + \tau^{-2}} \left(\frac{1}{\omega\tau} \right). \tag{C.15}$$

Solving these equations numerically produces plots similar to that seen in Figure C.1. For low frequencies, n and κ are close to the same value and divergent, indicating a high degree of opaqueness. At high frequencies n and κ approach limits of 1 and 0, respectively, showing that metals (like all materials) are essentially transparent for sufficiently high frequencies. The two curves cross at $\omega = \sqrt{\omega_p^2 - \tau^{-2}} \simeq \omega_p$. This model describes most metals quite well, and the approximation for the crossing frequency is usually accurate given that typically ω_p is on the order of 10^{16} rad/s while τ^{-1} is on the order of 10^{13} s^{-1}.

The lossless metal approximation

When studying the optical properties of metals, it is useful to examine the behaviour of an ideal, lossless metal, in which it is assumed that there are zero collisions of the free electrons with the atomic lattice, i.e. that the relaxation time $\tau \to \infty$. In the static case (Equation C.5), $\sigma \to \infty$, and at DC the lossless metal has infinite conductivity. Of course, at higher frequencies the inertial effects of the electrons comes into play, and Equation C.13 becomes:

$$N^2 = \varepsilon_r = 1 - \frac{\omega_p^2}{\omega^2}. \tag{C.16}$$

From this equation we can make several observations. First, for frequencies less than the plasma frequency, ε_r is negative, leading to a purely imaginary refractive index ($N = i\kappa$). Correspondingly, the wavenumber ($K = Nk_o$) is also purely imaginary, corresponding to an evanescent wave decay of the wave at the metal boundary. In this case the energy of the incident wave is completely reflected. At frequencies above the plasma frequency, ε_r is positive and less than 1, corresponding to a completely real refractive index that is also less than 1. The wave propagates without loss in the metal, although it is highly dispersive as n changes rapidly with frequency just above the plasma frequency.

For real metals, where loss associated with the collisions of electrons must be taken into account, the general Drude model is fairly accurate. Some metals will have a different plasma frequency than that predicted by this model however, due to interband resonant transmissions. This will typically cause a reduction in reflectance in blue region wavelengths, which causes some metals such as copper or gold to have their distinctive colours.

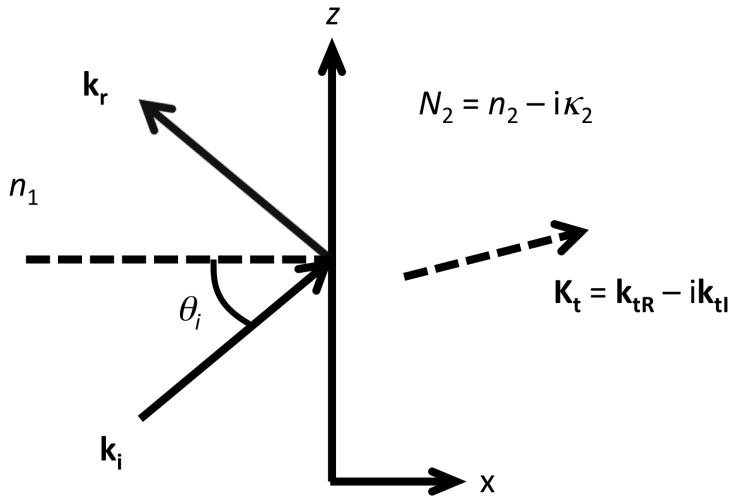

Figure C.2: Schematic showing light impinging on a dielectric/metal boundary.

Light interaction at metal boundaries

If a plane wave traveling in a lossless medium is incident on an absorbing medium (like a metal) with a complex refractive index and complex wavenumber (as shown in Figure C.2), the refracted wave inside the medium can be considered to also have a complex wave vector, i.e., $\mathbf{K_t} = \mathbf{k_{tR}} - i\mathbf{k_{tI}}$. Given this wave vector, the complex fields can be expressed as:

$$\mathbf{E_i} = \mathbf{E_{io}} e^{i(\mathbf{k_i}\cdot\mathbf{r} - \omega t)}, \tag{C.17}$$

$$\mathbf{E_r} = \mathbf{E_{ro}} e^{i(\mathbf{k_r}\cdot\mathbf{r} - \omega t)}, \tag{C.18}$$

$$\mathbf{E_t} = \mathbf{E_{to}} e^{i(\mathbf{K_t}\cdot\mathbf{r} - \omega t)} = \mathbf{E_{to}} e^{\mathbf{k_{tI}}\cdot\mathbf{r}} e^{i(\mathbf{k_{tR}}\cdot r - \omega t)}. \tag{C.19}$$

As in the case of a dielectric interface, the fields must maintain a constant ratio at the boundary plane. These boundary conditions can be expressed as:

$$\mathbf{k_i} \cdot \mathbf{r} = \mathbf{k_t} \cdot \mathbf{r}, \tag{C.20}$$

$$\mathbf{k_i} \cdot \mathbf{r} = \mathbf{K_t} \cdot \mathbf{r} = (\mathbf{k_{tR}} - i\mathbf{k_{tI}}) \cdot \mathbf{r}. \tag{C.21}$$

Equation C.20 expresses the law of reflection, while the second equation, if the real and imaginary parts are set equal to one another, produces;

$$\mathbf{k_i} \cdot \mathbf{r} = \mathbf{k_{tR}} \cdot \mathbf{r}, \tag{C.22}$$

$$0 = \mathbf{k_{tI}} \cdot \mathbf{r}. \tag{C.23}$$

These equations indicate that the real and imaginary components of the wave vector in the metal have different directions, and in this case the wave is inhomogeneous. Also, we can note that $\mathbf{k_{tR}}$ can have any direction, determined by n_1 and θ_i, and that $\mathbf{k_{tI}}$ is always perpendicular to the boundary, as illustrated in Figure C.3. Equation C.22 is analogous to Snell's law, and can be used to find the angle of refraction ϕ that separates $\mathbf{k_{tR}}$ and $\mathbf{k_{tI}}$:

$$k_i \sin\theta_i = k_{tR} \sin\phi, \tag{C.24}$$

where k_i and k_{tR} are the magnitudes of $\mathbf{k_i}$ and $\mathbf{k_{tR}}$, respectively. However, it is important to note that k_{tR} is not constant but actually a function of ϕ. As shown in Figure C.3, the planes of constant phase are perpendicular to $\mathbf{k_{tR}}$, while the planes of constant amplitude are perpendicular to $\mathbf{k_{tI}}$. This property means that the photon flux decays with distance away from the boundary inside the medium, and that power flows along the direction of $\mathbf{k_{tI}}$, not in line with $\mathbf{k_{tR}}$, making the wave in the metal non-homogeneous. Only in the normal-incidence case ($\theta_i = 0$) do $\mathbf{k_{tR}}$ and $\mathbf{k_{tI}}$

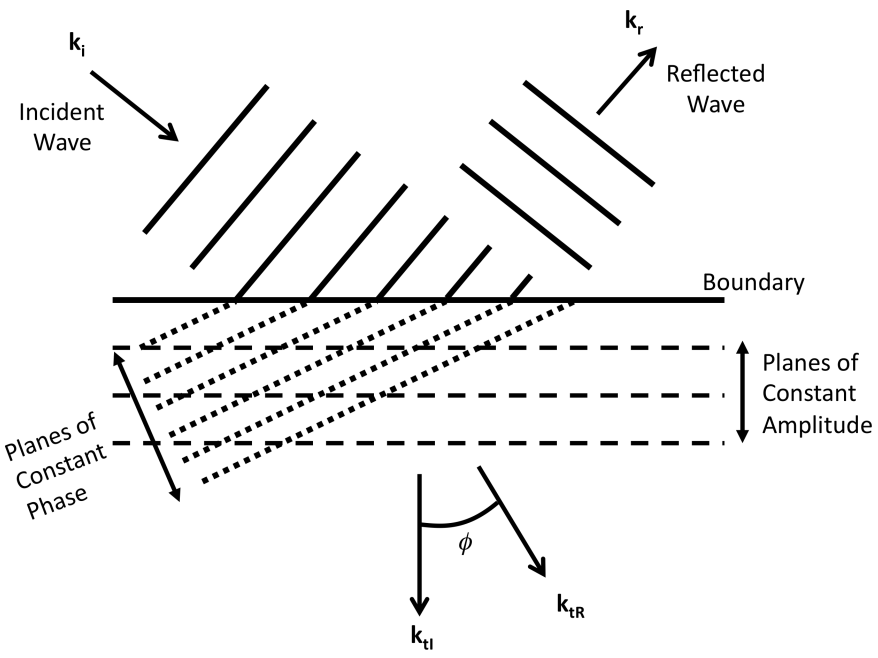

Figure C.3: Schematic showing real and imaginary components of the wave vector in an absorbing medium, with oblique incidence light.

align along the same direction, in which case the wave is considered to be a lossy, homogeneous wave.

There is also a relationship between $\mathbf{k_{tR}}$ and $\mathbf{k_{tI}}$ that can be derived using Maxwell's equations [3]:

$$k_{tr}\cos\phi + ik_{ti} = k_o\sqrt{N^2 - \sin^2\theta_i}. \tag{C.25}$$

This equation assumes the light is incident from air. In addition, it can be shown that the Fresnel formulae and related transfer matrix techniques still apply to absorbing layers [3]. The only real difference is that the complex refractive indices and complex propagation angles (calculated using Snell's law) are used in the appropriate places when metal layers are involved. It is also important to note that the complex angle of propagation in the metal is not equal to the angle between $\mathbf{k_{tR}}$ and $\mathbf{k_{tI}}$, which has a real value.

References

[1] S. Ramo, J.R. Whinnery, T. Van Duzer, *Fields and Waves in Communication Electronics, Third Edition*, John Wiley & Sons, Inc., 1994.

[2] B.E.A. Saleh, M.C. Teich, *Fundamentals of Photonics*, John Wiley & Sons, Inc., 1991.

[3] G.R. Fowles, *Introduction to Modern Optics, Second Edition*, Dover Publications, Inc., 1975.